PULSED LASER DEPOSITION: ENERGETIC GROWTH EFFECTS IN GROUP IV SEMICONDUCTOR MATERIALS

Thesis by

Maggie E. Taylor

In Partial Fulfillment of the Requirements

for the Degree of

Doctor of Philosophy

California Institute of Technology

Pasadena, California

1998

(Submitted April 24, 1998)

Dedication

This thesis is dedicated to Kyu Min, who likes me when I drink too much and who looks like Jackie Chan when he drinks too much. Minnow and I have been friends in the lab and out of the lab, in snow and in rain and in sunshine, on planes and on trains and on boats, and on at least two continents.

Acknowledgements

I want to thank Ann Taylor and Dr. Bernard Taylor for providing me with the ambition and the resources to survive graduate school.

I want to thank Dr. Harry Atwater for his encouragement, for all of the proposals that he put together to support my research, and for putting up with my temper.

I want to thank Dr. Harry Atwater, Dr. Eric Chason, Dr. David Goodwin, Dr. Hyun Joo, Dr. James McCamy, and Dr. Albert Polman for their guidance.

I want to thank Carol Garland for assisting me with transmission electron microscopy. Without her assistance very few of my samples would have survived long enough to reach the scope. I am trying to learn to be as patient as Carol, both with people and with samples.

I want to thank Dr. Gang He for assisting me with molecular beam deposition. Gang provided me with the molecular beam deposition samples used in my alloy work. The time that he and I spent together at the FOM Institute for Atomic and Molecular Physics means a great deal to me.

I want to thank Kyu Min for assisting me with transmission electron microscopy and molecular beam deposition. Minnow provided me with the molecular beam deposition samples used in my simulation work. It will be difficult for me to adjust to not having him within earshot.

I want to thank Michael Easterbrook for assisting me with Rutherford backscattering spectrometry.

I want to thank Claudine Chen and Dr. Chih Yang for assisting me with our computer systems.

I want to thank Robert Beach, Brendan Crill, Stephen Glade, and Matthew Ragan for assisting me to run my simulation code. I want to thank Dr. William Goddard, Dr. David Goodwin, Dr. Thomas Tombrello, and the Engineering Computing Facility for providing me with computer systems to run my simulation code.

I want to thank Elizabeth Boer, Dr. David Boyd, Mark Brongersma, Dr. Renato Camata, Joseph Christopherson, Dr. Erik Daniel, Dr. Jennifer Dooley, Dr. John Hartman, Dr. Gerlas van den Hoven, Ushma Kriplani, Dr. Torrey Lyons, Dr. Ramana Murty, Dr. Laura Nagel, Dr. Kirill Shcheglov, Maribeth Swiatek, Regina Ragan, and Rosalie Rowe for assisting me on countless occasions in the lab and out of the lab.

I want to thank Dr. Harry Atwater, Dr. Brent Fultz, Dr. David Goodwin, Dr. William Johnson, and Dr. Thomas McGill for conducting my candidacy exam. I want to thank Dr. Harry Atwater, Dr. Brent Fultz, Dr. David Goodwin, Dr. Sossina Haile, and Dr. William Johnson for conducting my thesis exam.

Lastly, I want to thank Robert Beach for his support. For the last few months, Bobby has washed my clothes, put gasoline in my car, fed my turtles, and done everything possible to assure that I would complete my thesis on time. I promise to return the favor.

Support

The research that comprises this thesis was supported by the National Science Foundation, by the North Atlantic Treaty Organization, by a Clare Boothe Luce Graduate Fellowship, and by an Intel Foundation Graduate Fellowship. It was performed at the California Institute of Technology and at the FOM Institute for Atomic and Molecular Physics.

Primary Author Publications

"Monte Carlo Simulations of Epitaxial Growth: Comparison of Pulsed Laser Deposition and Molecular Beam Epitaxy," M. E. Taylor and H. A. Atwater, Applied Surface Science, (1998).

"Role of Energetic Flux in Low Temperature Si Epitaxy on Dihydride-Terminated Si (001)," M. E. Taylor, H. A. Atwater, and M. V. R. Murty, Thin Solid Films, (1998).

"Low Temperature Epitaxy of Si on Dihydride-Terminated Si (001): Energetic Versus Thermal Growth," M. E. Taylor, H. A. Atwater, and M. V. R. Murty, Materials Research Society Symposia Proceedings 441, 579 (1997).

"Solid Phase Epitaxy of Diamond Cubic Sn_xGe_{1-x} Alloys," M. E. Taylor, G. He, and H. A. Atwater, Journal of Applied Physics 80, 4384 (1996).

"Inhibited Sn Surface Segregation in Epitaxial Sn_xGe_{1-x} Alloy Films Grown by Pulsed Laser Deposition," M. E. Taylor, G. He, C. Saipetch, and H. A. Atwater, Materials Research Society Symposia Proceedings 388, 97 (1995).

Abstract

Pulsed laser deposition is characterized by a broad deposition energy distribution with a mean energy of a few eV or a few tens of eV. The research that comprises this thesis was motivated by a desire to characterize energetic growth effects in pulsed laser deposition of Group IV semiconductor materials in order to understand and manipulate fundamental growth kinetics. This research specifically focuses on energetic effects in growth morphology, in growth on hydrogen-terminated surfaces, and in alloy growth.

In Chapter 1, pulsed laser deposition is introduced. In Chapter 2, simulated growth morphologies for Si growth by molecular beam deposition, sputter deposition, and pulsed laser deposition are compared. Feature atom displacement, an energetic effect, was found to significantly decrease roughness at low substrate temperatures. Pulsed roughening, a temporal effect, was found to slightly increase roughness at high substrate temperatures. In Chapter 3, crystalline Si grown by pulsed laser deposition on dihydride-terminated Si (001) surfaces and by molecular beam deposition and sputter deposition on clean Si (001) surfaces are compared. H transfer and Si subplantation, two energetic effects, were found to enable crystalline growth on dihydride-terminated Si (001) surfaces. In Chapter 4, crystalline Sn_xGe_{1-x} grown by solid phase epitaxy and pulsed laser deposition are compared. Solid phase epitaxy was found to produce alloys with compositions no larger than approximately 0.05. Pulsed laser deposition was found to produce alloys with compositions as large as approximately 0.38. Composition was found to increase with ablation energy density. In Appendix A, actual and simulated growth morphologies for Si growth by

molecular beam deposition and pulsed laser deposition are compared. In Appendix B, the simulation code is listed.

Abbreviations

A number of conventional and unconventional unit abbreviations are used in this thesis. The unconventional unit abbreviations are described below.

Unit	Abbreviation
atom	atm
jump	jmp
monolayer	mL
pulse	pls

Contents

Figures

Chapter 1

Pulsed Laser Deposition

1.1 Background

In pulsed laser ablation, a laser beam is focused on a target. The photons interact with the material through ablation processes and ablated material is carried away from the target in a plume. In pulsed laser deposition, ablated material is deposited on a substrate.

Pulsed laser ablation has been the focus of extensive research [1]. Primary ablation processes include electronic sputtering, exfoliational sputtering, and hydrodynamic sputtering. Electronic sputtering arises when material absorbs laser radiation at levels sufficient to trigger dielectric breakdown and plasma formation. Exfoliational sputtering occurs when repeated thermal shocks result in expulsion of particles of material. Hydrodynamic sputtering occurs when transient melting processes result in expulsion of particles of material.

Pulsed laser deposition has been the focus of extensive research [2]. Pulsed laser deposition was first developed in the 1960s. Advances in laser technology in the 1970s made pulsed laser deposition more feasible. Growth of high-temperature superconductors in the 1980s brought pulsed laser deposition into the foreground. Materials systems that have been explored using pulsed laser deposition include metals, superconductors, semiconductors, oxides on semiconductors, ferroelectrics, ferrites, polymers, tribological materials, and biocompatible materials.

Pulsed laser deposition has several advantages in comparison to more conventional deposition processes [2]. Pulsed laser deposition systems are simple, durable, and versatile. Necessary *in situ* components are limited to a target system and a substrate system. The typically least reliable component, the laser, is an *ex situ* component. The deposited material can be varied rapidly by *in situ* or *ex situ* replacement of the target. Pulsed laser deposition has characteristics that can be utilized to grow materials with new and improved properties. Plumes are typically characterized by a high ionization fraction, an energy distribution that peaks at a few eV or a few tens of eV and can extend to hundreds of eV, and a composition that reflects the target composition.

Pulsed laser deposition has several disadvantages in comparison to more conventional deposition processes [2]. Exfoliational sputtering, hydrodynamic sputtering, and condensation of atoms in the plume lead to deposition of particles, referred to as macroparticles, that can be as large or larger than a few microns. Plumes are typically characterized by a narrow forward angular distribution that impedes uniform deposition over large areas. These disadvantages are inconvenient but not insurmountable. Macroparticle deposition can be decreased using molten targets, mechanical velocity selectors, biased substrates, and innovative ablation and deposition geometries. Deposition uniformity can be increased using substrate rotation, substrate translation, and laser beam translation.

Pulsed laser deposition of Group IV semiconductor materials is largely uncharacterized. Si and Ge films grown in the 1980s by pulsed laser deposition exhibited good crystallinity [3,4]. This research was unfortunately not pursued, largely because of competition from more conventional deposition processes.

The research that comprises this thesis was motivated by a desire to characterize energetic growth effects in pulsed laser deposition of Group IV semiconductor materials in order to understand and manipulate fundamental growth kinetics. This research specifically focuses on energetic effects in growth morphology, in growth on hydrogen-terminated surfaces, and in alloy growth. In the remainder of Chapter 1, the pulsed laser deposition system is described. In Chapter 2, simulated growth morphologies for Si growth by molecular beam deposition, sputter deposition, and pulsed laser deposition are compared. In Chapter 3, crystalline Si grown by pulsed laser deposition on dihydride-terminated Si (001) surfaces and by molecular beam deposition and sputter deposition on clean Si (001) surfaces are compared. In Chapter 4, crystalline Sn_xGe_{1-x} grown by solid phase epitaxy and pulsed laser deposition are compared. In Appendix A, actual and simulated growth morphologies for Si growth by molecular beam deposition and pulsed laser deposition are compared. In Appendix B, the simulation code is listed.

1.2 Deposition System

The pulsed laser deposition system constructed for use in this research is sketched in Figure 1.1. It is comprised of an excimer laser system, a vacuum system, a deposition system, and a reflection high-energy electron diffraction system.

The excimer laser system uses a lasing gas consisting of 0.24% F, 6% Kr, and a Ne balance. It operates at a wavelength of 248 nm, a maximum power of 0.25 J pls^{-1}, and a maximum repetition rate of 200 pls sec^{-1}.

The vacuum system is comprised of a growth chamber, a loadlock chamber, two mechanical pumps, two turbomolecular pumps, a sublimation pump, two gate valves, an ion gauge, and a quadrupole gas analyzer. The growth chamber is pumped by a mechanical pump, a turbomolecular pump, and a sublimation pump, and has a base pressure of 5x10^{-10} torr. The loadlock chamber is pumped by a mechanical pump and a turbomolecular pump, and has a base pressure of 5x10^{-9} torr. The gate valves are located between the growth chamber and the growth chamber turbomolecular pump and between the growth chamber and the loadlock chamber. The ion gauge and the quadrupole gas analyzer are located in the growth chamber. The vacuum system is vented through the loadlock chamber turbomolecular pump and is vented with N_2.

The deposition system is comprised of a lens, a window, a substrate system, and a target system. The lens focuses the excimer beam at the target and is made of fused silica. The window allows the excimer beam to enter the growth chamber and is made of MgF.

The substrate system is comprised of a baseplate and two manipulators. The first manipulator is located in the growth chamber and is comprised of a holder, a heater, a rotary feedthrough, a linear feedthrough, and an alignment gimbal. The second manipulator is located in the loadlock chamber and is comprised of a holder, a magnetically coupled transporter, and an alignment gimbal. The substrate is attached to the baseplate by restraining screws. Rods on the exterior of the baseplate fit into grooves in the exteriors of the holders. The baseplate is passed between the holders by means of the magnetically coupled transporter. The heater is a resistive heater and has a maximum temperature of approximately 750 °C, which translates into a maximum substrate temperature of approximately 420 °C. The rotary feedthrough, linear feedthrough, and alignment gimbals provide positioning flexibility.

The target system is located in the growth chamber and is comprised of a holder, a rotary feedthrough, a linear feedthrough, and an alignment gimbal. The holder can hold a circular target with a diameter of 1 in, a circular target with a diameter of 3 in, or a circular target with a diameter of 1 in and a toroidal target with an inside diameter of 1 in and an outside diameter of 3 in. The targets are attached to the holder by restraining rings. The rotary feedthrough rotates the target at 10 rpm to avoid severe target erosion. The linear feedthrough and alignment gimbal provide positioning flexibility.

The reflection high-energy electron diffraction system is located in the growth chamber and is comprised of a 20 keV electron gun and a phosphor screen.

After each exposure of the growth chamber to air, a series of routines were performed to prepare for growth experiments. Heating tapes were used to bake the growth chamber at 200 °C to desorb adsorbed H_2O. Components not accessible with heating tapes were baked using a heat gun. After the growth chamber cooled to room temperature, the target was ablated to remove adsorbed hydrocarbons and H_2O. The substrate baseplate was inserted prior to ablation to protect the substrate heater.

Excimer power was measured prior to each growth experiment using a thermopile meter. Power was found to remain relatively constant for three to four days after replacement of the lasing gas and to decrease rapidly thereafter. The lasing gas was replaced every three days when the pulsed laser deposition system was in use.

Excimer energy density at the target was periodically calibrated. To obtain an estimate of the irradiated area, thermal burn paper was placed in the target holder. To obtain an estimate of the energy, the thermopile meter was inserted into the growth chamber.

Substrate temperature was periodically calibrated using a Si substrate with embedded thermocouples. In each measurement, the heater power was incremented and the heater temperature and substrate temperature were recorded. Substrate temperature did not vary with thermocouple position, indicating a constant temperature profile across the substrate. The calibration curves did not change significantly between calibration experiments.

The MgF window was periodically removed and cleaned. Deposited material was dissolved in CH_3OH.

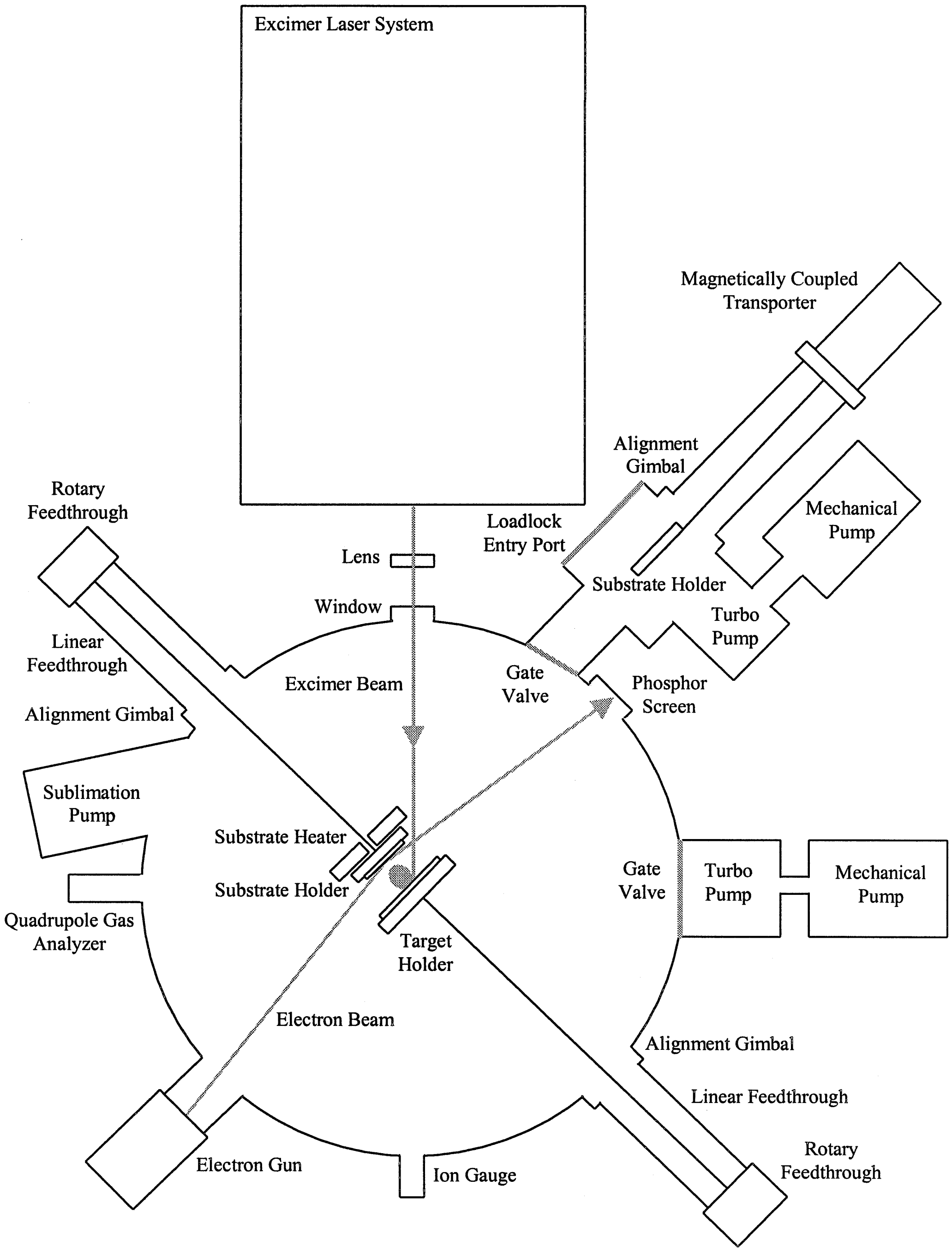

Figure 1.1: The pulsed laser deposition system.

1.3 Substrate Preparation

The Si (001) surface has several H termination states [5]. The dihydride-terminated (1x1) Si (001) surface is stable at temperatures below approximately 370 °C. The monohydride-terminated (2x1) Si (001) surface is stable at temperatures between 370 °C and 450 °C. The clean (2x1) Si (001) surface is stable at temperatures above approximately 450 °C.

Each Si (001) substrate was immersed in a solution of H_2O, H_2O_2, and NH_4OH to oxidize the contaminated surface layer and in a solution of H_2O and HF to remove the oxidized surface layer and to produce a dihydride-terminated (1x1) Si (001) surface. The dihydride-terminated (1x1) Si (001) surface is resistant to contamination and can be stored in ultra-high vacuum for several hours.

1.4 Energy Distribution

The energy distribution of the plume varies with the target material and the target energy density. To estimate the energy distributions that characterize pulsed laser deposition of Group IV semiconductor materials, the energy distribution of Si ablated at an energy density of approximately 3 J cm^{-2} was determined.

The substrate manipulator located in the growth chamber was removed and replaced with an ion probe constructed from Cu wire. A polycrystalline Si substrate was used as a target. Time-of-flight spectra were collected and analyzed using a digital oscilloscope.

The plume was assumed to expand perpendicular to the target, to expand collisionlessly, and to consist of monomeric Si. Origin was used to estimate a Si^+ ion energy distribution from the time-of-flight spectra using the transformation

$$E = mx^2/2t^2$$

where E is energy, m is the mass of a Si atom, x is the distance between the target and the ion probe, and t is the time-of-flight [6]. This energy distribution is shown in Figure 1.2. It ranges from 10 eV to 135 eV and peaks at approximately 20 eV.

Si neutral energy distributions, studied by planar laser induced fluorescence, are reported to be very similar to Si^+ ion energy distributions [7]. The Si neutral energy distribution was assumed to be equal to the Si^+ ion energy distribution.

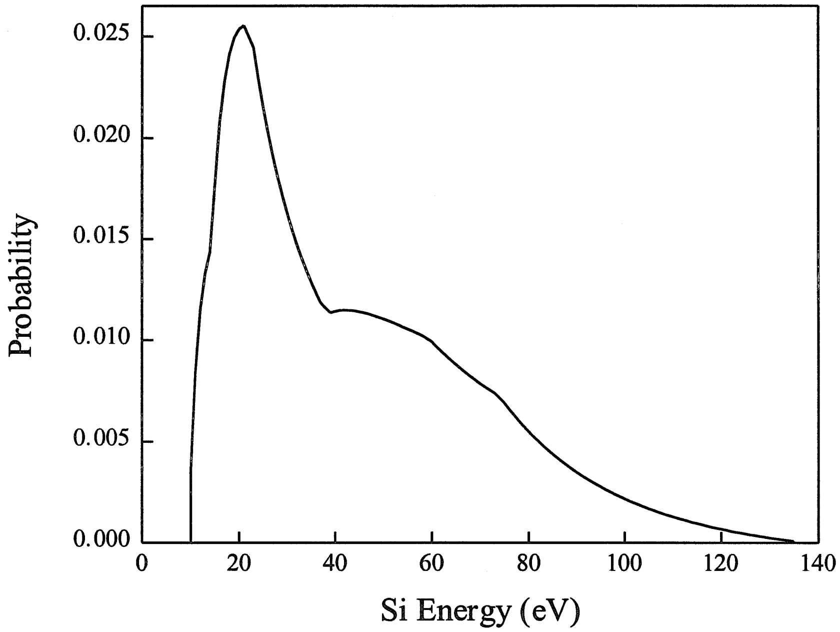

Figure 1.2: Estimated energy distribution for Si ablated at an energy density of approximately 3 J cm^{-2}.

References

[1] Laser Ablation and Desorption, Ed. J. C. Miller and R. F. Haglund, Jr., Academic Press, San Diego, 1998.

[2] Pulsed Laser Deposition of Thin Films, Ed. D. B. Chrisey and G. K. Hubler, John Wiley and Sons, Inc., New York, 1994.

[3] D. Lubben, S. A. Barnett, K. Suzuki, S. Gorbatkin, and J. E. Greene, J. Vac. Sci. Technol. B 3, 968 (1985).

[4] H. Sankur, W. J. Gunning, J. DeNatale, and J. F. Flintoff, J. Appl. Phys. 65, 2475 (1989).

[5] G. Schulze and M. Henzler, Surf. Sci. 124, 336 (1983).

[6] Origin, Microcal Origin.

[7] D. L. Capewell, Doctoral Thesis, Adv. D. G. Goodwin, California Institute of Technology, 1996.

Chapter 2

Simulation of Energetic Effects in Silicon Growth Morphology

2.1 Background

Figures 2.1 and 2.2 show scanning electron micrographs of Ge grown on Si (001) surfaces at a deposition rate of 0.5 nm sec^{-1} and a substrate temperature of 300 ^{o}C by molecular beam deposition and pulsed laser deposition, respectively [1]. The Ge grown by molecular beam deposition is polycrystalline. The Ge grown by pulsed laser deposition is crystalline. The surface of the former is significantly rougher than the surface of the latter. These results suggest that growth morphology is affected by the deposition process.

Molecular beam deposition, sputter deposition, and pulsed laser deposition exhibit different growth kinetics. Molecular beam deposition is characterized by a continuous temporal distribution and a narrow energy distribution with a mean energy of a few tenths of an eV. Sputter deposition is characterized by a continuous temporal distribution and a broad energy distribution with a mean energy of a few eV or a few tens of eV. Pulsed laser deposition is characterized by a pulsed temporal distribution and a broad energy distribution with a mean energy of a few eV or a few tens of eV.

Growth morphology is primarily determined by interplay between stochastic roughening, nonstochastic roughening, and surface diffusion smoothening. In the low temperature limit, growth morphology is determined by stochastic roughening. In the high temperature limit, growth morphology is determined by surface diffusion smoothening. As the temporal distribution is shifted to higher pulsing degrees, stochastic roughening arising from a high instantaneous deposition rate, referred to as pulsed roughening, is expected to come increasingly into play. As the energy distribution is shifted to higher energies, smoothening arising from feature atom displacement, referred to as energetic smoothening, is expected to come increasingly into play.

To evaluate the effects of temporal distribution and energy distribution on growth morphology, an atomistic simulation was developed [2].

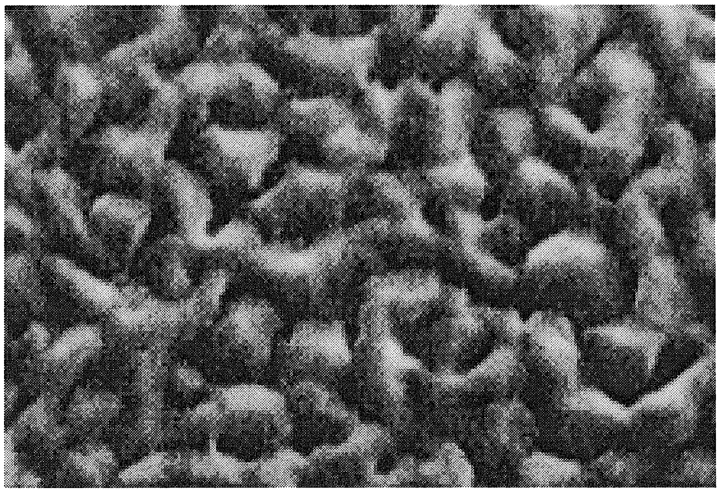

Figure 2.1: Scanning electron micrograph of Ge grown on a Si (001) surface by molecular beam deposition at a deposition rate of 0.5 nm sec^{-1} and a substrate temperature of 300 °C [1]. The image area is approximately 7 μm by 5 μm.

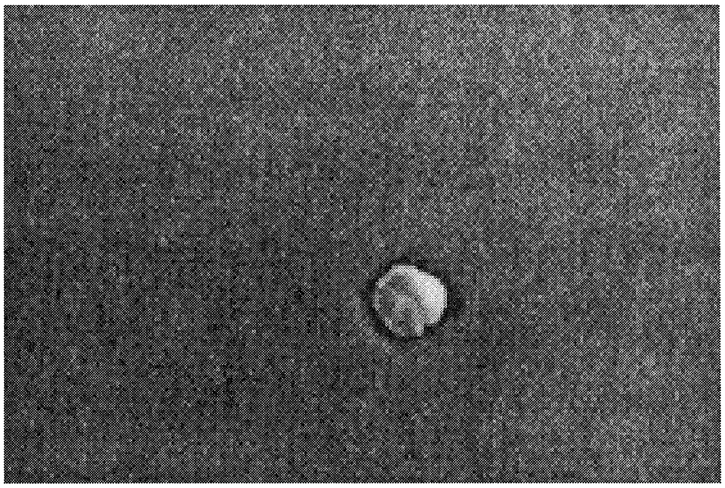

Figure 2.2: Scanning electron micrograph of Ge grown on a Si (001) surface by pulsed laser deposition at a deposition rate of 0.5 nm sec^{-1} and a substrate temperature of 300 °C [1]. The image area is approximately 7 μm by 5 μm.

Reprinted with permission from "High Quality Optical and Epitaxial Ge Films Formed by Laser Evaporation," H. Sankur, W. J. Gunning, J. DeNatale, and J. F. Flintoff, J. Appl. Phys. 65. Copyright 1989 American Institute of Physics.

2.2 Simulation Theory

Although the objective was to obtain qualitative results descriptive of Group IV semiconductor growth, it was necessary to select a specific Group IV semiconductor surface to simulate. The Si (001) surface was selected because it has been the focus of extensive research.

Two temporal distributions are simulated. The continuous distribution is characterized by a mean time between deposition events. The pulsed distribution is characterized by a mean time between deposition events in a deposition pulse and a time between deposition pulses.

Two energy distributions are simulated. In the thermal distribution, deposition events are characterized by an energy of 0.3 eV, an energy selected to reflect Si molecular beam deposition. In the energetic distribution, deposition events are characterized by an energy distribution that ranges from 10 eV to 135 eV and peaks at approximately 20 eV, an energy distribution selected to reflect Si pulsed laser deposition as described in Chapter 1. This energy distribution is shown in Figure 1.2.

Four deposition process types are simulated. The first type uses the continuous temporal distribution and the thermal energy distribution and is intended to simulate molecular beam deposition. The second type uses the continuous temporal distribution and the energetic energy distribution and is intended to simulate sputter deposition. The third type uses the pulsed temporal distribution and the energetic energy distribution and is intended to simulate pulsed laser deposition. The fourth type uses the pulsed temporal distribution and the thermal energy distribution and is intended to be complementary to the first three types.

If an atom is incident on an atom that forms the perimeter of a feature, the collision may result in displacement of the feature atom and replacement of the feature atom by the incident atom. This effect, referred to as feature atom displacement, is simulated. An energy distribution for this effect was extrapolated from molecular dynamics simulation results for Si atom displacement yield from Si (001) surfaces irradiated by Ar^+ ions [3]. This energy distribution is shown in Figure 2.3.

It should be noted that a number of potentially important effects are not simulated. These effects include bulk displacement, radiation damage, hydrogen termination, surface reconstruction, anisotropic surface diffusion, anisotropic bonding, and surface diffusion involving step edge heights greater than two monolayers.

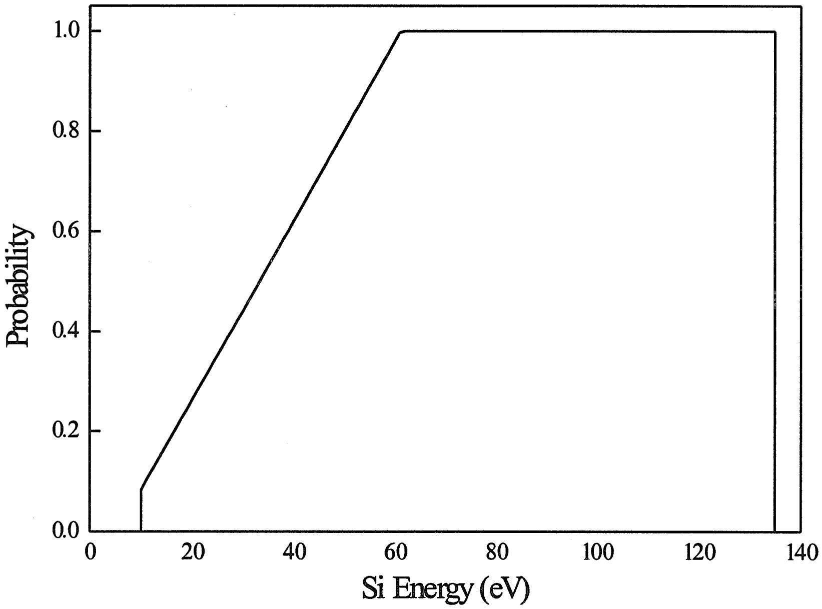

Figure 2.3: Estimated energy distribution for Si feature atom displacement [3].

2.2.1 Architecture

The simulation is similar in structure to simulations previously developed to study molecular beam deposition [4-6]. The growth volume is a simple cubic lattice with unity lattice parameter. The substrate extends in the x and y directions. Growth occurs in the z direction. The boundary conditions are periodic in the x and y directions.

An occupied site is a lattice site that contains an atom. A surface site is an occupied site whose z coordinate is greater than the z coordinates of all other occupied sites located at the same position in the x-y plane. Associated with each surface site are four neighbor sites located one lattice site from the surface site in the same x-y plane as the surface site, and a maximum of four destination sites located one lattice site from the surface site in the x-y plane, located less than three lattice sites from the surface site in the z direction, and located immediately above surface sites.

A solid atom is an atom in the growth volume. A vapor atom is an atom slated for deposition into the growth volume. A solid atom is an active atom if it is in a surface site and if fewer than four of the neighbor sites associated with the surface site are occupied sites.

Figure 2.4 shows an example growth volume. The substrate plane is not shown. Squares and dots represent lattice sites and solid atoms, respectively. Lattice sites (0,0,1), (1,0,1), (2,0,1), (0,1,1), (1,1,1), (0,2,1), (1,2,1), (2,2,1), (1,0,2), (0,1,2), and (1,1,2) are occupied sites. Occupied sites (0,0,1), (2,0,1), (0,2,1), (1,2,1), (2,2,1), (1,0,2), (0,1,2), and (1,1,2) are surface sites. Lattice sites (1,0,2), (0,1,2), (2,1,2), and (1,2,2) are neighbor sites of surface site (1,1,2). Lattice sites (2,1,1), (1,2,2), (1,0,3), and (0,1,3) are destination sites of surface site (1,1,2). The atoms in lattice sites (2,0,1), (2,2,1), (1,0,2), (0,1,2), and (1,1,2) are active atoms.

(0,0,1) ●	(1,0,1) ●	(2,0,1) ●
(0,1,1) ●	(1,1,1) ●	(2,1,1)
(0,2,1) ●	(1,2,1) ●	(2,2,1) ●

(0,0,2)	(1,0,2) ●	(2,0,2)
(0,1,2) ●	(1,1,2) ●	(2,1,2)
(0,2,2)	(1,2,2)	(2,2,2)

Figure 2.4: Example growth volume.

2.2.2 Initialization

The substrate is comprised of atoms in the set of lattice sites with zero z coordinates. This set of lattice sites forms the initial sets of occupied sites and surface sites. These atoms form the initial set of solid atoms. Each of these atoms is assigned an energy E_S equal to

$$E_S = kT$$

where k is the Boltzmann constant and T is the substrate temperature.

If the thermal energy distribution is selected, each vapor atom is assigned an energy E_V of 0.3 eV. If the energetic energy distribution is selected, each vapor atom is assigned an energy E_V according to the energy distribution shown in Figure 1.2. If the energetic energy distribution and the continuous temporal distribution are both selected, vapor atoms are assigned energies randomly with respect to deposition order. If the energetic energy distribution and the pulsed temporal distribution are both selected, each pulse contains an identical set of vapor atoms assigned decreasing energies with respect to deposition order to reflect the temporal separation of vapor atoms by energy that occurs in the interim between ablation and deposition.

Each vapor atom is assigned a feature atom displacement probability P_F according to the energy distribution shown in Figure 2.3.

2.2.3 Surface Diffusion

For each active atom and for each destination site associated with the current site of the active atom, there is a potential diffusion event corresponding to diffusion from the current site to the destination site.

Associated with each potential diffusion event is a diffusion rate D equal to

$$D = D_o e^{-Q/E}$$

where D_o is a rate, E is the energy of the active atom, and Q is an activation energy equal to

$$Q = Q_0 + A_1 Q_1 + A_2 Q_2 + A_3 Q_3$$

where Q_0, Q_1, Q_2, and Q_3 are activation parameters, A_1 is the number of occupied neighbor sites associated with the current site, A_2 is unity if the current site is one lattice site from the destination site in the z direction and zero otherwise, and A_3 is unity if the current site is two lattice sites from the destination site in the z direction and zero otherwise.

Values for D_o and Q_0 of 150 jmp μs^{-1} and 0.55 eV, respectively, were selected to reflect scanning tunneling microscopy results for Si growth on Si (001) surfaces [7]. Values for Q_1 and Q_2 of 0.30 eV and 0.15 eV, respectively, were selected to reflect molecular dynamics simulation results for Si growth on Si (001) surfaces [8]. Since diffusion on the Si (001) surface across a distance of two lattice sites in the z direction microscopically resembles diffusion on the Si (111) surface, a value for Q_3 of 0.40 eV was selected to reflect molecular dynamics simulation results for Si growth on Si (111) surfaces [9]. These values are listed in Figure 2.5.

There are twelve diffusion event types, one for each permutation of A_1, A_2, and A_3. The activation energies Q corresponding to these diffusion event types are listed in Figure 2.6.

Diffusion is monitored and controlled using a matrix in which each row represents an active atom and each column represents a diffusion event type. Each entry is a diffusion rate $D_{A,T}$ equal to

$$D_{A,T} = N_{A,T}D$$

where $N_{A,T}$ is the number of potential diffusion events of type T for which active atom A is eligible. The diffusion rate D_S for the set of active atoms, the diffusion rate D_A for an active atom, and the diffusion rate D_T for a diffusion event type are equal to

$$D_S = \Sigma_A \Sigma_T D_{A,T}$$

$$D_A = \Sigma_T D_{A,T}$$

$$D_T = \Sigma_A D_{A,T}$$

where Σ_A and Σ_T represent sums of the entries in a column and a row, respectively.

When a deposition event or a diffusion event occurs, the atoms involved in the event are reclassified as active or inactive. If an active atom becomes inactive, the corresponding row in the diffusion matrix is deleted. If an inactive atom becomes active, the diffusion rates associated with the atom are determined and a row is added to the diffusion matrix. If an active atom remains active, the diffusion rates associated with the atom are determined and the corresponding row in the diffusion matrix is modified.

When a diffusion event occurs, the diffusing atom is removed from its original site and placed in a destination site. The destination site replaces the original site in the sets of occupied sites and surface sites. The occupied site immediately beneath the original site replaces the occupied site immediately beneath the destination site in the set of surface sites. The diffused atom, the atoms in the occupied sites immediately beneath the original site and the destination site, and the atoms in the surface sites located one lattice site in the x-y plane from the original site or from the destination site are reclassified as active or inactive and the diffusion matrix is modified accordingly.

A generic diffusion event is a diffusion event selected from the set of potential diffusion events for which the set of active atoms is eligible. A diffusion event type is randomly selected from the set of diffusion event types with a selection probability P_T equal to

$$P_T = D_T/D_S.$$

An active atom is randomly selected from the set of active atoms eligible for potential diffusion events of the selected type with a selection probability $P_{T,A}$ equal to

$$P_{T,A} = D_{A,T}/D_T.$$

If among the potential diffusion events for which the selected active atom is eligible there is a single potential diffusion event of the selected type, that potential diffusion event is selected and performed. If among the potential diffusion events for which the selected active atom is eligible there are multiple potential diffusion events of the selected type, a potential diffusion event of the selected type is randomly selected and performed.

A specific diffusion event is a diffusion event selected from the set of potential diffusion events for which a specific active atom is eligible. A diffusion event type is randomly selected with a selection probability $P_{A,T}$ equal to

$$P_{A,T} = D_{A,T}/D_A.$$

If among the potential diffusion events for which the active atom is eligible there is a single potential diffusion event of the selected type, that potential diffusion event is selected and performed. If among the potential diffusion events for which the active atom is eligible there are multiple potential diffusion events of the selected type, a potential diffusion event of the selected type is randomly selected and performed.

Diffusion is characterized by two diffusion times. The time τ_S necessary for a generic diffusion event to occur is equal to

$$\tau_S = 1/D_S.$$

The time τ_A necessary for a specific diffusion event to occur is equal to

$$\tau_A = 1/D_A.$$

In a generic diffusion event cycle, a timer value is incremented by the time τ_S. If the timer value is equal to or smaller than a preset value, a generic diffusion event is selected and performed. In a specific diffusion event cycle, a timer value is incremented by the time τ_A. If the timer value is equal to or smaller than a preset value, a specific diffusion event is selected and performed.

Parameter	Value	Reference	Method
D_o	150 jmp μs^{-1}	[7]	Si (001) Scanning Tunneling Microscopy
Q_0	0.55 eV	[7]	Si (001) Scanning Tunneling Microscopy
Q_1	0.30 eV	[8]	Si (001) Molecular Dynamics Simulations
Q_2	0.15 eV	[8]	Si (001) Molecular Dynamics Simulations
Q_3	0.40 eV	[9]	Si (111) Molecular Dynamics Simulations

Figure 2.5: Surface diffusion parameters.

Neighbors	Vertical Separation (mL)	Activation Energy (eV)
0	0	0.55
0	1	0.70
0	2	0.95
1	0	0.85
1	1	1.00
1	2	1.25
2	0	1.15
2	1	1.30
2	2	1.55
3	0	1.45
3	1	1.60
3	2	1.85

Figure 2.6: Surface diffusion activation energies.

2.2.4 Deposition

When a deposition event occurs, a surface site is randomly selected. If the atom in the surface site is inactive, the vapor atom is placed in the lattice site immediately above the surface site. If the atom in the surface site is active, a value between zero and unity is randomly selected. If the randomly selected value is greater than the feature atom displacement probability P_F associated with the vapor atom, the vapor atom is placed in the lattice site immediately above the surface site. If the randomly selected value is equal to or less than the feature atom displacement probability P_F associated with the vapor atom, a specific diffusion event cycle featuring the atom in the surface site is performed and the vapor atom is placed in the surface site. The deposited atom is removed from the set of vapor atoms and added to the set of solid atoms. The energy of the deposited atom is changed from energy E_V to energy E_S. If the deposition site is the lattice site immediately above the surface site, the deposition site is added to the sets of occupied sites and surface sites and the surface site is removed from the set of surface sites. The deposited atom is reclassified as active or inactive. If the deposition site is the lattice site immediately above the surface site, the atom in the surface site and the atoms in surface sites located one lattice site in the x-y plane from the deposition site are also reclassified as active or inactive. The diffusion matrix is modified accordingly.

If the continuous temporal distribution is selected, deposition is characterized by a rate R_C and a time τ_C equal to

$$\tau_C = 1/R_C.$$

If the pulsed temporal distribution is selected, deposition is characterized by rates R_P and R_R and times τ_P and τ_R equal to

$$\tau_P = \tau_D/R_P$$

$$\tau_R = (1/R_R)-\tau_D$$

where R_P is the deposition rate within a pulse, R_R is the pulse repetition rate, and τ_D is the pulse duration. A value for τ_D of 5 μs pls^{-1} was selected to reflect Si pulsed laser deposition as described in Chapter 1.

2.2.5 Sequence

If the continuous temporal distribution is selected, the simulation is comprised of a series of deposition cycles. Each deposition cycle is comprised of a deposition event and a variable number of generic diffusion events. Each deposition cycle is controlled by a critical value equal to the deposition time τ_C multiplied by a random exponential deviate. At the start of each deposition cycle, a timer value is initialized. A deposition event is completed. Generic diffusion event cycles are repeated until the timer value exceeds the critical value. If the number of completed deposition events is smaller than the number of potential deposition events, a new deposition cycle is initiated.

If the pulsed temporal distribution is selected, the simulation is comprised of a series of pulse cycles. Each pulse cycle is comprised of a number of deposition cycles followed by an annealing cycle. Each deposition cycle is comprised of a deposition event and a variable number of generic diffusion events. Each deposition cycle is controlled by a critical value equal to the deposition time τ_P multiplied by a random exponential deviate. At the start of each deposition cycle, a timer value is initialized. A deposition event is completed. Generic diffusion event cycles are repeated until the timer value exceeds the critical value. If the number of completed deposition events in the pulse cycle is smaller than the number of potential deposition events in each pulse, a new deposition cycle is initiated. If the number of completed deposition events in the pulse cycle is equal to the number of potential deposition events in each pulse, an annealing cycle is initiated. Each annealing cycle is comprised of a variable number of generic diffusion events. Each annealing cycle is controlled by a critical value equal to the deposition time τ_R. At the start of each annealing cycle, a timer value is initialized. Generic diffusion event cycles are repeated until the timer value exceeds the critical value. If the number of completed pulses is smaller than the number of potential pulses, a new pulse cycle is initiated.

2.3 Growth Morphology Metrics

Growth morphologies can be evaluated using root-mean square roughness analysis [10]. For one-dimensional surface profiles S(x) and two-dimensional surface profiles S(x,y), the root-mean square roughnesses R are equal to

$$R = <(S(x)-<S(x)>)^2>^{1/2}$$

$$R = <(S(x,y)-<S(x,y)>)^2>^{1/2}.$$

Growth morphologies can also be evaluated using Fourier height correlation analysis [10]. For one-dimensional surface profiles S(x) and two-dimensional surface profiles S(x,y), the Fourier height correlation functions $M(k_x)$ and $M(k_x,k_y)$ are equal to

$$M(k_x) = |FFT[S(x)-<S(x)>]|^2$$

$$M(k_x,k_y) = |FFT[S(x,y)-<S(x,y)>]|^2$$

where FFT represents a discrete Fourier transform. A simplified Fourier height correlation function M(k) is equal to

$$M(k) = M(k_x)$$

$$M(k) = \Sigma_k(M(k_x,0)+M(0,k_y))/2$$

where Σ_k represents a sum over the two-dimensional set of k values.

The value of the Fourier height correlation function at a value of k indicates roughness with respect to features of a size k^{-1}. The slope of the Fourier height correlation function indicates the feature size distribution. According to scaling theory, the Fourier height correlation function in log-log format should vary with k as k^0 where the feature size distribution is determined by stochastic roughening, as k^1 where the feature size distribution is determined by feature coalescence, as k^2 where the feature size distribution is determined by feature nucleation, and as k^{-4} where the feature size distribution is determined by surface diffusion smoothening [10].

2.4 Simulations

Simulation types A and B use the continuous temporal distribution at a deposition rate of 0.25 mL sec^{-1}. Simulation types C and D use the pulsed temporal distribution at a deposition coverage of 0.05 mL pls^{-1}, a repetition rate of 5.0 pls sec^{-1}, and a time-averaged deposition rate of 0.25 mL sec^{-1}. Simulation types E and F use the pulsed temporal distribution at a deposition coverage of 0.50 mL pls^{-1}, a repetition rate of 0.50 pls sec^{-1}, and a time-averaged deposition rate of 0.25 mL sec^{-1}. Simulation types A, C, and E use the thermal energy distribution. Simulation types B, D, and F use the energetic energy distribution. Simulation type A is intended to simulate molecular beam deposition. Simulation type B is intended to simulate sputter deposition. Simulation types D and F are intended to simulate pulsed laser deposition. The simulation types are described in Figure 2.7.

In each simulation, 10 mL of material was deposited on an initially flat surface. For each simulation type, ten simulations were performed at substrate temperatures of 200 °C, 300 °C, 400 °C, 500 °C, and 600 °C. For substrate temperatures of 200 °C, 300 °C, and 400 °C, a 128 atm by 128 atm cell size was used. For substrate temperatures of 500 °C and 600 °C, a 64 atm by 64 atm cell size was used to reduce computation time.

Origin was used to generate surface images [11]. Each pair of integer coordinates in the x-y plane of the image has an associated height value equal to the height of the surface atom located at the corresponding position in the x-y plane of the film. To aid interpretation, non-integer pairs of coordinates have associated height values obtained by linear interpolation of height values associated with surrounding pairs of integer coordinates. The height values are represented using a gray scale in which white represents a maximum value and black represents a minimum value.

The surface images were used to generate surface profiles S(x,y). Origin was used to determine a mean root-mean square roughness R for each simulation type at each substrate temperature [11]. Numerical Recipes was used to determine a mean Fourier height correlation function M(k) for each simulation type at substrate temperatures of 200 °C, 400 °C, and 600 °C [12]. Origin was used to linearly fit the mean Fourier height correlation functions M(k) for k values between 0.01 atm^{-1} and 0.4 atm^{-1} for each simulation type at substrate temperatures of 200 °C and 400 °C and for k values between 0.03 atm^{-1} and 0.4 atm^{-1} for each simulation type at a substrate temperature of 600 °C [11]. These k values correspond to features of 3 atm to 100 atm in size and of 3 atm to 33 atm in size, respectively. Smaller and larger k values were discarded because of possible Fourier transform edge effects and possible discrete atom effects, respectively.

Simulation Type	Energy Distribution	Temporal Distribution	Deposition Rate (mL sec^{-1})	Deposition Coverage (mL pls^{-1})	Repetition Rate (pls sec^{-1})
A	Thermal	Continuous	0.25	-	-
B	Energetic	Continuous	0.25	-	-
C	Thermal	Pulsed	0.25	0.05	5.00
D	Energetic	Pulsed	0.25	0.05	5.00
E	Thermal	Pulsed	0.25	0.50	0.50
F	Energetic	Pulsed	0.25	0.50	0.50

Figure 2.7: Simulation types A, B, C, D, E, and F.

2.5 Results

Figures 2.8 through 2.13, Figures 2.14 through 2.19, Figures 2.20 through 2.25, Figures 2.26 through 2.31, and Figures 2.32 through 2.37 show surface images representing simulation types A, B, C, D, E, and F at substrate temperatures of 200 °C, 300 °C, 400 °C, 500 °C, and 600 °C, respectively. Figures 2.8 through 2.37 indicate a transition from three-dimensional growth to two-dimensional growth as substrate temperature is increased. This transition occurred between approximately 500 °C and 600 °C for each simulation type.

Figures 2.38 and 2.39 show root-mean square roughnesses R for simulation types A, B, C, D, E, and F at substrate temperatures of 200 °C, 300 °C, 400 °C, 500 °C, and 600 °C. At 200 °C, R is approximately 2.9 mL for simulation types A, C, and E and approximately 1.5 mL for simulation types B, D, and F, indicating that pulsed roughening does not significantly affect roughness and that energetic smoothening decreases roughness. At 400 °C, R ranges between approximately 0.9 mL for simulation type B and approximately 2.1 mL for simulation type E, indicating that both pulsed roughening and energetic smoothening affect roughness. At 600 °C, R is approximately 0.2 mL for simulation types A and B and approximately 0.4 mL for simulation types C, D, E, and F, indicating that pulsed roughening increases roughness and that energetic smoothening does not significantly affect roughness.

Figures 2.40 through 2.42 show Fourier height correlation functions M(k) for simulation types A, B, C, D, E, and F at substrate temperatures of 200 °C, 400 °C, and 600 °C, respectively. Figures 2.43 through 2.45 show Fourier height correlation function M(k) linear fit exponents for simulation types A, B, C, D, E, and F at substrate temperatures of 200 °C, 400 °C, and 600 °C, respectively.

At 200 °C, for features smaller than approximately 10 atm, M(k) is characterized by negative exponents, indicating a net smoothening effect. The exponents decrease with energy, indicating that energetic smoothening affects the feature size distribution. For simulation types A, C, and E, the exponents increase with pulsing degree, indicating that pulsed roughening affects the feature size distribution. For simulation types B, D, and F, the exponents do not vary significantly with pulsing degree, indicating that pulsed roughening does not significantly affect the feature size distribution. M(k) is approximately equal for simulation types A, C, and E and approximately equal for simulation types B, D, and F, indicating that pulsed roughening does not significantly affect roughness on these feature size scales. M(k) for simulation types A, C, and E is larger than M(k) for simulation types B, D, and F, indicating that energetic smoothening decreases roughness on these feature size scales.

At 200 °C, for features larger than approximately 10 atm, M(k) is characterized by positive exponents, indicating a net roughening effect. The exponents decrease with energy, indicating that energetic smoothening affects the feature size distribution. For simulation types A, C, and E, the exponents decrease with pulsing degree, indicating that pulsed roughening affects the feature size distribution. For simulation types B, D, and F, the exponents do not vary significantly with pulsing degree, indicating that pulsed roughening does not significantly affect the feature size distribution. M(k) is approximately equal for simulation types A, B, C, D, E, and F, indicating that energetic smoothening and pulsed roughening do not significantly affect roughness on these feature size scales.

At 400 °C, for features smaller than approximately 20 atm, M(k) is characterized by negative exponents, indicating a net smoothening effect. The exponents do not vary significantly with energy or pulsing degree, indicating that energetic smoothening and pulsed roughening do not significantly affect the feature size distribution. M(k) ranges from smallest to largest for simulation types B, D, F, A, C, and E, respectively, and is approximately equal for simulation types A and F, indicating that energetic smoothening decreases roughness on these feature size scales and that pulsed roughening increases roughness on these feature size scales.

At 400 °C, for features larger than approximately 20 atm, M(k) is characterized by positive exponents, indicating a net roughening effect. The exponents decrease with energy, indicating that energetic smoothening affects the feature size distribution. For simulation types A, C, and E, the exponents decrease with pulsing degree, indicating that pulsed roughening affects the feature size distribution. For simulation types B, D, and F, the exponents do not vary significantly with pulsing degree, indicating that pulsed roughening does not significantly affect the feature size distribution. M(k) is approximately equal for simulation types A and B, approximately equal for simulation types C and D, and approximately equal for simulation types E and F, indicating that energetic smoothening does not significantly affect roughness on these feature size scales. M(k) ranges from largest to smallest for simulation types A and B, C and D, and E and F, respectively, indicating that pulsed roughening decreases roughness on these feature size scales, most likely by suppressing nonstochastic roughening.

At 600 °C, M(k) is characterized by negative exponents, indicating a net smoothening effect. The exponents do not vary significantly with energy or pulsing degree, indicating that energetic smoothening and pulsed roughening do not significantly affect the feature size distribution. M(k) is approximately equal for simulation types A and B and approximately equal for simulation types C, D, E, and F, indicating that energetic smoothening does not significantly affect roughness on these feature size scales. M(k) is smaller for simulation types A and B than for simulation types C, D, E, and F, indicating that pulsed roughening increases roughness on these feature size scales.

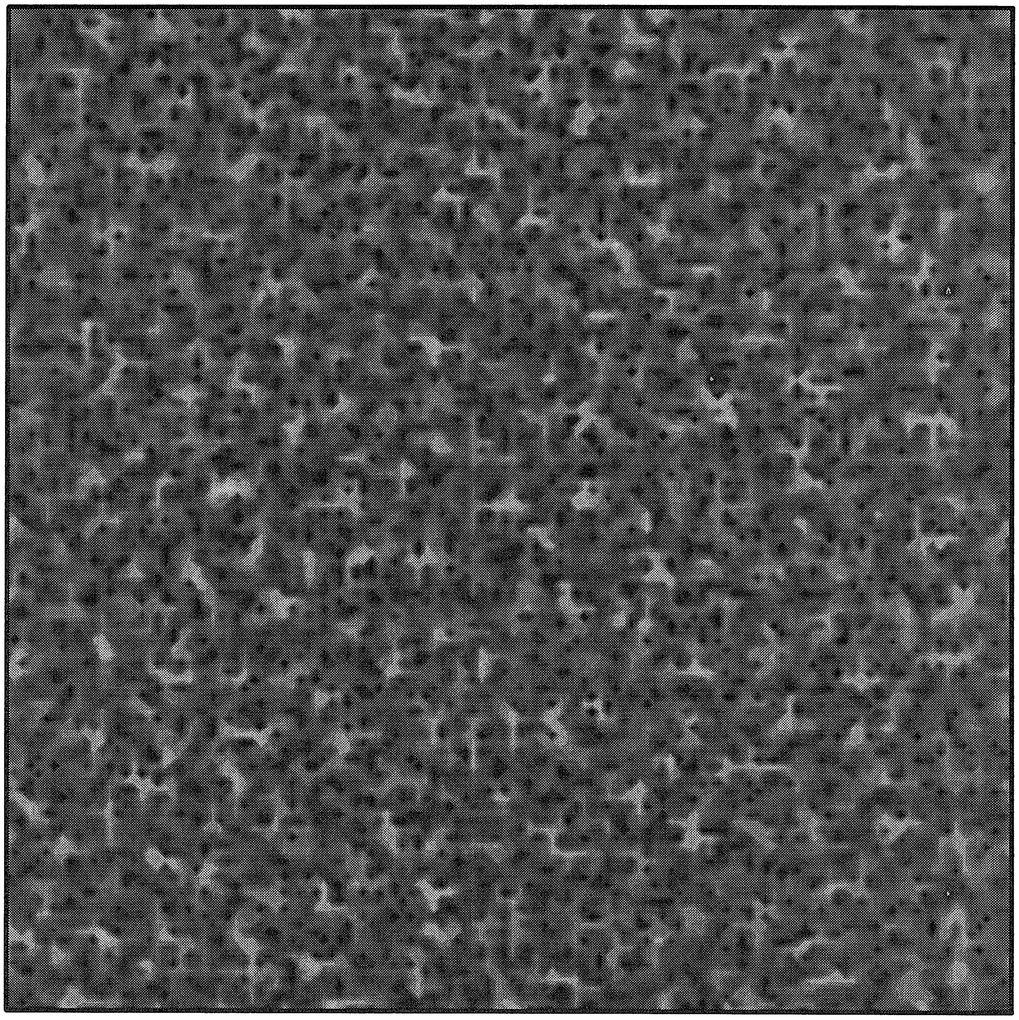

Figure 2.8: Surface image of a type A simulation at a substrate temperature of 200 °C. The simulation cell size is 128 atm by 128 atm. Black and white represent thicknesses of 0 mL and 22 mL, respectively.

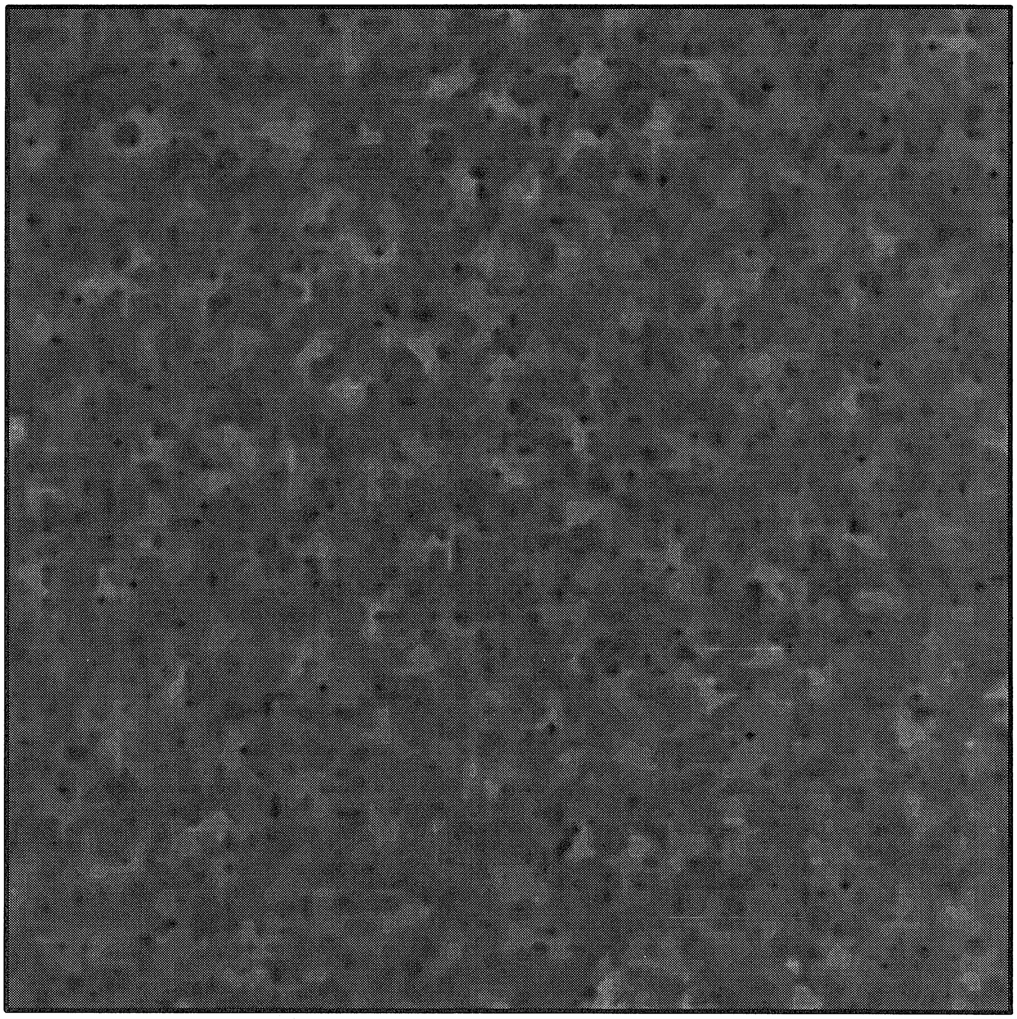

Figure 2.9: Surface image of a type B simulation at a substrate temperature of 200 °C. The simulation cell size is 128 atm by 128 atm. Black and white represent thicknesses of 0 mL and 22 mL, respectively.

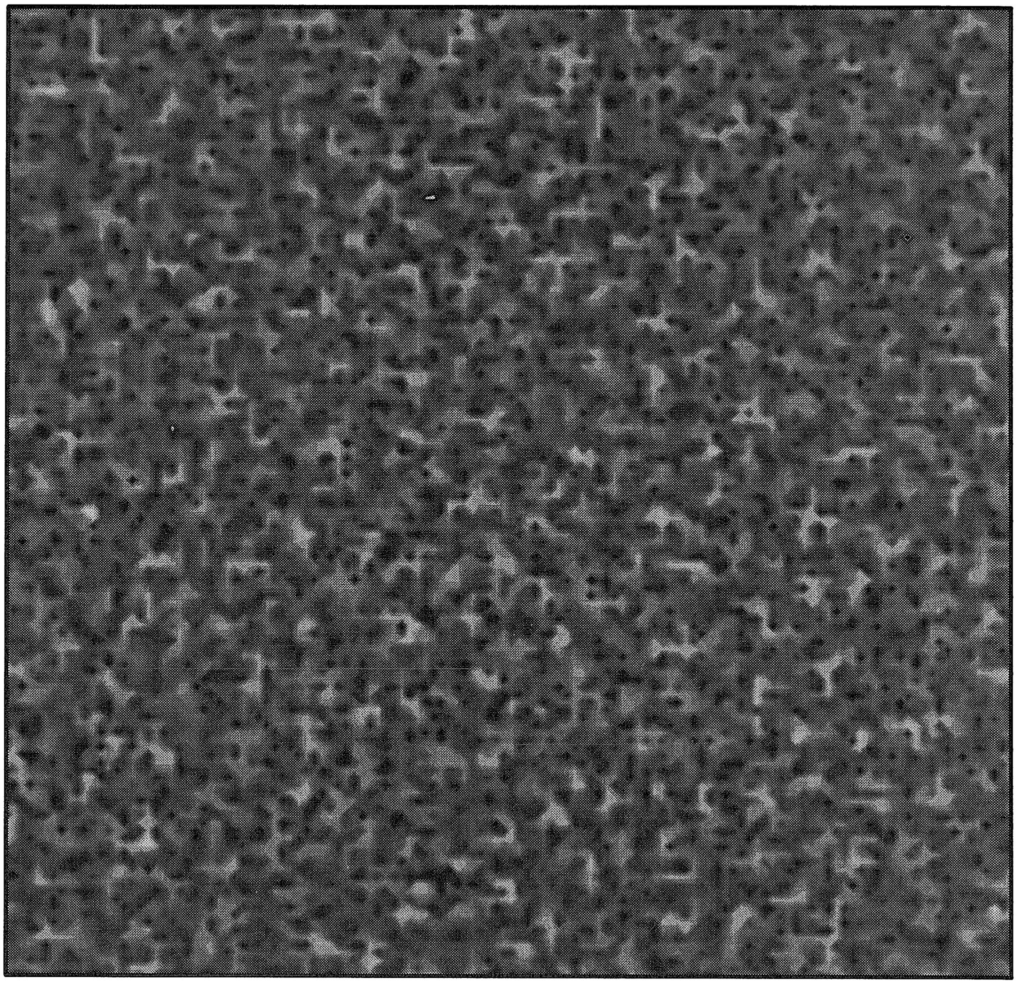

Figure 2.10: Surface image of a type C simulation at a substrate temperature of 200 °C. The simulation cell size is 128 atm by 128 atm. Black and white represent thicknesses of 0 mL and 22 mL, respectively.

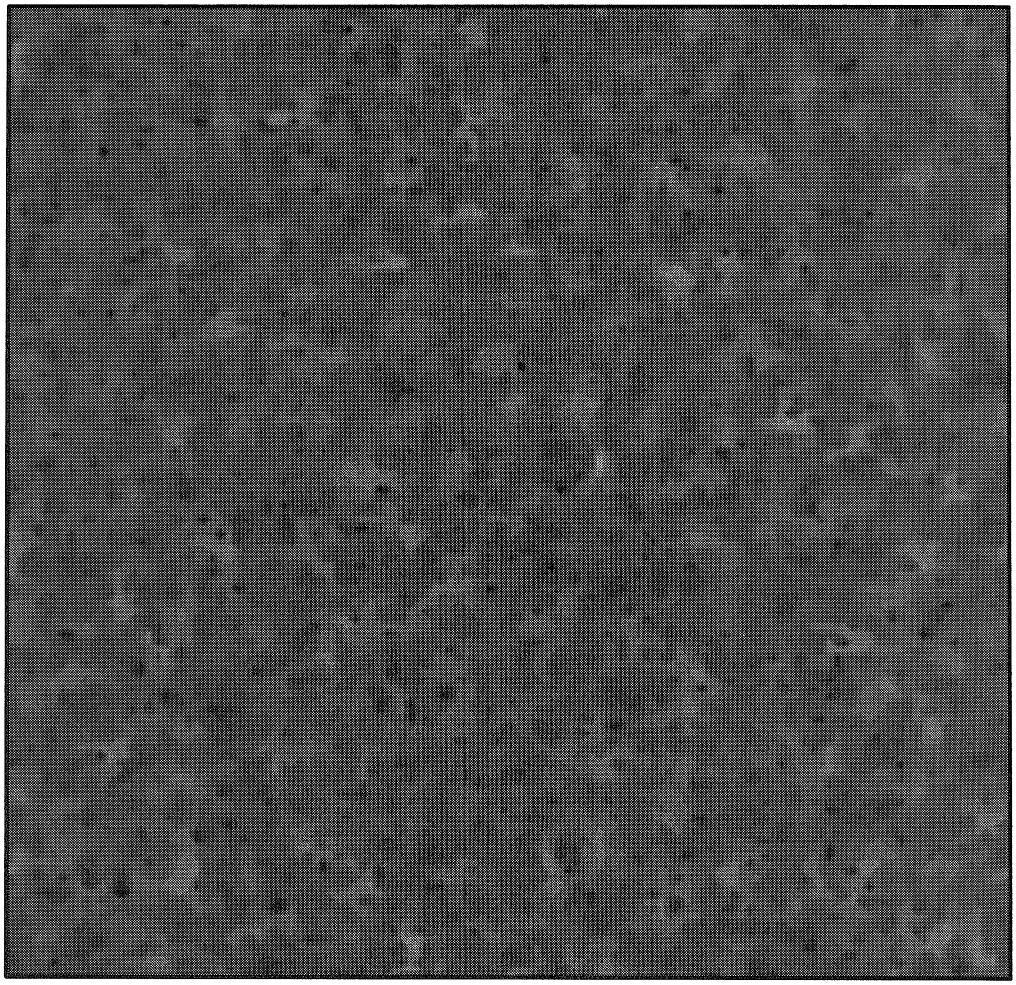

Figure 2.11: Surface image of a type D simulation at a substrate temperature of 200 ^{o}C. The simulation cell size is 128 atm by 128 atm. Black and white represent thicknesses of 0 mL and 22 mL, respectively.

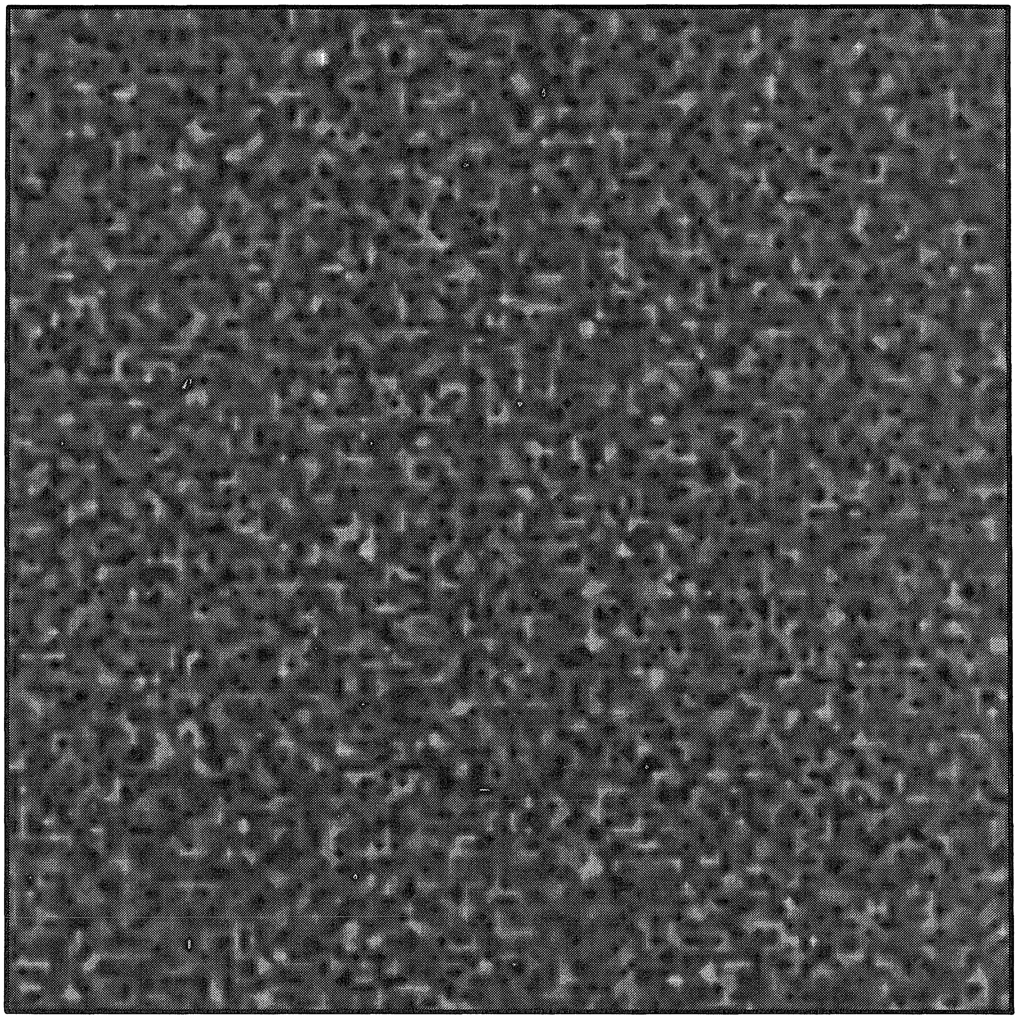

Figure 2.12: Surface image of a type E simulation at a substrate temperature of 200 °C. The simulation cell size is 128 atm by 128 atm. Black and white represent thicknesses of 0 mL and 22 mL, respectively.

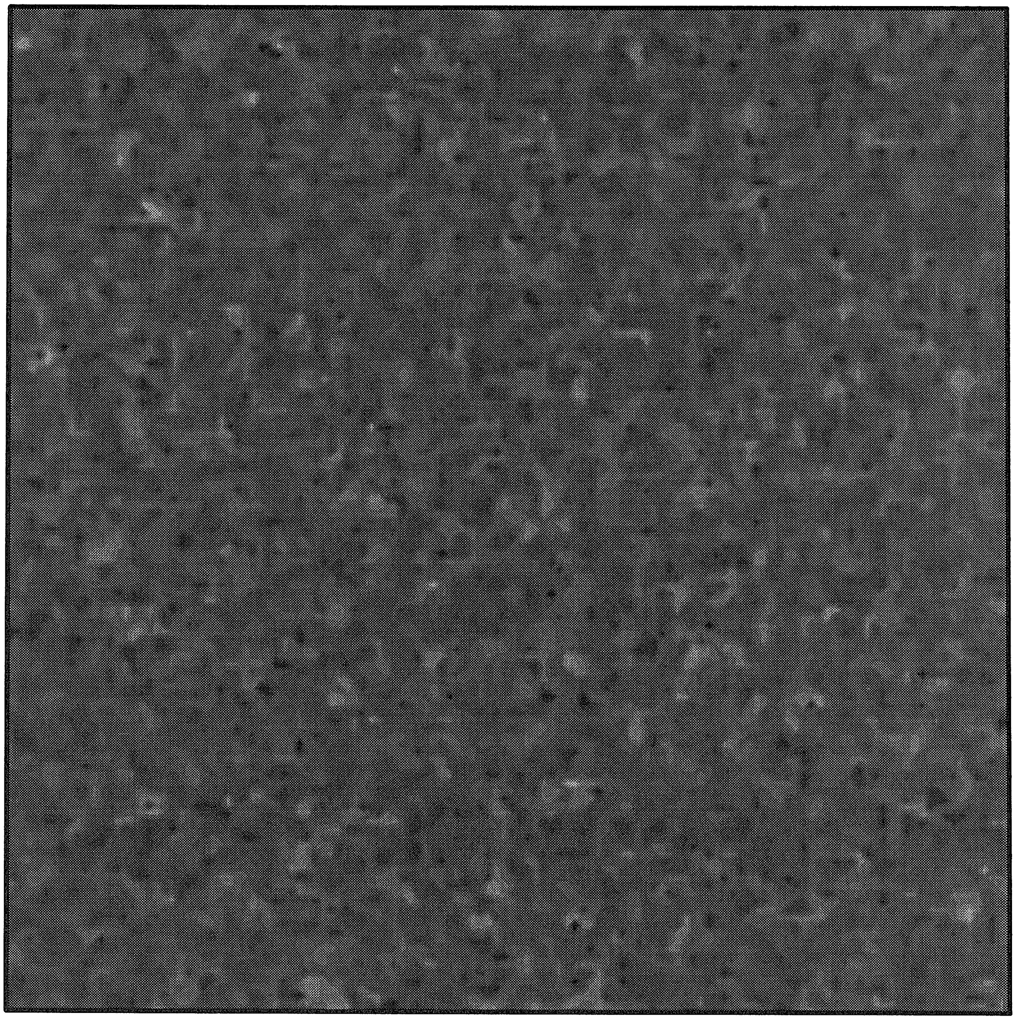

Figure 2.13: Surface image of a type F simulation at a substrate temperature of 200 °C. The simulation cell size is 128 atm by 128 atm. Black and white represent thicknesses of 0 mL and 22 mL, respectively.

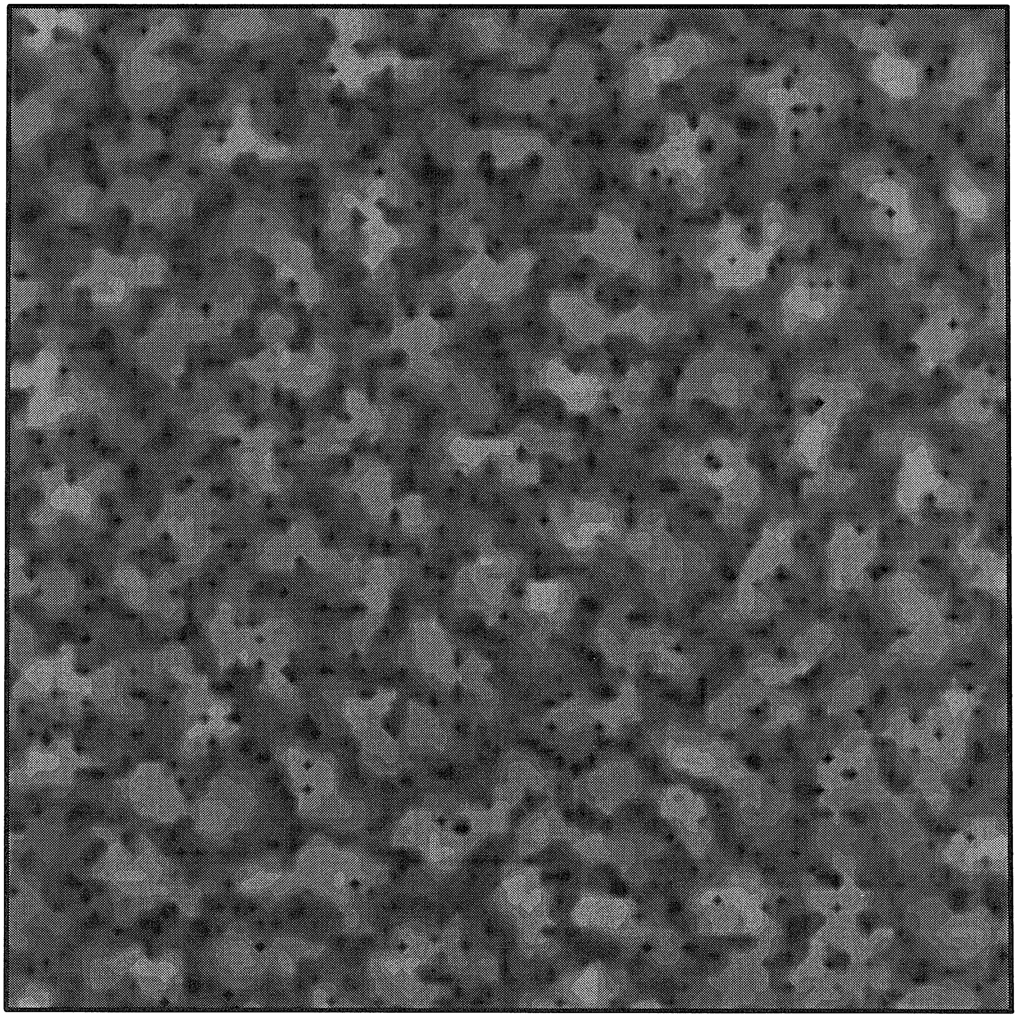

Figure 2.14: Surface image of a type A simulation at a substrate temperature of 300 °C. The simulation cell size is 128 atm by 128 atm. Black and white represent thicknesses of 0 mL and 20 mL, respectively.

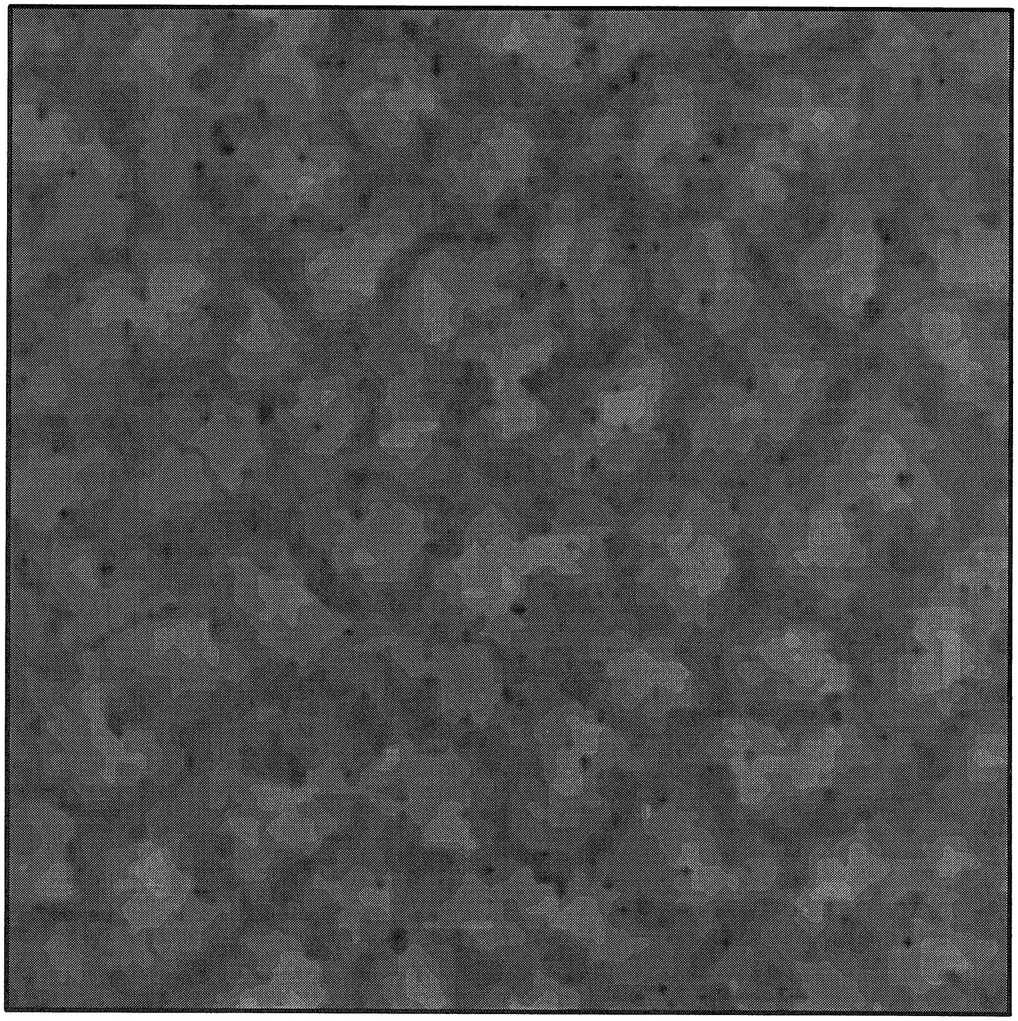

Figure 2.15: Surface image of a type B simulation at a substrate temperature of 300 °C. The simulation cell size is 128 atm by 128 atm. Black and white represent thicknesses of 0 mL and 20 mL, respectively.

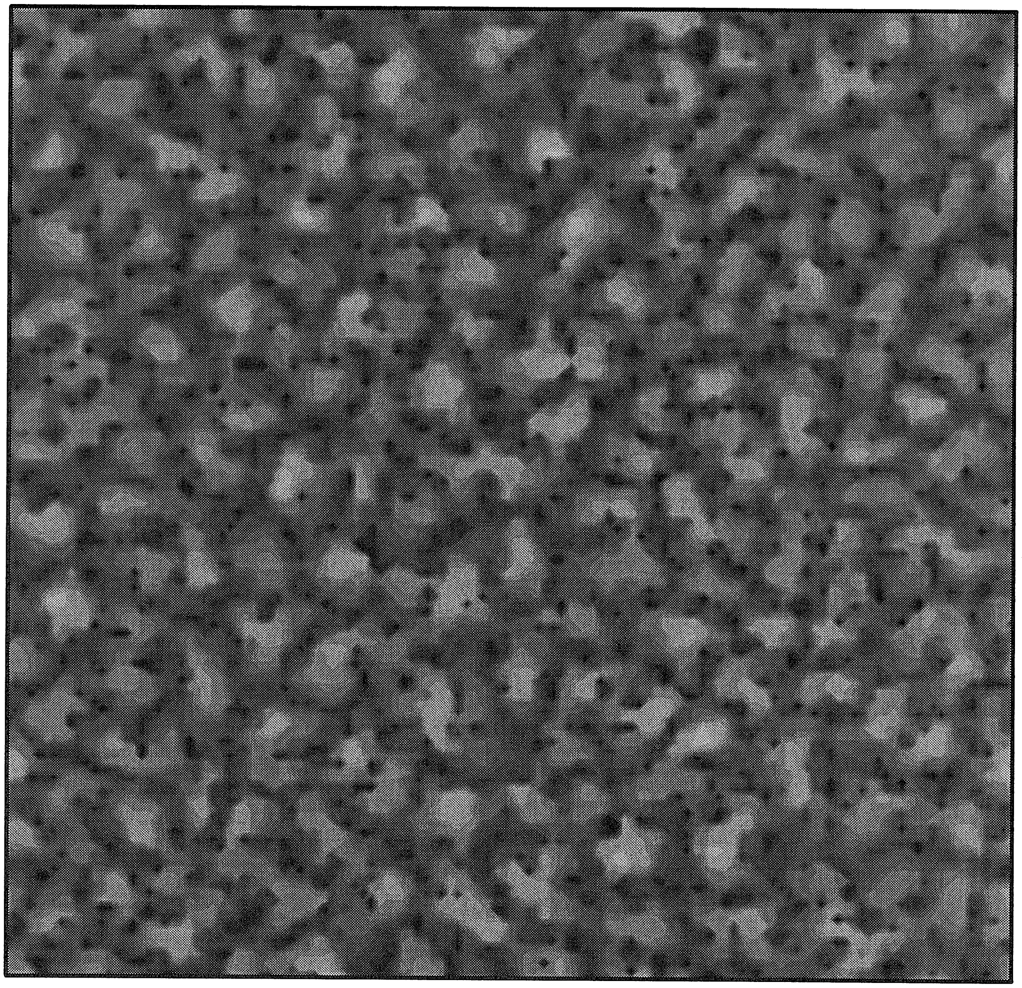

Figure 2.16: Surface image of a type C simulation at a substrate temperature of 300 °C. The simulation cell size is 128 atm by 128 atm. Black and white represent thicknesses of 0 mL and 20 mL, respectively.

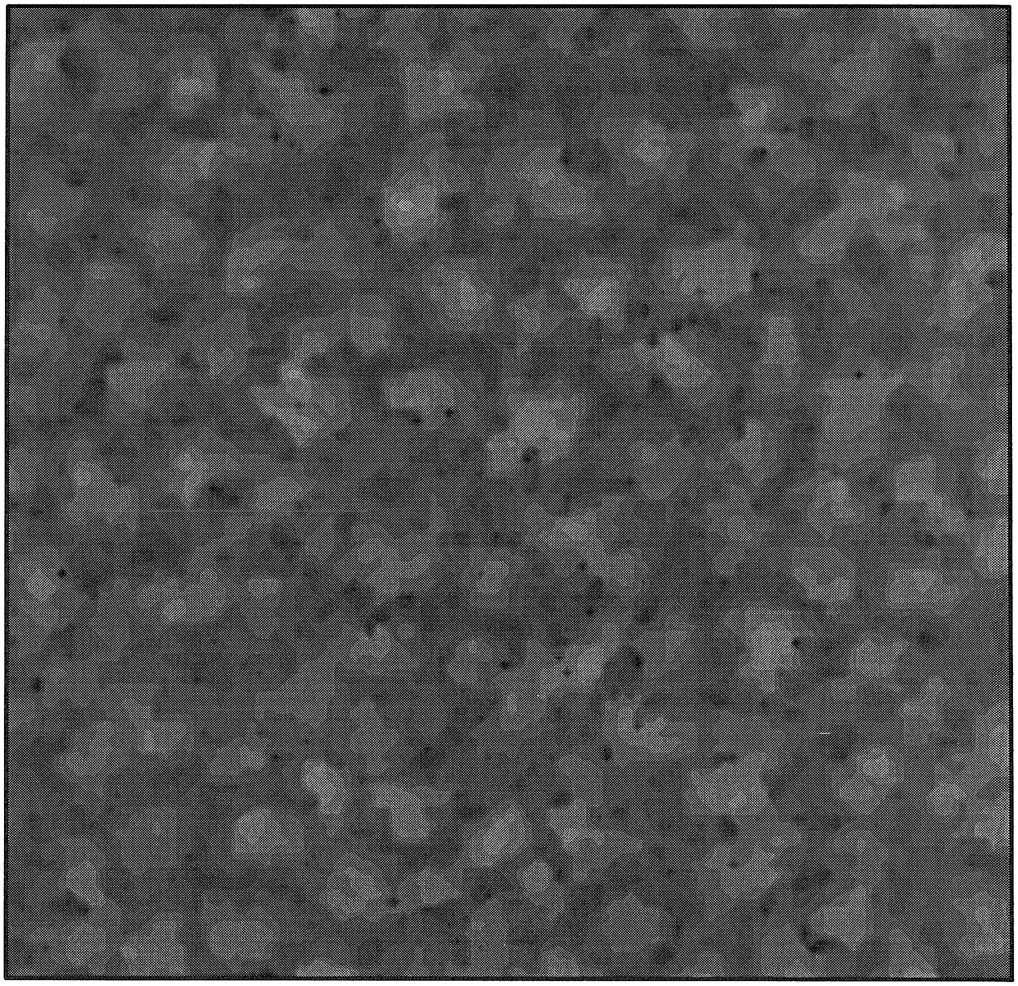

Figure 2.17: Surface image of a type D simulation at a substrate temperature of 300 °C. The simulation cell size is 128 atm by 128 atm. Black and white represent thicknesses of 0 mL and 20 mL, respectively.

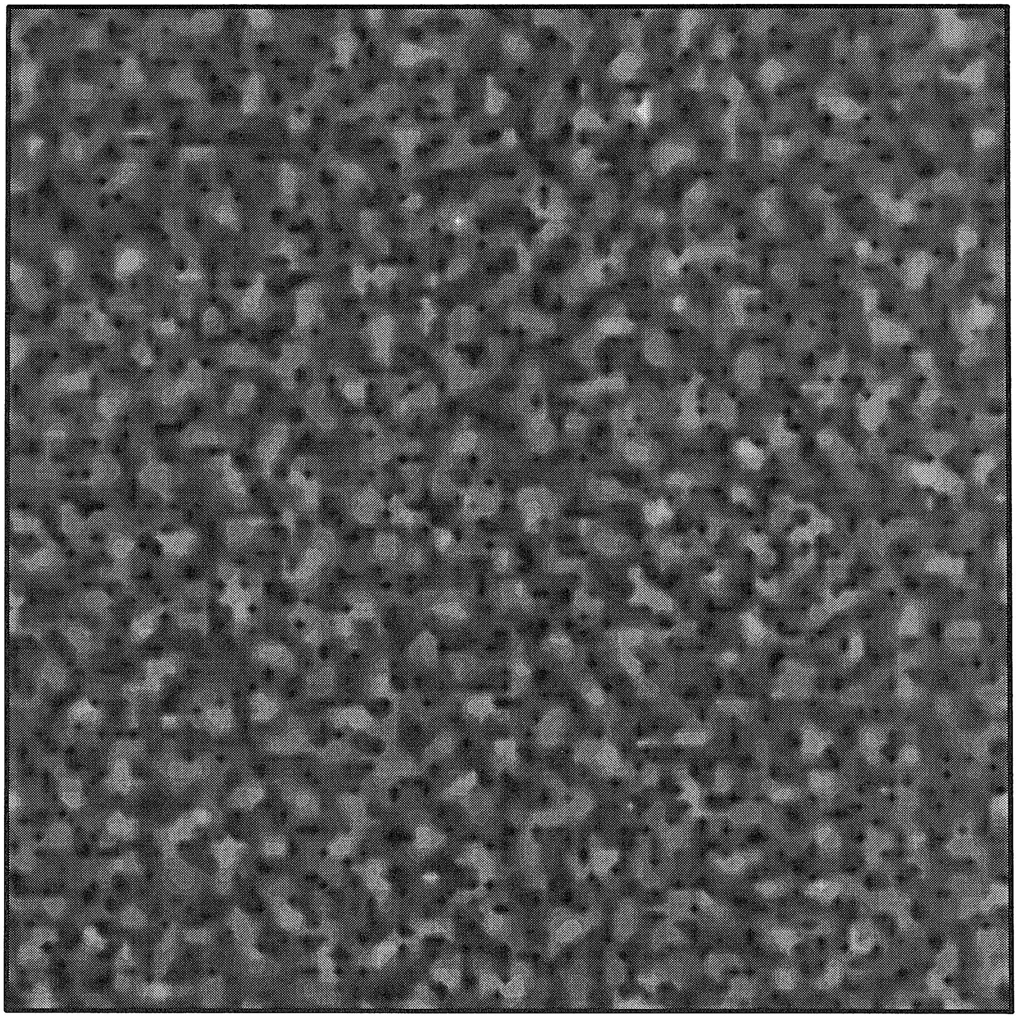

Figure 2.18: Surface image of a type E simulation at a substrate temperature of 300 °C. The simulation cell size is 128 atm by 128 atm. Black and white represent thicknesses of 0 mL and 20 mL, respectively.

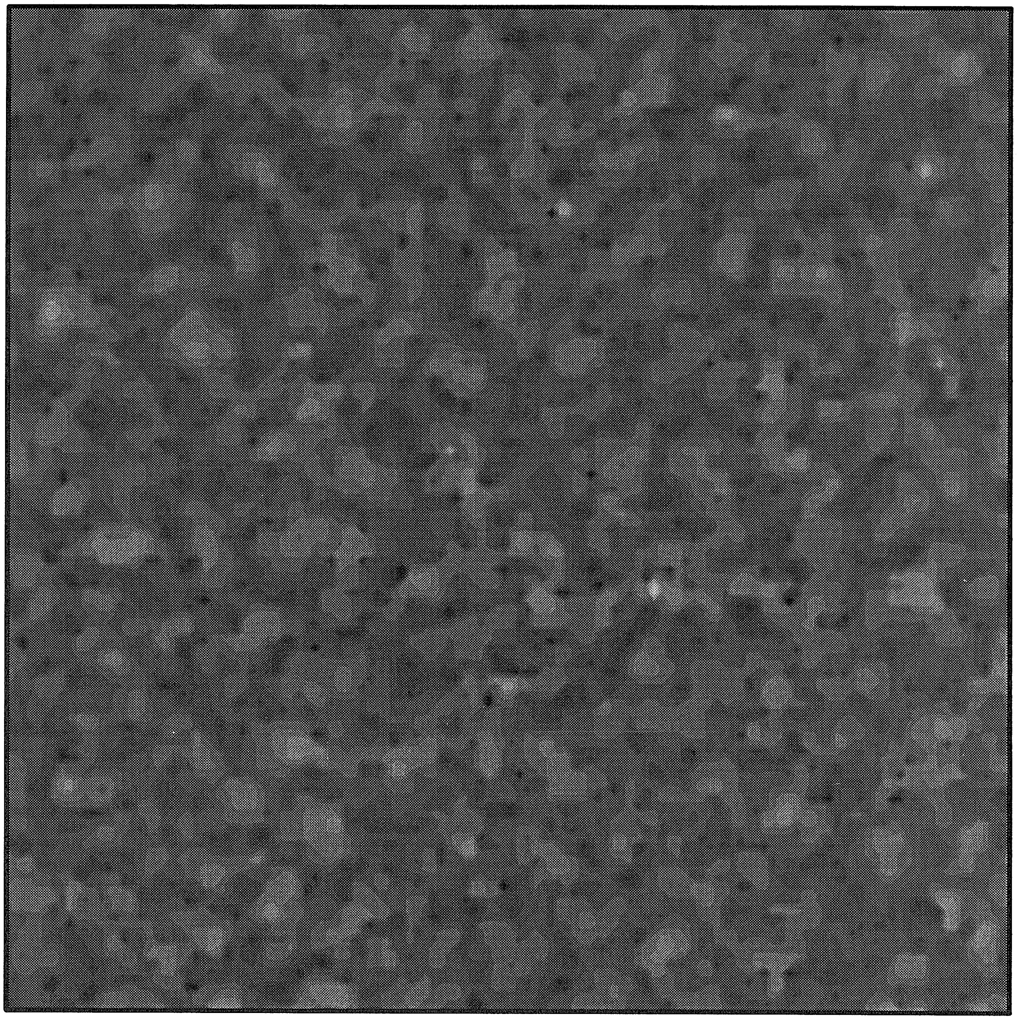

Figure 2.19: Surface image of a type F simulation at a substrate temperature of 300 °C. The simulation cell size is 128 atm by 128 atm. Black and white represent thicknesses of 0 mL and 20 mL, respectively.

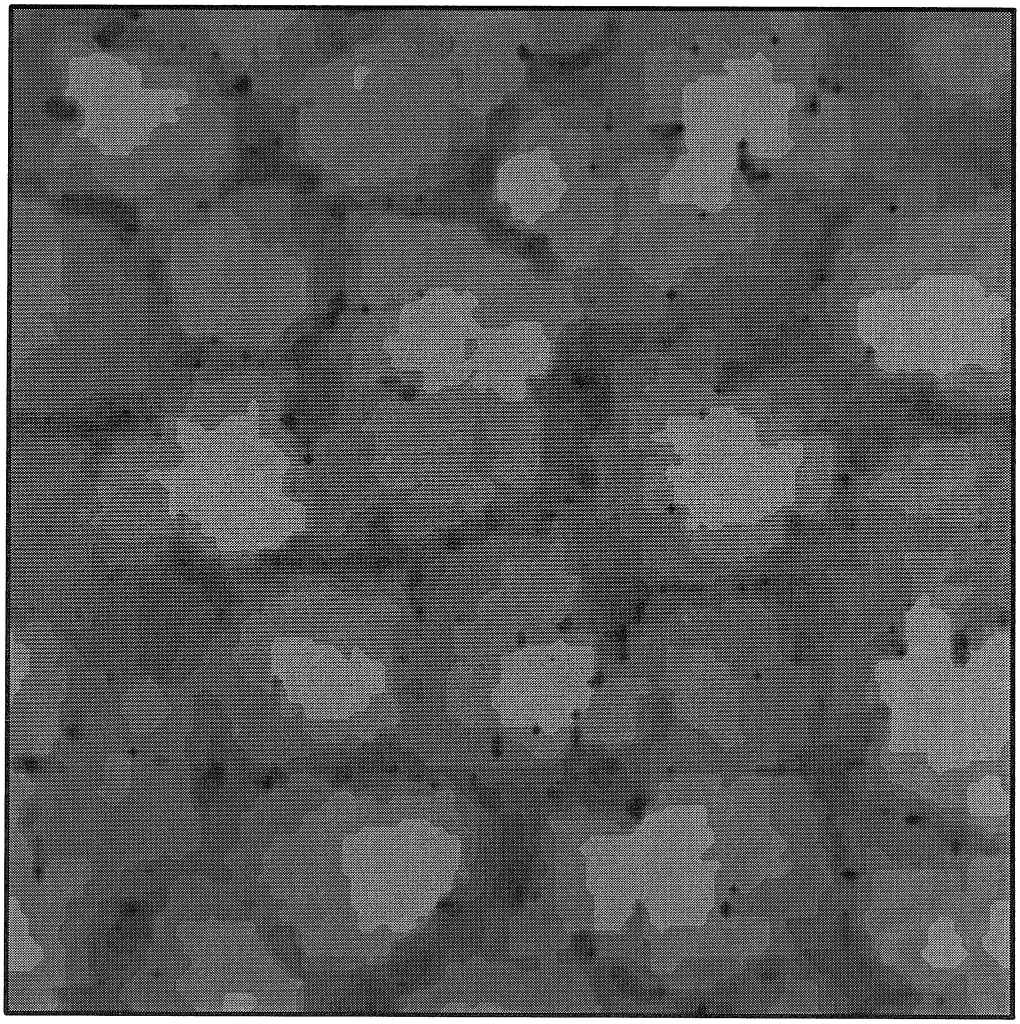

Figure 2.20: Surface image of a type A simulation at a substrate temperature of 400 °C. The simulation cell size is 128 atm by 128 atm. Black and white represent thicknesses of 0 mL and 18 mL, respectively.

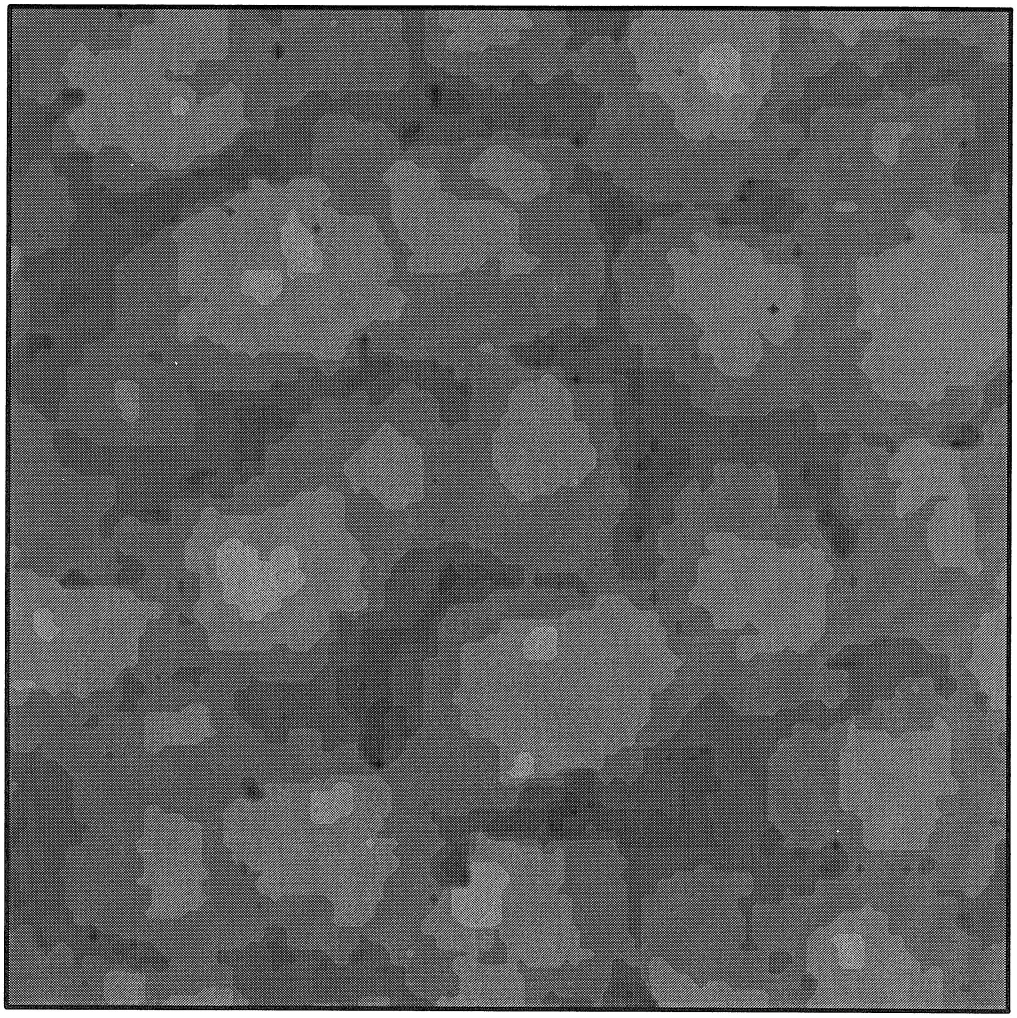

Figure 2.21: Surface image of a type B simulation at a substrate temperature of 400 °C. The simulation cell size is 128 atm by 128 atm. Black and white represent thicknesses of 0 mL and 18 mL, respectively.

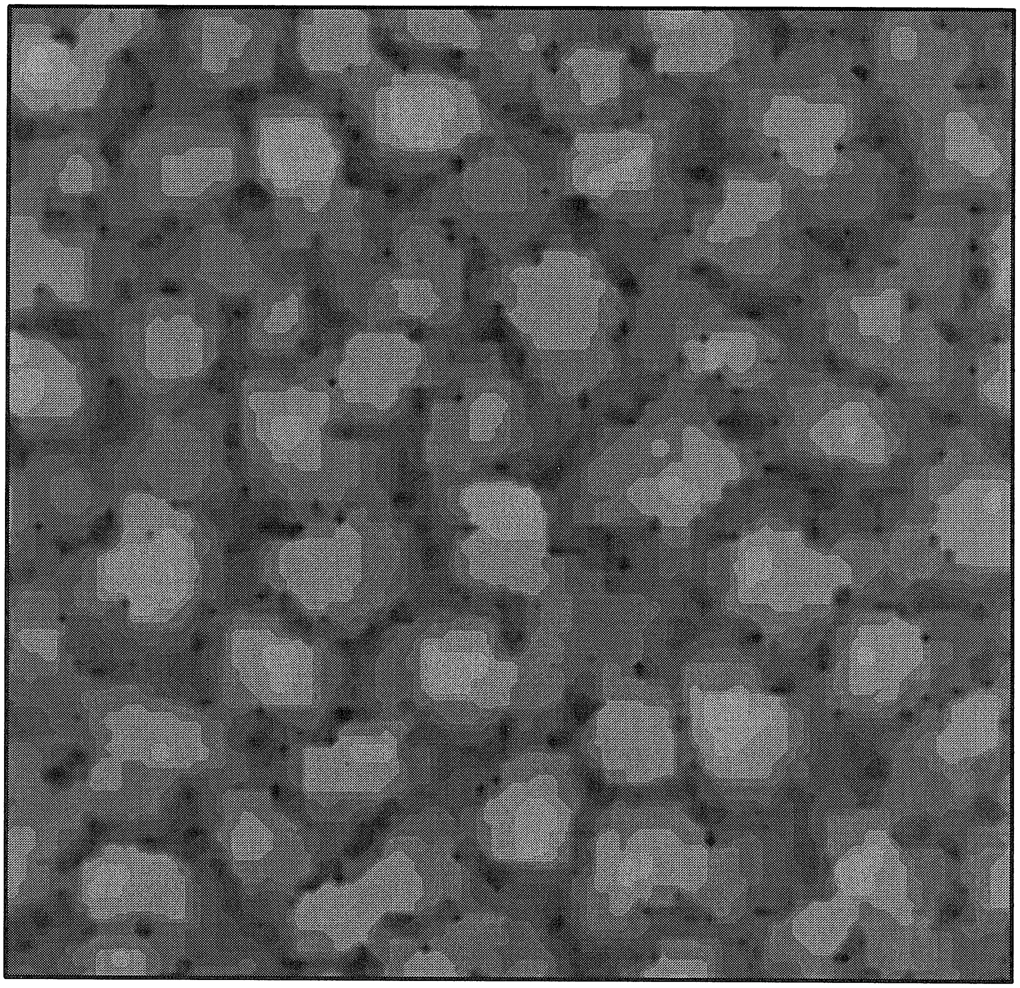

Figure 2.22: Surface image of a type C simulation at a substrate temperature of 400 °C. The simulation cell size is 128 atm by 128 atm. Black and white represent thicknesses of 0 mL and 18 mL, respectively.

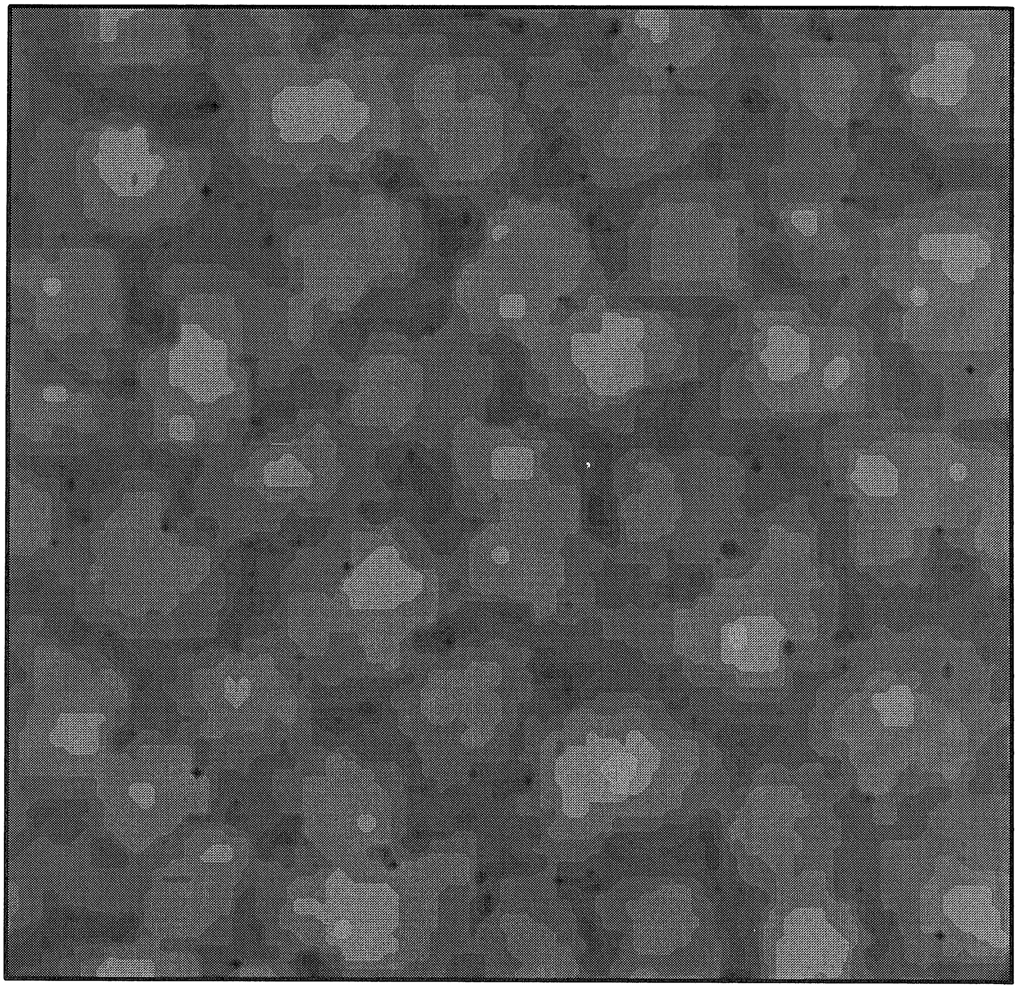

Figure 2.23: Surface image of a type D simulation at a substrate temperature of 400 °C. The simulation cell size is 128 atm by 128 atm. Black and white represent thicknesses of 0 mL and 18 mL, respectively.

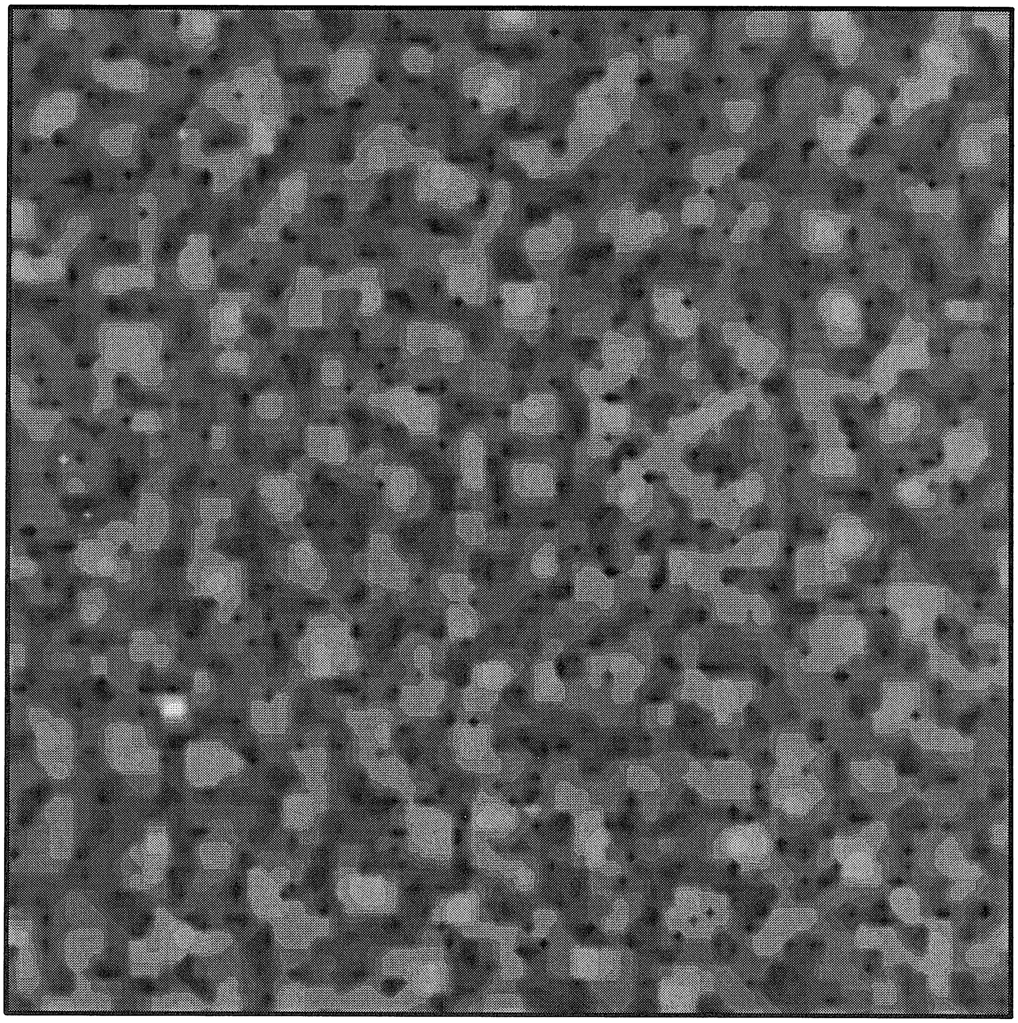

Figure 2.24: Surface image of a type E simulation at a substrate temperature of 400 °C. The simulation cell size is 128 atm by 128 atm. Black and white represent thicknesses of 0 mL and 18 mL, respectively.

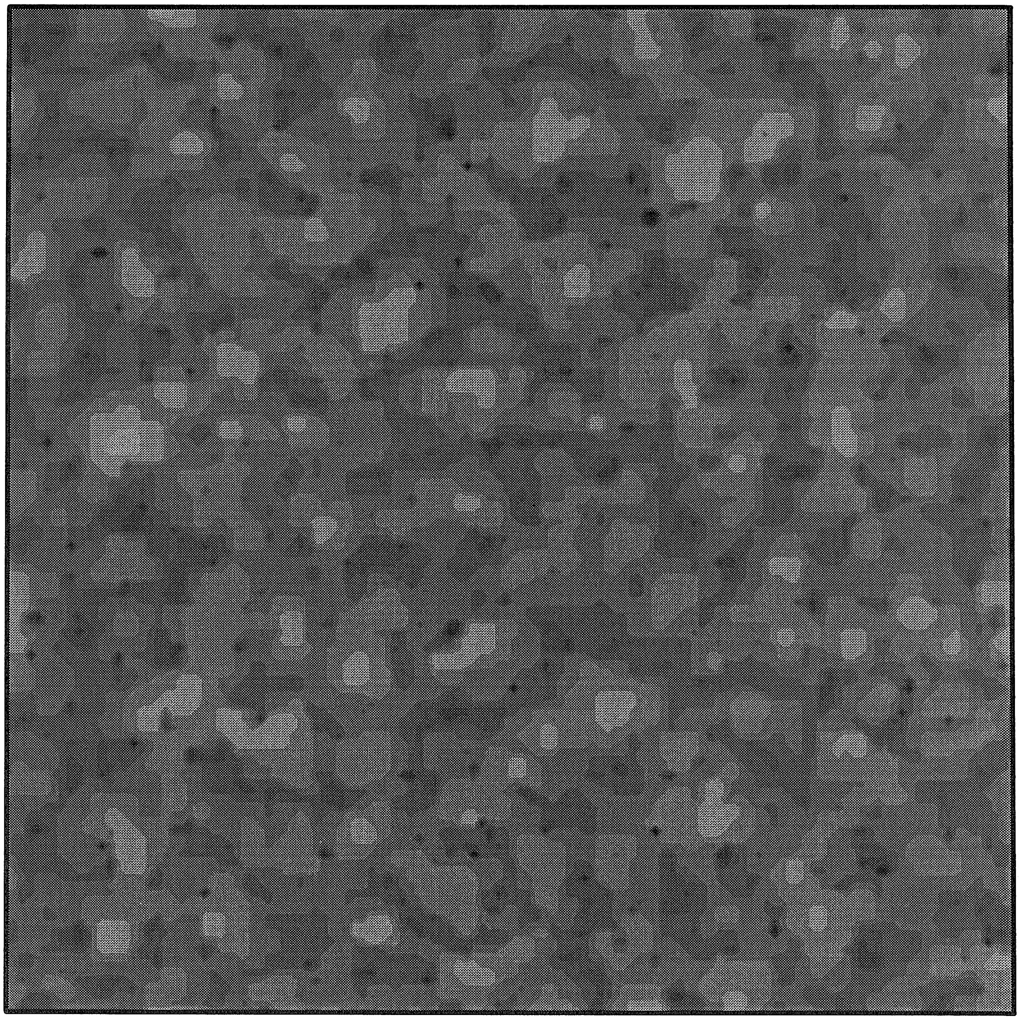

Figure 2.25: Surface image of a type F simulation at a substrate temperature of 400 °C. The simulation cell size is 128 atm by 128 atm. Black and white represent thicknesses of 0 mL and 18 mL, respectively.

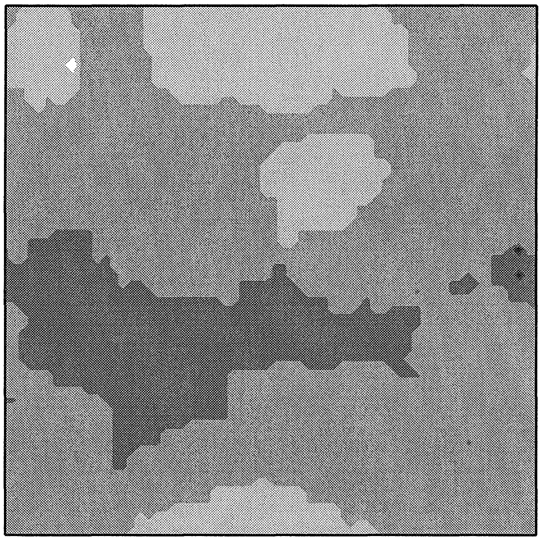

Figure 2.26: Surface image of a type A simulation at a substrate temperature of 500 °C. The simulation cell size is 64 atm by 64 atm. Black and white represent thicknesses of 4 mL and 12 mL, respectively.

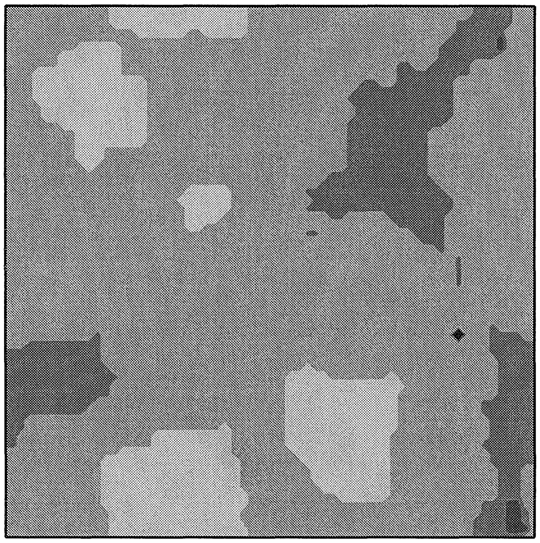

Figure 2.27: Surface image of a type B simulation at a substrate temperature of 500 °C. The simulation cell size is 64 atm by 64 atm. Black and white represent thicknesses of 4 mL and 12 mL, respectively.

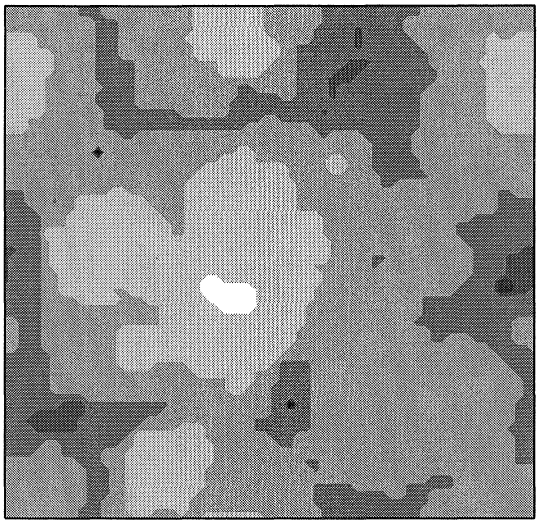

Figure 2.28: Surface image of a type C simulation at a substrate temperature of 500 °C. The simulation cell size is 64 atm by 64 atm. Black and white represent thicknesses of 4 mL and 12 mL, respectively.

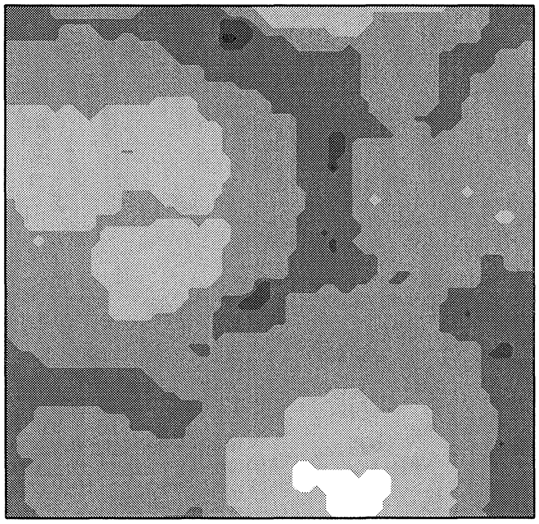

Figure 2.29: Surface image of a type D simulation at a substrate temperature of 500 °C. The simulation cell size is 64 atm by 64 atm. Black and white represent thicknesses of 4 mL and 12 mL, respectively.

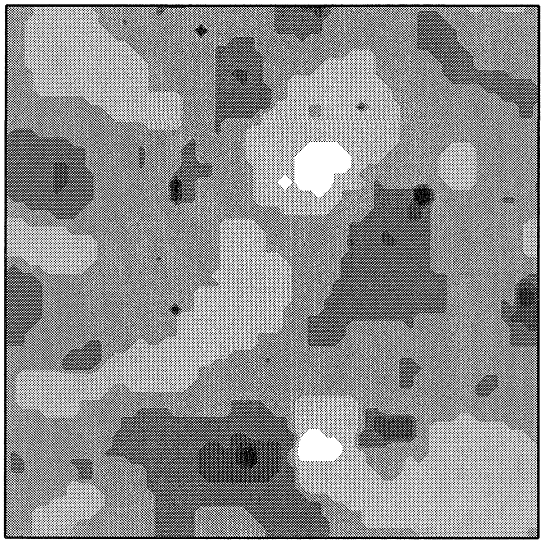

Figure 2.30: Surface image of a type E simulation at a substrate temperature of 500 °C. The simulation cell size is 64 atm by 64 atm. Black and white represent thicknesses of 4 mL and 12 mL, respectively.

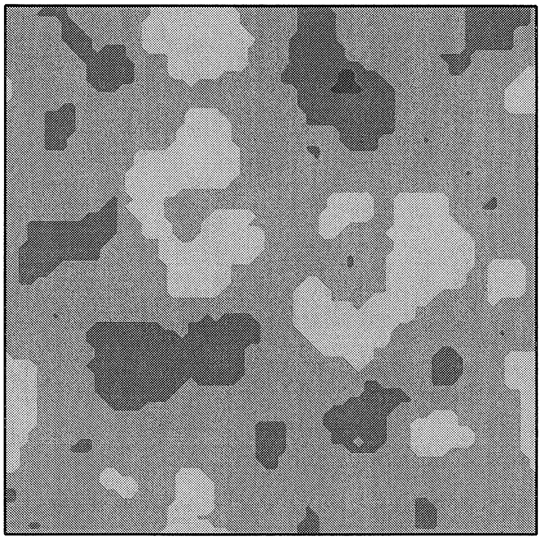

Figure 2.31: Surface image of a type F simulation at a substrate temperature of 500 °C. The simulation cell size is 64 atm by 64 atm. Black and white represent thicknesses of 4 mL and 12 mL, respectively.

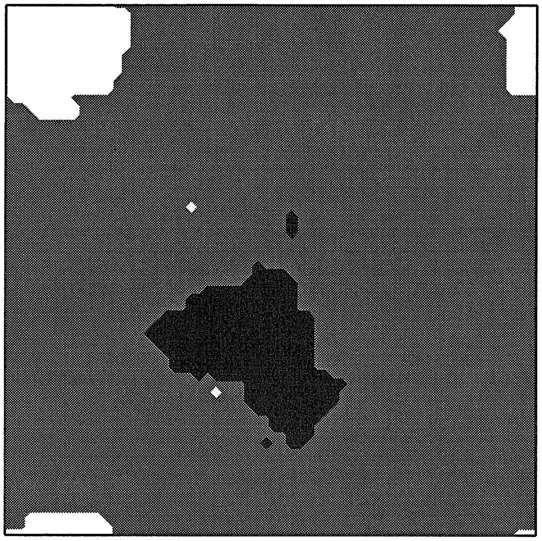

Figure 2.32: Surface image of a type A simulation at a substrate temperature of 600 °C. The simulation cell size is 64 atm by 64 atm. Black and white represent thicknesses of 9 mL and 11 mL, respectively.

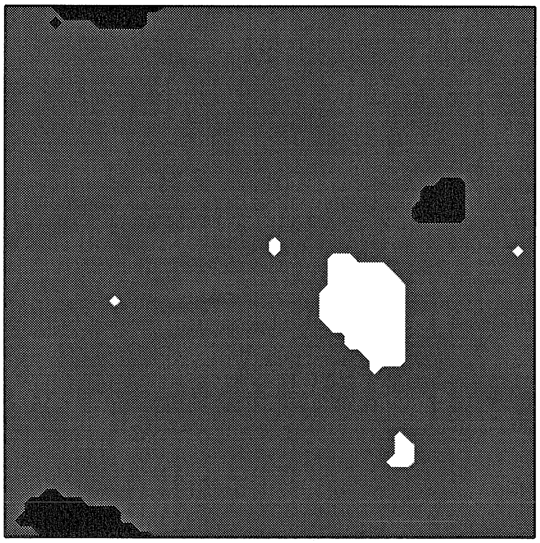

Figure 2.33: Surface image of a type B simulation at a substrate temperature of 600 °C. The simulation cell size is 64 atm by 64 atm. Black and white represent thicknesses of 9 mL and 11 mL, respectively.

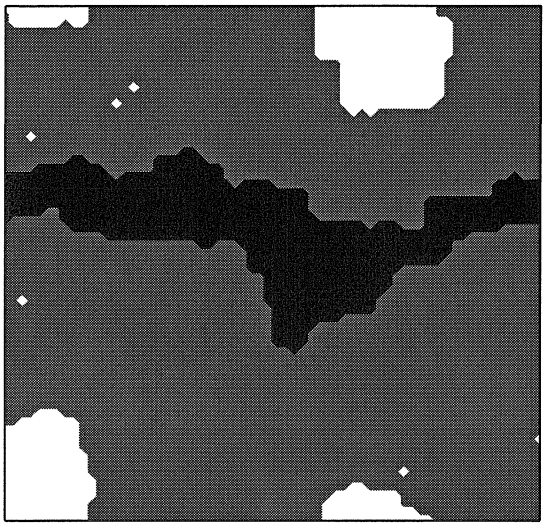

Figure 2.34: Surface image of a type C simulation at a substrate temperature of 600 °C. The simulation cell size is 64 atm by 64 atm. Black and white represent thicknesses of 9 mL and 11 mL, respectively.

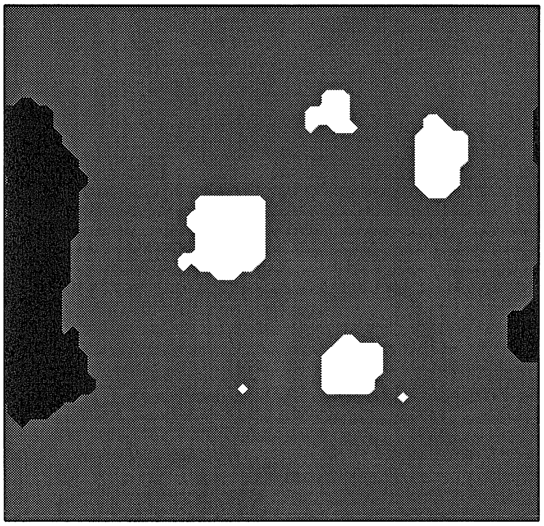

Figure 2.35: Surface image of a type D simulation at a substrate temperature of 600 °C. The simulation cell size is 64 atm by 64 atm. Black and white represent thicknesses of 9 mL and 11 mL, respectively.

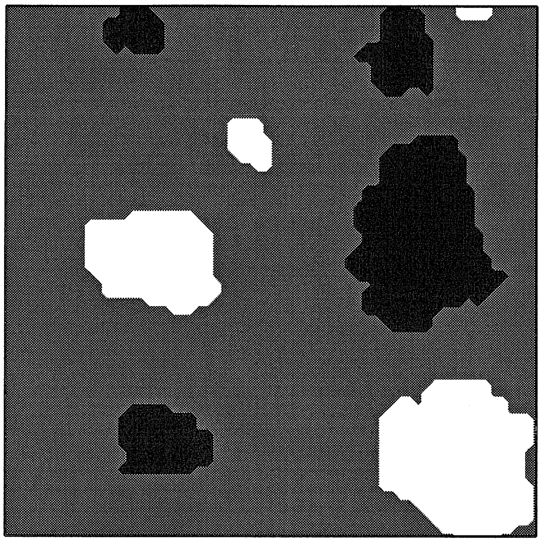

Figure 2.36: Surface image of a type E simulation at a substrate temperature of 600 °C. The simulation cell size is 64 atm by 64 atm. Black and white represent thicknesses of 9 mL and 11 mL, respectively.

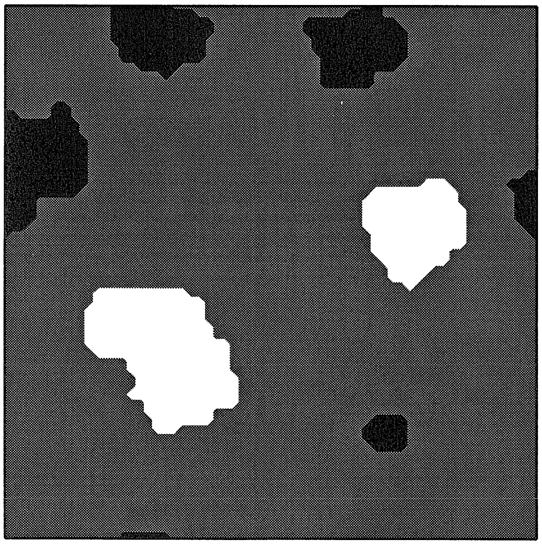

Figure 2.37: Surface image of a type F simulation at a substrate temperature of 600 °C. The simulation cell size is 64 atm by 64 atm. Black and white represent thicknesses of 9 mL and 11 mL, respectively.

Simulation Type	200 °C R (mL)	300 °C R (mL)	400 °C R (mL)	500 °C R (mL)	600 °C R (mL)
A	2.936 ± 0.006	2.446 ± 0.006	1.417 ± 0.010	0.567 ± 0.033	0.231 ± 0.023
B	1.475 ± 0.004	1.348 ± 0.005	0.931 ± 0.009	0.515 ± 0.024	0.212 ± 0.013
C	2.902 ± 0.003	2.598 ± 0.007	1.861 ± 0.007	0.793 ± 0.033	0.468 ± 0.022
D	1.429 ± 0.007	1.398 ± 0.007	1.114 ± 0.008	0.670 ± 0.028	0.395 ± 0.026
E	2.938 ± 0.006	2.622 ± 0.006	2.110 ± 0.006	0.753 ± 0.013	0.375 ± 0.014
F	1.454 ± 0.004	1.295 ± 0.007	1.076 ± 0.004	0.594 ± 0.017	0.376 ± 0.026

Figure 2.38: Root-mean square roughnesses for simulation types A, B, C, D, E, and F at substrate temperatures of 200 °C, 300 °C, 400 °C, 500 °C, and 600 °C.

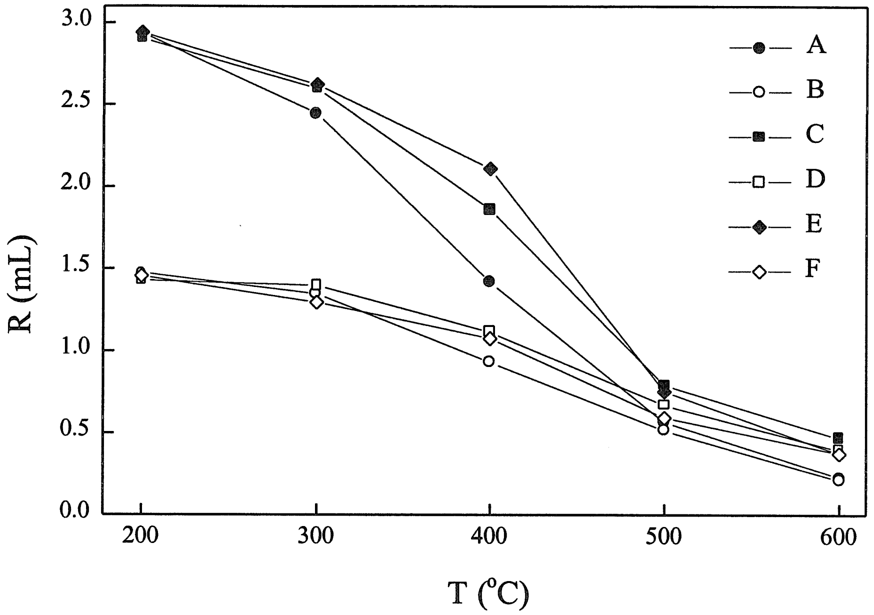

Figure 2.39: Root-mean square roughnesses for simulation types A, B, C, D, E, and F at substrate temperatures of 200 °C, 300 °C, 400 °C, 500 °C, and 600 °C.

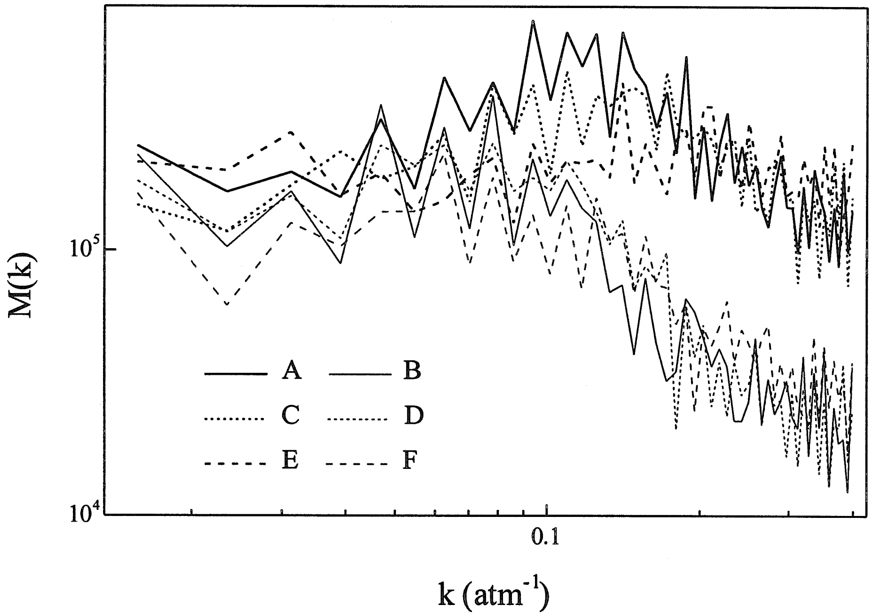

Figure 2.40: Fourier height correlation functions for simulation types A, B, C, D, E, and F at a substrate temperature of 200 °C.

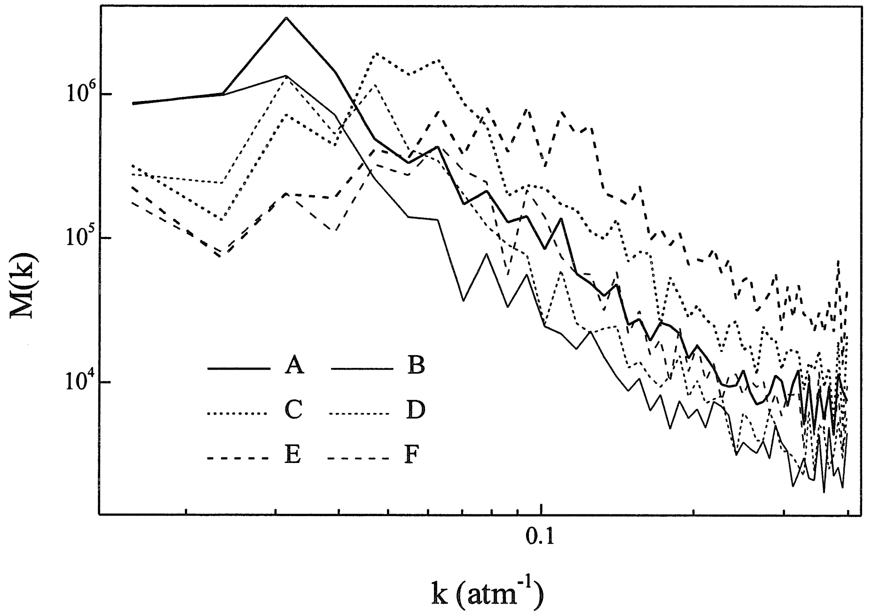

Figure 2.41: Fourier height correlation functions for simulation types A, B, C, D, E, and F at a substrate temperature of 400 °C.

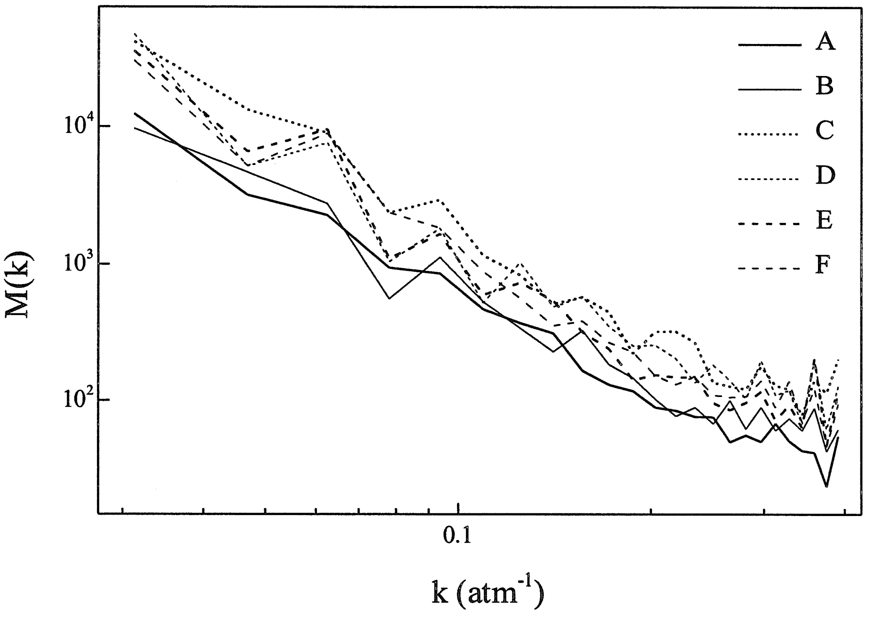

Figure 2.42: Fourier height correlation functions for simulation types A, B, C, D, E, and F at a substrate temperature of 600 °C.

Simulation Type	k (atm^{-1})	x (atm)	Linear Fit Exponent
A	0.01 – 0.14	7 – 100	0.6 ± 0.2
A	0.14 – 0.40	3 – 7	-1.4 ± 0.2
B	0.01 – 0.08	13 – 100	0.3 ± 0.4
B	0.08 – 0.40	3 – 13	-1.5 ± 0.1
C	0.01 – 0.14	7 – 100	0.5 ± 0.1
C	0.14 – 0.40	3 – 7	-1.2 ± 0.2
D	0.01 – 0.08	13 – 100	0.3 ± 0.2
D	0.08 – 0.40	3 – 13	-1.7 ± 0.1
E	0.01 – 0.14	7 – 100	0.1 ± 0.1
E	0.14 – 0.40	3 – 7	-0.5 ± 0.2
F	0.01 – 0.08	13 – 100	0.2 ± 0.3
F	0.08 – 0.40	3 – 13	- 1.1 ± 0.1

Figure 2.43: Fourier height correlation function linear fit exponents for simulation types A, B, C, D, E, and F at a substrate temperature of 200 °C.

Simulation Type	k (atm^{-1})	x (atm)	Linear Fit Exponent
A	0.01 – 0.03	33 – 100	1.9 ± 1.1
A	0.03 – 0.40	3 – 33	-2.3 ± 0.1
B	0.01 – 0.03	33 – 100	0.6 ± 0.2
B	0.03 – 0.40	3 – 33	-2.3 ± 0.1
C	0.01 – 0.05	20 – 100	1.6 ± 0.7
C	0.05 – 0.40	3 – 20	-2.5 ± 0.1
D	0.01 – 0.05	20 – 100	1.4 ± 0.7
D	0.05 – 0.40	3 – 20	-2.5 ± 0.1
E	0.01 – 0.09	11 – 100	1.0 ± 0.3
E	0.09 – 0.40	3 – 11	-2.3 ± 0.2
F	0.01 – 0.06	17 – 100	0.8 ± 0.4
F	0.06 – 0.40	3 – 17	-2.2 ± 0.1

Figure 2.44: Fourier height correlation function linear fit exponents for simulation types A, B, C, D, E, and F at a substrate temperature of 400 °C.

Simulation Type	k (atm^{-1})	x (atm)	Linear Fit Exponent
A	0.03 – 0.40	3 – 33	-2.3 ± 0.1
B	0.03 – 0.40	3 – 33	-2.1 ± 0.1
C	0.03 – 0.40	3 – 33	-2.4 ± 0.1
D	0.03 – 0.40	3 – 33	-2.2 ± 0.1
E	0.03 – 0.40	3 – 33	-2.4 ± 0.2
F	0.03 – 0.40	3 – 33	-2.4 ± 0.1

Figure 2.45: Fourier height correlation function linear fit exponents for simulation types A, B, C, D, E, and F at a substrate temperature of 600 °C.

2.6 Conclusions

Si growth by molecular beam deposition and sputter deposition at a deposition rate of 0.25 mL sec^{-1} and by pulsed laser deposition at an energy density of approximately 3 J cm^{-2}, deposition coverages of 0.05 mL pls^{-1} and 0.50 mL pls^{-1}, repetition rates of 5.00 pls sec^{-1} and 0.50 pls sec^{-1}, and a time-averaged deposition rate of 0.25 mL sec^{-1} at substrate temperatures of 200 °C to 600 °C was simulated.

The surface images indicated a transition from three-dimensional growth to two-dimensional growth as substrate temperature is increased. This transition occurred between approximately 500 °C and 600 °C for each simulation type.

Root-mean square roughness analysis indicated that energetic smoothening significantly decreases roughness at substrate temperatures below approximately 400 °C and that pulsed roughening slightly increases roughness at substrate temperatures above approximately 400 °C.

In the 200 °C simulations, Fourier height correlation analysis indicated that energetic smoothening affects the feature size distribution, that pulsed roughening affects the feature size distribution in simulations that use the thermal energy distribution, and that energetic smoothening decreases roughness for features smaller than approximately 10 atm. In the 400 °C simulations, for features smaller than approximately 20 atm, Fourier height correlation analysis indicated that energetic smoothening decreases roughness and that pulsed roughening increases roughness. In the 400 °C simulations, for features larger than approximately 20 atm, Fourier height correlation analysis indicated that energetic smoothening affects the feature size distribution, that pulsed roughening affects the feature size distribution in simulations that use the thermal energy distribution, and that pulsed roughening decreases roughness, most likely by suppressing nonstochastic roughening. In the 600 ^{o}C simulations, Fourier height correlation analysis indicated that pulsed roughening increases roughness.

These results indicate that energy distribution and temporal distribution both affect growth morphology, the former more significantly than the latter. To minimize roughening, energetic deposition processes should be used at low substrate temperatures and continuous deposition processes should be used at high substrate temperatures.

References

[1] H. Sankur, W. J. Gunning, J. DeNatale, and J. F. Flintoff, J. Appl. Phys. 65, 2475 (1989).

[2] M. E. Taylor and H. A. Atwater, Appl. Surf. Sci., (1998).

[3] M. V. R. Murty and H. A. Atwater, Phys. Rev. B 45, 1507 (1992).

[4] P. K. Maksym, Semicond. Sci. Technol. 3, 594 (1988).

[5] E. Chason and J. Y. Tsao, Surf. Sci. 234, 361 (1990).

[6] E. Chason and B. W. Dodson, J. Vac. Sci. Technol. A 9, 1545 (1990).

[7] Y. W. Mo, J. Kleiner, M. B. Webb, and M. G. Lagally, Phys. Rev. Lett. 66, 1998 (1991).

[8] R. Boguslawski, Q.-M. Zhang, Z. Zhang, C. Roland, and J. Bernholc, Mat. Sci. Eng. B 30, 167 (1995).

[9] S. Kodiyalam, K. E. Khor, and S. Das Sarma, Phys. Rev. B 53, 9913 (1996).

[10] W. M. Tong and R. S. Williams, Ann. R. Ph. Ch. 45, 401 (1994).

[11] Origin, Microcal Origin.

[12] W. H. Press, S. A. Teukolsky, W. T. Vetterling, and B. P. Flannery, Numerical Recipes in C, Cambridge University Press, New York, 1995.

Chapter 3

Energetic Effects in Silicon Growth on Hydrogen-Terminated Surfaces

3.1 Background

In Si growth on clean (2x1) Si (001) surfaces by molecular beam deposition and sputter deposition, a transition from crystalline growth to amorphous growth occurs at a critical thickness [1-4]. This transition is triggered by formation of crystallographic defects along {111} planes whose intersections provide nucleation sites for the amorphous phase. The critical thickness Z varies with substrate temperature T as

$$Z = Z_0 e^{-Q/kT}$$

where Z_0 is a thickness determined by deposition rate and growth environment, Q is an activation energy, and k is the Boltzmann constant. The critical thickness Z varies slowly with deposition rate R and can be approximately described as

$$Z = Z_0 R^{-1/4}$$

where Z_0 is a thickness determined by substrate temperature and growth environment.

H is always present in some form in the growth environment, either explicitly as in chemical vapor deposition or adventitiously as in molecular beam deposition. Hydrogen termination has been observed to decrease the critical thickness by inhibiting Si surface diffusion [2,5,6]. Crystalline Si growth on monohydride-terminated (2x1) Si (001) surfaces by molecular beam deposition is possible [5]. Although crystalline Si growth on dihydride-terminated (1x1) Si (001) surfaces by sputter deposition is possible, Si growth on dihydride-terminated (1x1) Si (001) surfaces by molecular beam deposition results in purely amorphous growth [7-11]. These results suggest that growth on hydrogen-terminated surfaces is affected by the deposition process.

Molecular beam deposition and sputter deposition exhibit different growth kinetics. Molecular beam deposition is characterized by a narrow energy distribution with a mean energy of a few tenths of an eV. Sputter deposition is characterized by a broad energy distribution with a mean energy of a few eV or a few tens of eV. Pulsed laser deposition, like sputter deposition, is characterized by a broad energy distribution with a mean energy of a few eV or a few tens of eV. Figure 1.2 shows the estimated energy distribution for Si ablated at an energy density of approximately 3 J cm^{-2} as described in Chapter 1.

There are at least four energetic effects that could conceivably enable crystalline growth on dihydride-terminated (1x1) Si (001) surfaces [10,12]. These effects are sputtering of H atoms by incident Si atoms, recoil implantation of H atoms by incident Si atoms, transfer of H atoms from surface Si atoms to incident Si atoms, and subplantation or subsurface deposition of incident Si atoms. The sputtering and implantation effects could enable crystalline growth by transforming the dihydride-terminated (1x1) Si (001) surface to the monohydride-terminated (2x1) Si (001) surface or to the clean (2x1) Si (001) surface at the onset of growth. The transfer and subplantation effects could enable crystalline growth by allowing growth to proceed beneath the dihydride-terminated (1x1) Si (001) surface.

Energy distributions for the sputtering and implantation effects were estimated from molecular dynamics simulation results for H atom yield from dihydride-terminated (1x1) Si (001) surfaces irradiated by Ar^+ ions [12]. Figure 3.1 shows these energy distributions for an initial substrate temperature of 0 K. To transform the dihydride-terminated (1x1) Si (001) surface to the monohydride-terminated (2x1) Si

(001) surface at the onset of growth, each incident Si atom must either sputter or implant one H atom. To transform the dihydride-terminated (1x1) Si (001) surface to the clean (2x1) Si (001) surface at the onset of growth, each incident Si atom must either sputter or implant two H atoms. The estimated combined yield is greater than one H atom and two H atoms per incident Si atom for energies larger than approximately 30 eV and 48 eV, respectively. This indicates that the sputtering and implantation effects are likely to come into play at energies larger than approximately 30 eV if they enable crystalline growth by transforming the dihydride-terminated (1x1) Si (001) surface to the monohydride-terminated (2x1) Si (001) surface and at energies larger than approximately 48 eV if they enable crystalline growth by transforming the dihydride-terminated (1x1) Si (001) surface to the clean (2x1) Si (001) surface.

Energy distributions for the transfer and subplantation effects were estimated from molecular dynamics simulation results for energetic Si growth on dihydride-terminated (1x1) Si (001) surfaces [10]. Figure 3.2 shows these energy distributions for initial substrate temperatures of 0 K and 200 °C. To enable crystalline growth, each incident Si atom must either trigger transfer of an H atom or subplant. The estimated combined probability is approximately unity for energies larger than approximately 8 eV and 3 eV for initial substrate temperatures of 0 K and 200 °C, respectively. This indicates that the transfer and subplantation effects are likely to come into play at energies larger than a few eV.

To evaluate the effect of energy distribution on growth on hydrogen-terminated surfaces, Si was grown on dihydride-terminated (1x1) Si (001) surfaces by pulsed laser deposition [13,14].

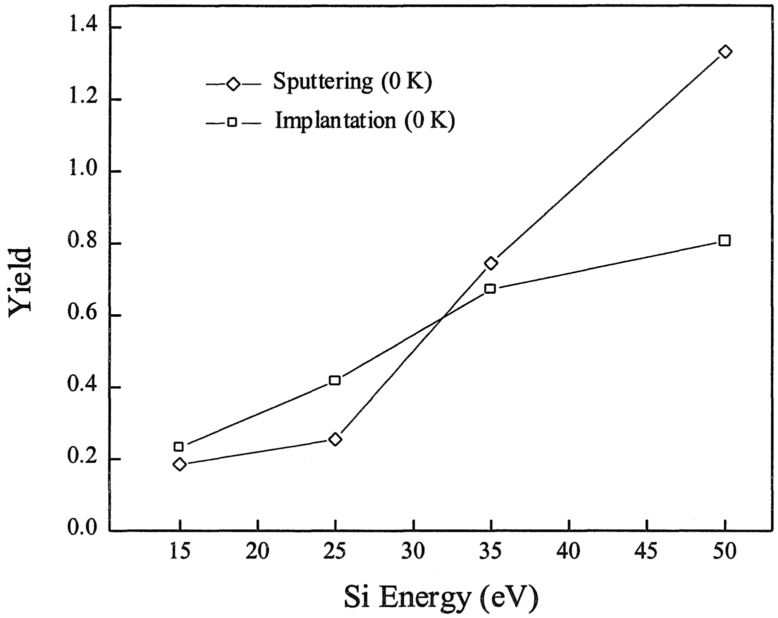

Figure 3.1: Estimated energy distributions for H sputtering and H implantation for an initial substrate temperature of 0 K [12].

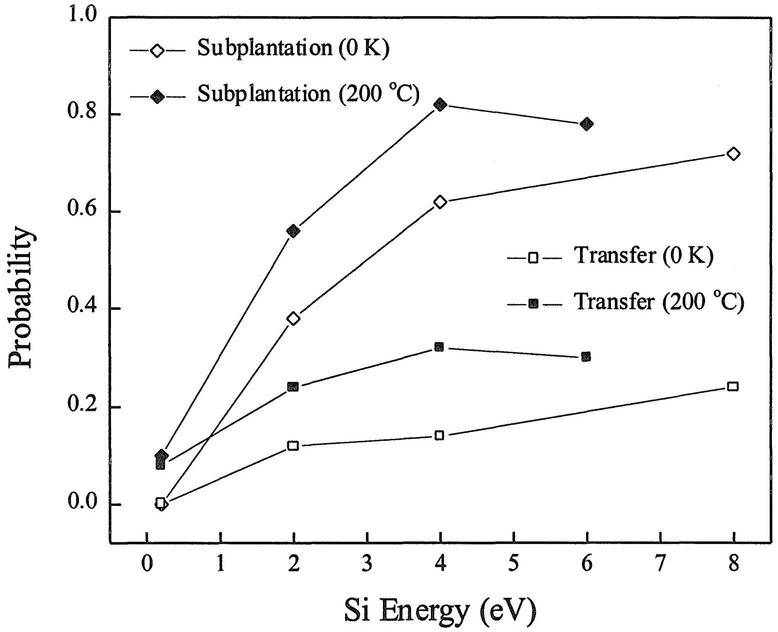

Figure 3.2: Estimated energy distributions for H transfer and Si subplantation for initial substrate temperatures of 0 K and 200 °C [10].

3.2 Experiments

Each Si (001) substrate was cleaned and passivated as described in Chapter 1 to produce a dihydride-terminated (1x1) Si (001) surface.

The pulsed laser deposition system is described in detail in Chapter 1. A polycrystalline Si substrate was used as a target. An energy density of approximately 3 J cm^{-2} was used. Si was grown at a deposition coverage of 0.03 nm pls^{-1}, a repetition rate of 3 pls sec^{-1}, and a time-averaged deposition rate of 0.09 nm sec^{-1}. Growth was continued until a transition from crystalline growth to amorphous growth was observed. Reflection high-energy electron diffraction was used at the onset of growth to confirm surface reconstruction and throughout growth to monitor surface reconstruction and crystallinity. Samples A, B, C, D, E, F, G, and H were grown at substrate temperatures of 40 °C, 75 °C, 100 °C, 170 °C, 205 °C, 275 °C, 305 °C and 345 °C, respectively, and are described in Figure 3.3.

Samples A, B, C, D, E, F, G, and H were characterized by 300 keV cross-sectional high-resolution transmission electron microscopy to determine the critical thickness Z and the morphology at the interface between crystalline growth and amorphous growth. The critical thickness Z is defined as the midpoint of the transition from crystalline growth to amorphous growth.

Sample	Substrate Temperature (^{o}C)
A	40
B	75
C	100
D	170
E	205
F	275
G	305
H	345

Figure 3.3: Samples A, B, C, D, E, F, G, and H.

3.3 Results

Figures 3.4 and 3.5 show representative reflection high-energy electron diffraction patterns for sample E before growth and after growth of 2 nm of Si, respectively. Both patterns indicate a dihydride-terminated (1x1) Si (001) surface. This is consistent with the transfer and subplantation effects, in which the dihydride-terminated (1x1) Si (001) surface remains a dihydride-terminated (1x1) Si (001) surface, and inconsistent with the sputtering and implantation effects, in which the dihydride-terminated (1x1) Si (001) surface is transformed to the monohydride-terminated (2x1) Si (001) surface or to the clean (2x1) Si (001) surface.

Figure 3.6 shows a representative cross-sectional <110> high-resolution transmission electron micrograph of sample H. As in Si growth on clean (2x1) Si (001) surfaces by molecular beam deposition and sputter deposition, the transition from crystalline growth to amorphous growth appears to be triggered by formation of crystallographic defects along {111} planes whose intersections provide nucleation sites for the amorphous phase.

Figure 3.7 shows critical thickness Z for samples A, B, C, D, E, F, G, and H. The error bars represent typical feature heights. Figure 3.8 compares Z for samples A, B, C, D, E, F, G, and H to Z for Si growth on clean (2x1) Si (001) surfaces by molecular beam deposition and sputter deposition at deposition rates of 0.07 nm sec^{-1} and 0.10 nm sec^{-1}, respectively [2,4]. Z for samples A, B, C, D, E, F, G, and H is smaller and increases less rapidly with substrate temperature than Z for molecular beam deposition and sputter deposition on clean (2x1) Si (001) surfaces and does not exhibit a clear Arrhenius dependence on substrate temperature unlike Z for molecular beam deposition and sputter deposition on clean (2x1) Si (001) surfaces. This indicates suppressed Si surface diffusion arising from steric hindrances caused by surface H. This is consistent with the transfer and subplantation effects, in which growth proceeds beneath the dihydride-terminated (1x1) Si (001) surface. This is consistent with the sputtering and implantation effects if these effects enable crystalline growth by transforming the dihydride-terminated (1x1) Si (001) surface to the monohydride-terminated (2x1) Si (001) surface and inconsistent with the sputtering and implantation effects if these effects enable crystalline growth by transforming the dihydride-terminated (1x1) Si (001) surface to the clean (2x1) Si (001) surface.

Figure 1.2 shows the estimated energy distribution for Si ablated at an energy density of approximately 3 J cm^{-2} as described in Chapter 1. Figure 1.2 indicates that approximately 0.40, 0.62 and 1.00 of the incident Si atoms have energies larger than 48 eV, 30 eV, and a few eV, respectively. This is consistent with the transfer and subplantation effects, which are likely to come into play at energies larger than a few eV, and inconsistent with the sputtering and implantation effects, which are likely to come into play at energies larger than approximately 30 eV if they enable crystalline growth by transforming the dihydride-terminated (1x1) Si (001) surface to the monohydride-terminated (2x1) Si (001) surface and at energies larger than approximately 48 eV if they enable crystalline growth by transforming the dihydride-terminated (1x1) Si (001) surface to the clean (2x1) Si (001) surface.

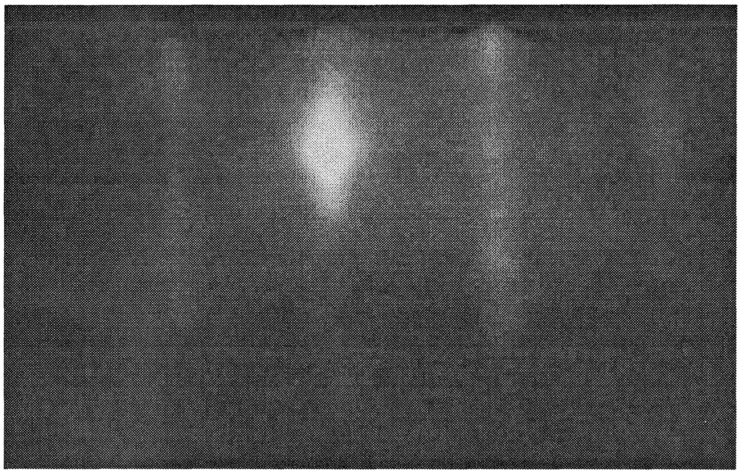

Figure 3.4: Reflection high-energy electron diffraction pattern for sample E before growth.

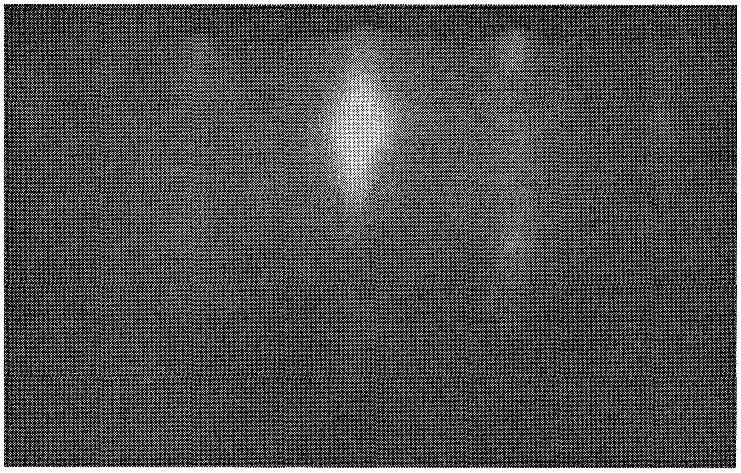

Figure 3.5: Reflection high-energy electron diffraction pattern for sample E after growth of 2 nm of Si.

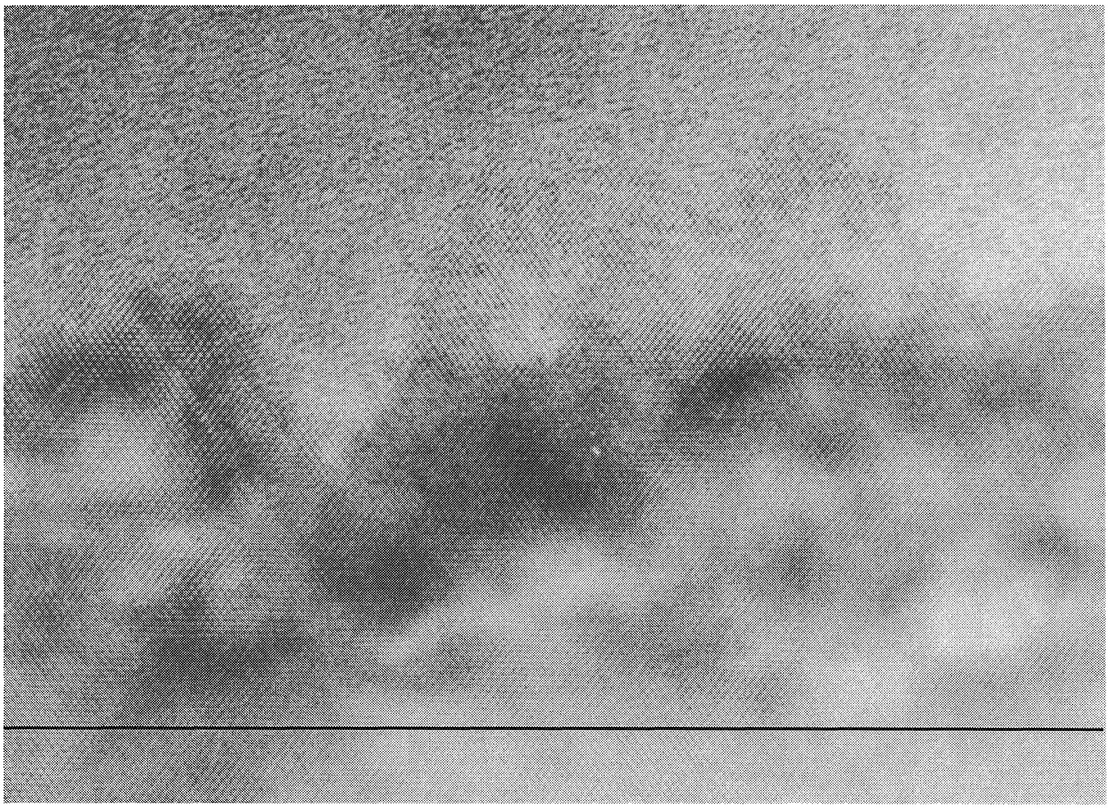

Figure 3.6: Cross-sectional <110> high-resolution transmission electron micrograph of sample H. The image area is approximately 43 nm by 31 nm. The line demarcates the boundary between the substrate and the film.

Sample	Substrate Temperature (°C)	Critical Thickness (nm)
A	40	1.5 ± 0.5
B	75	3.5 ± 1.0
C	100	5.5 ± 1.0
D	170	10.0 ± 1.5
E	205	12.0 ± 3.0
F	275	8.5 ± 4.0
G	305	11.0 ± 2.0
H	345	17.5 ± 6.0

Figure 3.7: Critical thicknesses for samples A, B, C, D, E, F, G, and H. The error bars represent typical feature heights.

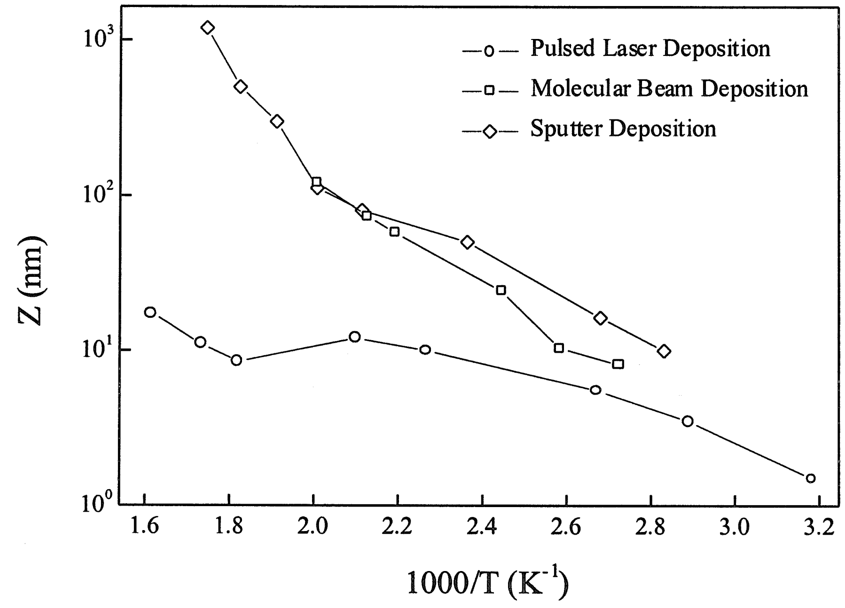

Figure 3.8: Critical thicknesses for samples A, B, C, D, E, F, G, and H and for Si growth on clean (2x1) Si (001) surfaces by molecular beam deposition and sputter deposition at deposition rates of 0.07 nm sec^{-1} and 0.10 nm sec^{-1}, respectively [2,4].

3.4 Conclusions

Si was grown on dihydride-terminated (1x1) Si (001) surfaces by pulsed laser deposition at an energy density of approximately 3 J cm^{-2}, a deposition coverage of 0.03 nm pls^{-1}, a repetition rate of 3 pls sec^{-1}, a time-averaged deposition rate of 0.09 nm sec^{-1}, and substrate temperatures of 40 °C to 345 °C.

Reflection high-energy electron diffraction and cross-sectional high-resolution transmission electron microscopy indicated that crystalline growth on dihydride-terminated (1x1) Si (001) surfaces by pulsed laser deposition is possible, like sputter deposition and unlike molecular beam deposition.

Cross-sectional high-resolution transmission electron microscopy indicated that the transition from crystalline growth to amorphous growth is triggered by formation of crystallographic defects along {111} planes whose intersections provide nucleation sites for the amorphous phase, as in molecular beam deposition and sputter deposition on clean (2x1) Si (001) surfaces.

Reflection high-energy electron diffraction indicated that dihydride-terminated (1x1) Si (001) surfaces remain dihydride-terminated (1x1) Si (001) surfaces throughout growth. Cross-sectional high-resolution transmission electron microscopy indicated that critical thickness is smaller and increases less rapidly with substrate temperature than critical thickness for molecular beam deposition and sputter deposition on clean (2x1) Si (001) surfaces, indicating suppressed Si surface diffusion arising from steric hindrances caused by surface H. The estimated energy distribution of incident Si atoms indicated that all of the incident Si atoms have energies of a few eV and that only a fraction of the incident Si atoms have energies of a few tens of eV.

These results indicate that crystalline growth on dihydride-terminated (1x1) Si (001) surfaces is enabled by transfer of H atoms from surface Si atoms to incident Si atoms and subplantation of incident Si atoms.

References

[1] M. V. R. Murty and H. A. Atwater, Phys. Rev. B 49, 8483 (1994).

[2] D. J. Eaglesham, J. Appl. Phys. 77, 3597 (1995).

[3] D. L. Smith, C.-C. Chen, G. B. Anderson, and S. B. Hagstrom, Appl. Phys. Lett. 62, 570 (1993).

[4] N.-E. Lee, G. A. Tomasch, and J. E. Greene, Appl. Phys. Lett. 65, 3236 (1994).

[5] M. Copel and R. M. Tromp, Phys. Rev. Lett. 72, 1236 (1994).

[6] J. E. Vasek, Z. Zhang, C. T. Salling, and M. G. Lagally, Phys. Rev. B 51, 17207 (1995).

[7] S. S. Iyer, M. Arienzo, and E. deFresart, Appl. Phys. Lett. 57, 893 (1990).

[8] F. Hirose, M. Suemitsu, and N. Miyamoto, Jap. J. Appl. Phys. 29, L1881 (1990).

[9] D. J. Eaglesham, G. S. Higashi, and M. Cerullo, Appl. Phys. Lett. 59, 685 (1991).

[10] M. V. R. Murty and H. A. Atwater, Surf. Sci. 374, 283 (1997).

[11] C.-C. Chen, D. L. Smith, G. B. Anderson, and S. B. Hagstrom, Mat. Res. Soc. Symp. Proc. 259, 443 (1992).

[12] M. V. R. Murty and H. A. Atwater, Nucl. Instrum. Methods Phys. Res. B 102, 293 (1995).

[13] M. E. Taylor, H. A. Atwater, and M. V. R. Murty, Mat. Res. Soc. Symp. Proc. 441, 579 (1997).

[14] M. E. Taylor, H. A. Atwater, and M. V. R. Murty, Thin Sol. Fi., (1998).

Chapter 4

Energetic Effects in Tin Germanium Alloy Growth

4.1 Background

Diamond cubic Sn_xGe_{1-x} alloys have been the focus of extensive research [1-27]. Band structure calculations predict that Sn_xGe_{1-x} is a direct bandgap semiconductor with a bandgap that ranges from 0.55 eV to 0 eV as the composition x is varied from 0.2 to 0.6 [16-22]. Infrared spectroscopy measurements of the absorption coefficient indicate that the direct bandgap of Sn_xGe_{1-x} ranges from 0.80 eV to 0.25 eV as the composition x is varied from 0 to 0.15 [23]. Sn_xGe_{1-x} has potential for monolithic integration on Si (001) substrates. These properties make Sn_xGe_{1-x} of interest for future Si-based infrared optoelectronics and high performance heterojunction applications.

Sn_xGe_{1-x} is a thermodynamically metastable material. The equilibrium phase diagram is shown in Figure 4.1. Sn and Ge form a simple eutectic with mutual solid solubilities of less than 0.01 [24-27]. This, in combination with the differences in surface free energy and atomic radii, leads to Sn surface segregation during growth [4-13]. In addition, at thermodynamic equilibrium bulk Sn undergoes a transition from the diamond cubic phase, referred to as the α-Sn phase, to the body centered tetragonal phase, referred to as the β-Sn phase, as temperature is increased above 13.2 °C [28]. The transition temperature has been shown to be as high as 130 °C for thin Sn films [29-32]. Thin Sn_xGe_{1-x} films are likely to have a higher transition temperature due to the presence of Ge [33].

To evaluate the effect of energy distribution on alloy growth, Sn_xGe_{1-x} was grown by solid phase epitaxy, a thermal process, and by pulsed laser deposition, an energetic process [34,35].

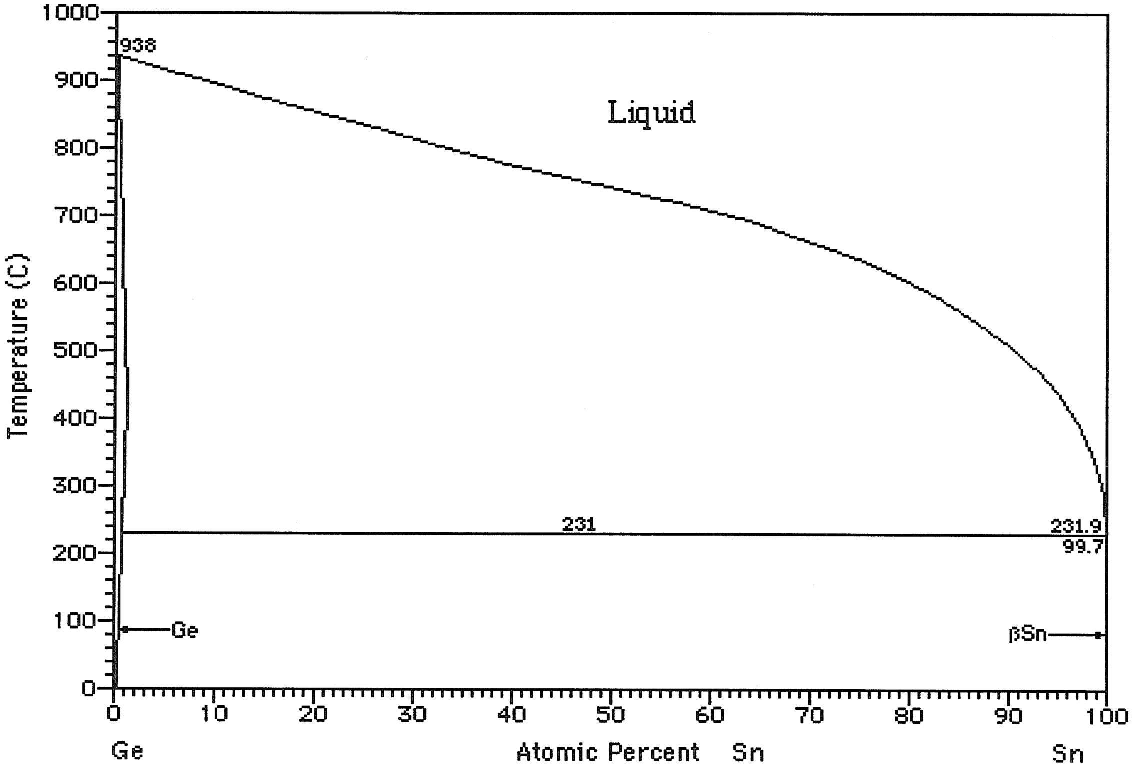

Figure 4.1: Equilibrium Sn Ge phase diagram [27].

Reprinted with permission from E S Microware.

4.2 Solid Phase Epitaxy

In solid phase epitaxy, an amorphous layer adjacent to or within a crystalline substrate is converted to a crystalline layer by rearrangement of atoms at the interface between the crystalline and amorphous phases [36]. This transformation can be induced either by annealing or by ion bombardment. In elemental materials, in the absence of random nucleation and growth, solid phase epitaxy occurs in a planar fashion. The velocity V of the interface between the crystalline and amorphous phases varies with temperature T as

$$V = V_o e^{-Q/kT}$$

where V_o is a velocity determined by the material and its microstructure, Q is an activation energy, and k is the Boltzmann constant.

Solid phase epitaxy of Si, Ge, and Si_xGe_{1-x} has been the focus of extensive research [36-38]. In Si and Ge, solid phase epitaxy occurs in a planar fashion with interface velocities well described by the temperature dependence shown above. Pre-exponential velocities V_o of $5x10^8$ cm sec^{-1} and $1x10^9$ cm sec^{-1} and activation energies Q of 2.70 eV ± 0.02 eV and 2.26 eV ± 0.02 eV have been reported for Si and Ge, respectively [36]. Interface velocities reported for Si_xGe_{1-x} vary significantly. However, similar microstructural behavior has been reported. In $Si_{0.70}Ge_{0.30}$, the interface was reported to facet into {111} planes [37]. In $Si_{0.88}Ge_{0.12}$, interface velocity was reported to decrease in the vicinity of crystallographic defects, leading to loss of interface planarity [38].

To evaluate the effect of energy distribution on alloy growth, Sn_xGe_{1-x} was grown by solid phase epitaxy, a thermal process.

4.2.1 Experiments

Each Si (001) substrate was cleaned and passivated as described in Chapter 1 and annealed at 550 °C to produce a clean (2x1) Si (001) surface.

The molecular beam deposition chamber has a base pressure of $2\text{x}10^{-10}$ torr. Crystalline Ge and amorphous Ge, referred to as c-Ge and a-Ge, were grown at substrate temperatures of 400 °C and 70 °C, respectively, prior to Sn_xGe_{1-x} growth to minimize lattice misfit. Amorphous Sn_xGe_{1-x}, referred to as a-Sn_xGe_{1-x}, was grown at a substrate temperature of 70 °C. Reflection high-energy electron diffraction was used at the onset of growth to confirm surface reconstruction and throughout growth to monitor crystallinity. Samples of types A, B, C, and D have compositions x of 0.02, 0.10, 0.19, and 0.26, respectively, and are described in Figure 4.2.

Samples of types A, B, C, and D were isothermally annealed to initiate solid phase epitaxy to produce crystalline Sn_xGe_{1-x}, referred to as c-Sn_xGe_{1-x}.

Samples of types A, B, C, and D were annealed at 360 °C, 300 °C, 300 °C, and 300 °C, respectively. These samples were characterized by 300 keV transmission electron microscopy. Micrographs were used to determine c-Sn_xGe_{1-x} microstructure. Semiquant was used to analyze energy dispersive x-ray yields to determine c-Sn_xGe_{1-x} composition x [39]. Diffraction patterns were used to determine c-Sn_xGe_{1-x} microstructure and composition x. Misfit strain relaxation was assumed. The c-Sn_xGe_{1-x} composition x is approximately equal to

$$x = (a_x-a_{Ge})/(a_{Sn}-a_{Ge})$$

where a_{Ge} is the Ge lattice parameter, a_{Sn} is the α-Sn lattice parameter, and a_x is the c-Sn_xGe_{1-x} lattice parameter and is equal to

$$a_x = a_{Si} r_{Si} / r_x$$

where a_{Si} is the Si lattice parameter, r_{Si} is the radial position of a Si diffraction, and r_x is the radial position of a corresponding c-Sn_xGe_{1-x} diffraction [40,41].

Samples of types A and D were annealed at 360 °C and 300 °C, respectively. These samples were characterized by Cu $K\alpha_1$ x-ray diffraction at a wavelength of 0.1541 nm. Diffraction patterns were used to determine c-Sn_xGe_{1-x} microstructure and composition x. Misfit strain relaxation was assumed. The c-Sn_xGe_{1-x} composition x is approximately equal to

$$x = (a_x - a_{Ge})/(a_{Sn} - a_{Ge})$$

where a_{Ge} is the Ge lattice parameter, a_{Sn} is the α-Sn lattice parameter, and a_x is the c-Sn_xGe_{1-x} lattice parameter and is equal to

$$a_x = a_{Si}(1 - (\theta_{Si} - \theta_x) \cot \theta_B)$$

where a_{Si} is the Si lattice parameter, θ_{Si} is the angular position of the Si (400) peak, θ_x is the angular position of the c-Sn_xGe_{1-x} (400) peak, and θ_B is the Bragg angle for Si (400) diffraction, equal to

$$\theta_B = 2\lambda / a_{Si}$$

where λ is the wavelength [40,41].

Type A samples were annealed at 300 °C, 325 °C, 345 °C, and 360 °C. A type C sample was annealed at 325 °C. These samples were characterized by 2 MeV He^{++} Rutherford backscattering spectrometry. Rump was used to analyze random orientation and channeling orientation Sn and Ge backscattering profiles to determine c-Sn_xGe_{1-x} microstructure, thickness, and composition x [42]. Type A samples were repeatedly annealed at 300 °C and 325 °C. Changes in c-Sn_xGe_{1-x} thickness were used to determine the interface velocity V. Origin was used to Arrheniusly fit the interface velocity V to determine a pre-exponential velocity V_o and an activation energy Q [43].

Type A samples were annealed at 350 °C, 375 °C, 400 °C, and 425 °C. Type B samples were annealed at 390 °C, 455 °C, and 505 °C. Type C samples were annealed at 300 °C, 350 °C, 375 °C, and 400 °C. Type D samples were annealed at 325 °C, 350 °C, and 375 °C. These samples were characterized by time-resolved reflectivity at wavelengths of 825 nm, 825 nm, 670 nm, and 670 nm, respectively. This form of reflection interferometry is based on interference between light reflected from the surface and light reflected from the interface [36]. A low-power laser was focused on the sample at near-normal incidence and the reflected intensity was measured with a photodiode. As the sample annealed, the interface approached the surface, causing interference oscillations in the reflected intensity. The interface velocity V is equal to

$$V = \lambda/2nP$$

where λ is the laser wavelength, n is the refractive index, and P is the oscillation period [36]. Origin was used to Arrheniusly fit the interface velocity V to determine a pre-exponential velocity V_o and an activation energy Q [43]. Non-oscillatory changes in reflected intensity were used to determine changes in microstructure. Values for n of 4.64 and 5.21, reported values for c-Ge at 825 nm and 670 nm, respectively, were used [44].

Sample Type	a-Sn_xGe_{1-x} Composition x	a-Sn_xGe_{1-x} Thickness (nm)	a-Ge Thickness (nm)	c-Ge Thickness (nm)
A	0.02	170	10	60
B	0.10	170	70	20
C	0.19	170	0	100
D	0.26	190	70	10

Figure 4.2: Samples A, B, C, and D.

4.2.2 Results

Figure 4.3 shows a cross-sectional <110> transmission electron micrograph of a type A sample annealed at 360 °C for 40 min. The micrograph shows c-Ge, c-Sn_xGe_{1-x}, and a-$Sn_{0.02}Ge_{0.98}$. It does not show segregated Sn, consistent with c-Sn_xGe_{1-x} where composition x is 0.02. The interface between c-Ge and c-Sn_xGe_{1-x} is characterized by crystallographic defects, indicating misfit strain relaxation. The interface between c-Sn_xGe_{1-x} and a-$Sn_{0.02}Ge_{0.98}$ is characterized by pits resembling {111} facets located at the exit points of threading dislocations, indicating that interface velocity is lower near crystallographic defects.

Figures 4.4 through 4.6 show plan-view <001> transmission electron micrographs of samples of types B, C, and D, respectively, annealed at 300 °C for 60 min. The micrographs show light regions interrupted by dark regions with diameters of approximately 60 nm, 400 nm, and 600 nm, respectively. Energy dispersive x-ray spectroscopy indicated that the light regions correspond to Sn_xGe_{1-x} where composition x is a few percent and that the dark regions correspond to segregated Sn.

Figure 4.7 shows a cross-sectional <110> transmission electron diffraction pattern for a type A sample annealed at 360 °C for 40 min. Figure 4.8 shows a plan-view <001> transmission electron diffraction pattern for a type C sample annealed at 300 °C for 60 min. Each pattern shows two sets of diffractions. Both sets of diffractions are consistent with diamond cubic material. The set of diffractions with larger radii most likely corresponds to Si. The set of diffractions with smaller radii is most likely a superposition of diffractions corresponding to c-Ge and c-Sn_xGe_{1-x}. In Figure 4.7, the relative radial positions of the two sets of diffractions indicate a composition x of

0.012 ± 0.006. This is consistent with a superposition of diffractions corresponding to c-Ge and c-Sn_xGe_{1-x} where composition x is larger than 0.01. In Figure 4.8, the relative radial positions of the two sets of diffractions indicate a composition x of 0.05 ± 0.06. This is consistent with a superposition of diffractions corresponding to c-Ge and c-Sn_xGe_{1-x} where composition x is larger than 0.05.

Figures 4.9 and 4.10 show plan-view <001> transmission electron diffraction patterns for samples of types B and D, respectively, annealed at 300 °C for 60 min. The patterns are consistent with diamond cubic material and most likely correspond to c-Sn_xGe_{1-x}. A number of extra diffractions appear in Figure 4.10. These diffractions most likely correspond to segregated β-Sn.

Figures 4.11 and 4.12 show x-ray diffraction patterns for a type A sample annealed at 360 °C for 70 min and a type D sample annealed at 300 °C for 60 min, respectively. The peaks on the right correspond to Si. The peaks on the left are most likely superpositions of peaks corresponding to c-Ge and c-Sn_xGe_{1-x}. Peak broadness arises from superposition, small layer thickness, and misfit strain relaxation. In Figure 4.11, the relative Gaussian mean positions of the two peaks indicate a composition x of –0.0070 ± 0.0001. This is inconsistent with a superposition of peaks corresponding to c-Ge and c-Sn_xGe_{1-x} but should not be considered as definitive because of uncertainty introduced by peak broadness. In Figure 4.12, if the peak in Figure 4.11 is assumed to correspond to c-Sn_xGe_{1-x} where composition x is 0.02, the relative Gaussian mean positions of the peaks on the left in Figures 4.11 and 4.12 indicate a composition x of 0.036 ± 0.001. This is consistent with a superposition of peaks corresponding to c-Ge and c-Sn_xGe_{1-x} where composition x is larger than 0.04.

Figure 4.13 shows Rutherford backscattering spectra for a type A sample annealed at 300 °C for 14 hrs. The channeling spectrum, collected after the anneal, shows lower yields in the low-energy regions of the Sn and Ge backscattering profiles than the random spectra, indicating c-Ge and c-Sn_xGe_{1-x}. The random spectra, collected before and after the anneal, show identical Sn and Ge backscattering profiles, indicating that Sn segregation did not occur, consistent with c-Sn_xGe_{1-x} where composition x is 0.02. The ratios of the channeling yields to the random yields in the low-energy regions of the Sn and Ge backscattering profiles are approximately 0.5, indicating a high density of crystallographic defects. Spectra for type A samples annealed at 325 °C, 345 °C, and 360 °C do not vary significantly from the spectra shown in Figure 4.13. The interface velocities V determined from spectra for type A samples annealed at 300 °C and 325 °C are described in Figures 4.15 and 4.16, respectively. An Arrhenius fit indicated a pre-exponential velocity V_o and an activation energy Q of 1×10^{11} cm sec^{-1} and 2.38 eV, respectively.

Figure 4.14 shows Rutherford backscattering spectra for a type C sample annealed at 325 °C for 40 min. The channeling spectrum, collected after the anneal, shows lower yields in the Sn and Ge backscattering profiles than the random spectra, indicating c-Ge and c-Sn_xGe_{1-x}. The random spectrum collected after the anneal shows lower yields in the low-energy region of the Sn backscattering profile and higher yields in the low-energy region of the Ge backscattering profile than the random spectrum collected before the anneal, indicating that Sn segregation occurred. The ratios of the channeling yields to the random yields in the Ge and Sn backscattering profiles are approximately 0.5 and 0.9, respectively, indicating a high density of crystallographic defects.

Figure 4.17 shows time-resolved reflectivity spectra for type A samples annealed at 350 °C, 375 °C, 400 °C, and 425 °C. The interface velocities V determined from the spectra are described in Figure 4.21. An Arrhenius fit indicated a pre-exponential velocity V_o of $8x10^9$ cm sec^{-1} to $3x10^{10}$ cm sec^{-1} and an activation energy Q of 2.30 eV ± 0.04 eV.

Figure 4.18 shows time-resolved reflectivity spectra for type B samples annealed at 390 °C, 455 °C, and 505 °C. The spectra increase after the final minimum that corresponds to completion of solid phase epitaxy. Since Sn has a higher reflectivity than Ge, this most likely indicates Sn segregation. This suggests a time delay between completion of solid phase epitaxy and onset of Sn segregation. Such a delay was observed for polycrystalline $Sn_{0.25}Ge_{0.75}$ grown by solid phase crystallization on amorphous substrates [3]. This suggests that by a careful choice of anneal time it may be possible to produce c-$Sn_{0.10}Ge_{0.90}$ by solid phase epitaxy. The interface velocities V determined from the spectra are described in Figure 4.22. An Arrhenius fit indicated a pre-exponential velocity V_o of $6x10^{-5}$ cm sec^{-1} to 10 cm sec^{-1} and an activation energy Q of 0.8 eV ± 0.4 eV.

Figures 4.19 and 4.20 show time-resolved reflectivity spectra for type C samples annealed at 300 °C, 350 °C, 375 °C and 400 °C and type D samples annealed at 325 °C, 350 °C, and 375 °C, respectively. The spectra decrease slightly rather than decreasing to the minimum that corresponds to completion of solid phase epitaxy. Since Sn has a higher reflectivity than Ge, this most likely indicates simultaneous solid phase epitaxy and Sn segregation. The interface velocities V determined from the spectra for samples of types C and D are described in Figures 4.23 and 4.24, respectively. Arrhenius fits indicated pre-exponential velocities V_o of 7 cm sec^{-1} to 30 cm sec^{-1} and of $2x10^{-4}$ cm sec^{-1} to 0.3 cm sec^{-1} and activation energies Q of 1.05 eV ± 0.04 eV and of 0.5 eV ± 0.2 eV for samples of types C and D, respectively.

Figure 4.25 shows the interface velocities V determined from Rutherford backscattering spectra and time-resolved reflectivity spectra for samples of types A, B, C, and D and reported for Ge [36]. Figure 4.26 lists the pre-exponential velocities V_o and activation energies Q determined from the interface velocities V for samples of types A, B, C, and D and reported for Ge [36]. The activation energy Q of 2.30 eV ± 0.04 eV determined from time-resolved reflectivity spectra for type A samples does not differ significantly from the activation energy Q of 2.26 eV ± 0.02 eV reported for Ge.

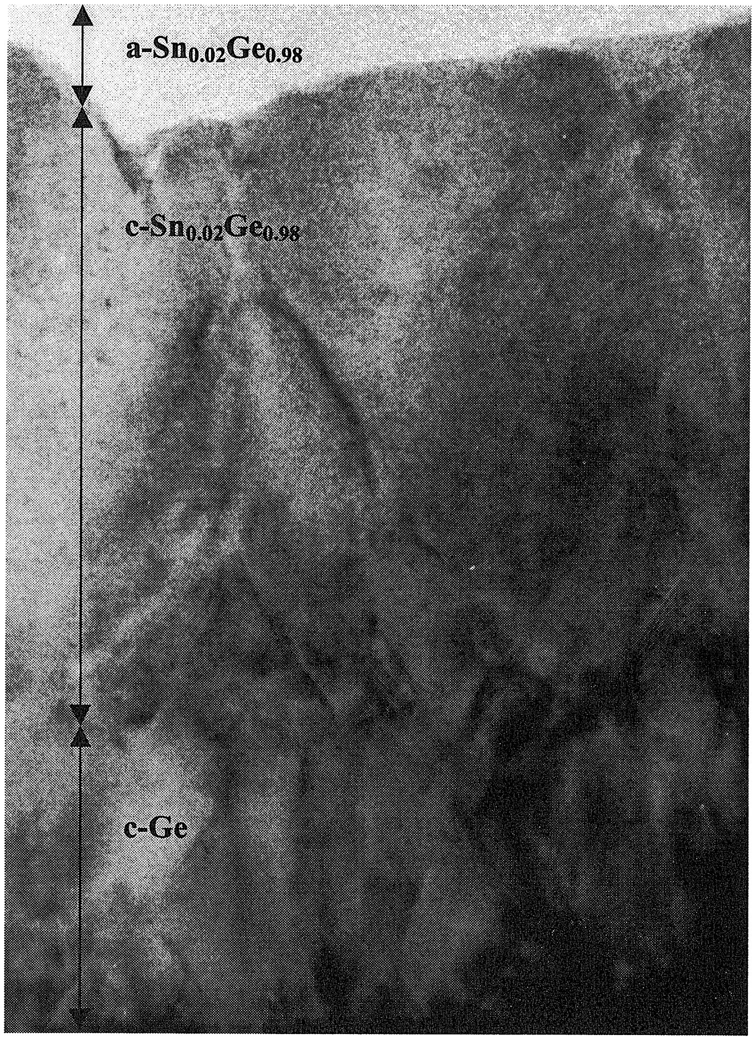

Figure 4.3: Cross-sectional <110> transmission electron micrograph of a type A sample annealed at 360 °C for 40 min. The image area is approximately 230 nm by 165 nm.

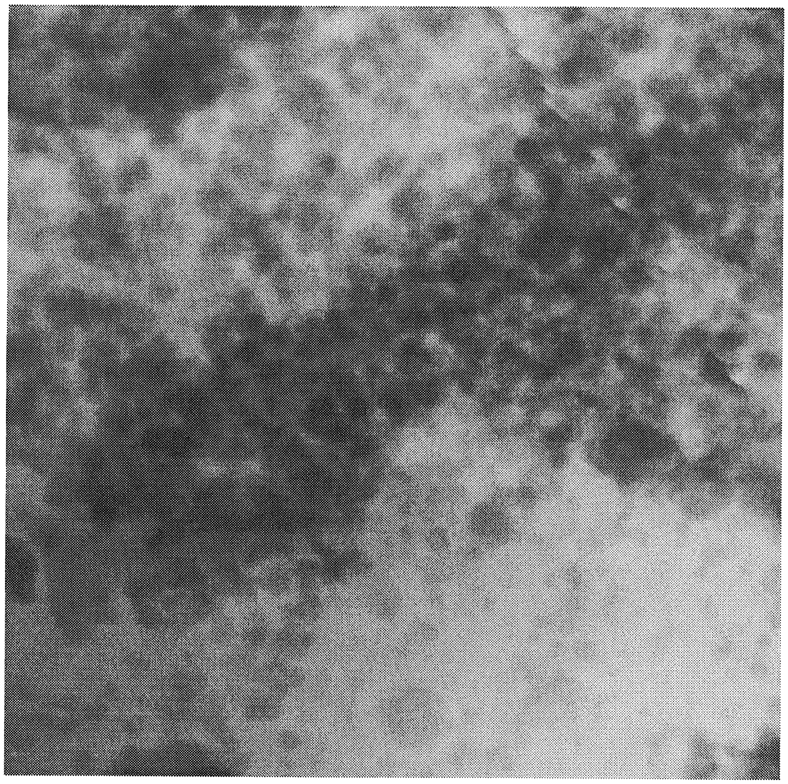

Figure 4.4: Plan-view <001> transmission electron micrograph of a type B sample annealed at 300 °C for 60 min. The image area is approximately 1 μm by 1 μm.

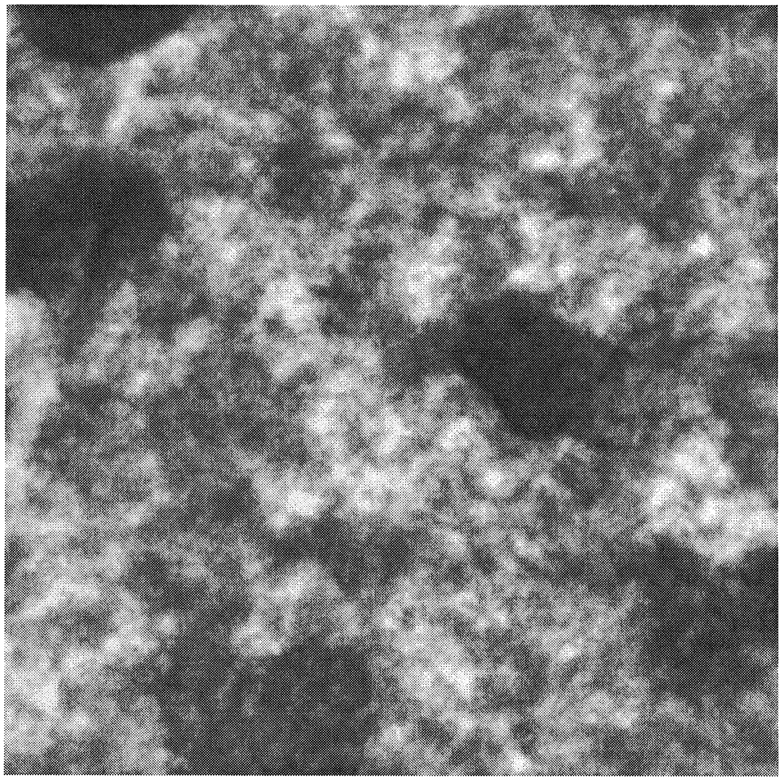

Figure 4.5: Plan-view <001> transmission electron micrograph of a type C sample annealed at 300 °C for 60 min. The image area is approximately 2 μm by 2 μm.

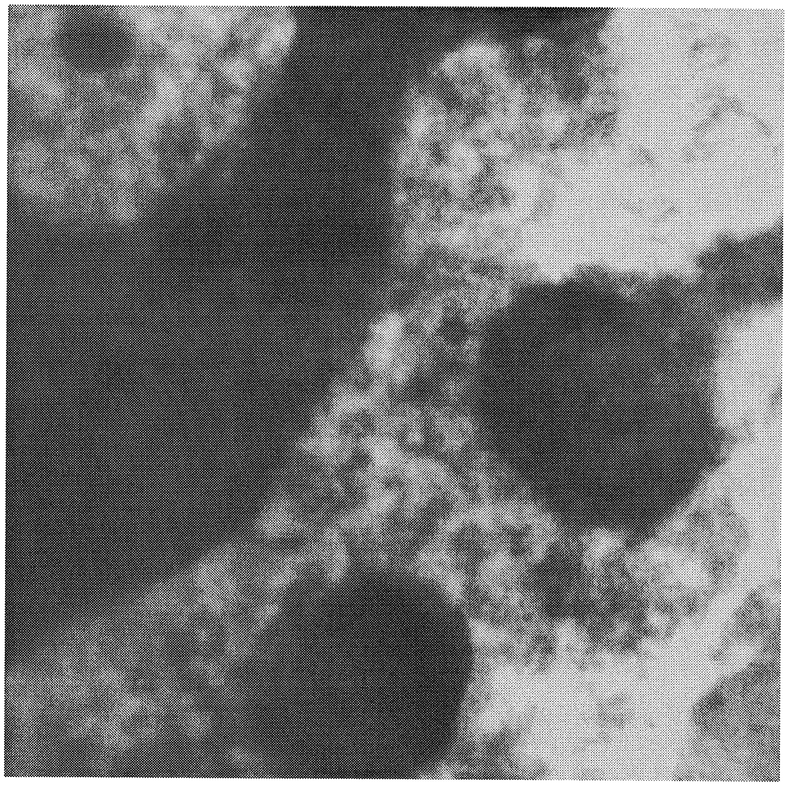

Figure 4.6: Plan-view <001> transmission electron micrograph of a type D sample annealed at 300 °C for 60 min. The image area is approximately 2 μm by 2 μm.

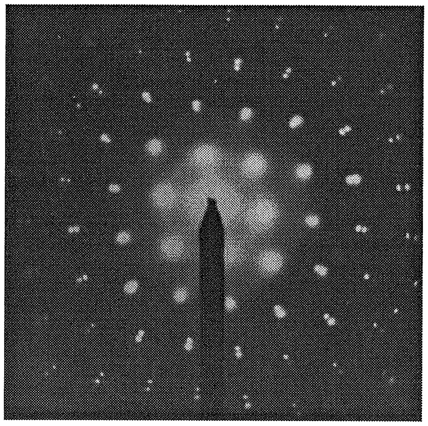

Figure 4.7: Cross-sectional <110> transmission electron diffraction pattern for a type A sample annealed at 360 °C for 40 min.

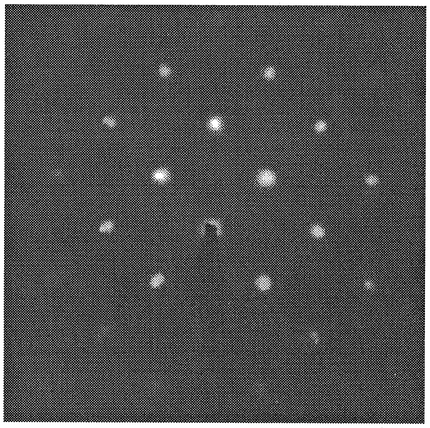

Figure 4.8: Plan-view <001> transmission electron diffraction pattern for a type C sample annealed at 300 °C for 60 min.

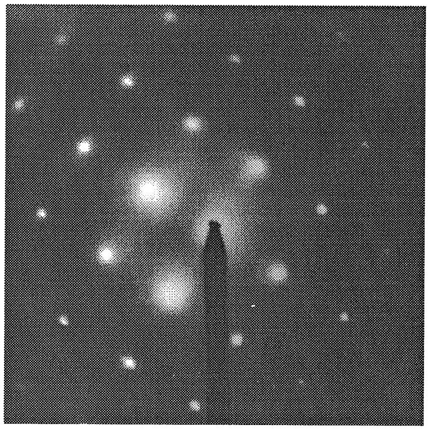

Figure 4.9: Plan-view <001> transmission electron diffraction pattern for a type B sample annealed at 300 °C for 60 min.

Figure 4.10: Plan-view <001> transmission electron diffraction pattern for a type D sample annealed at 300 °C for 60 min.

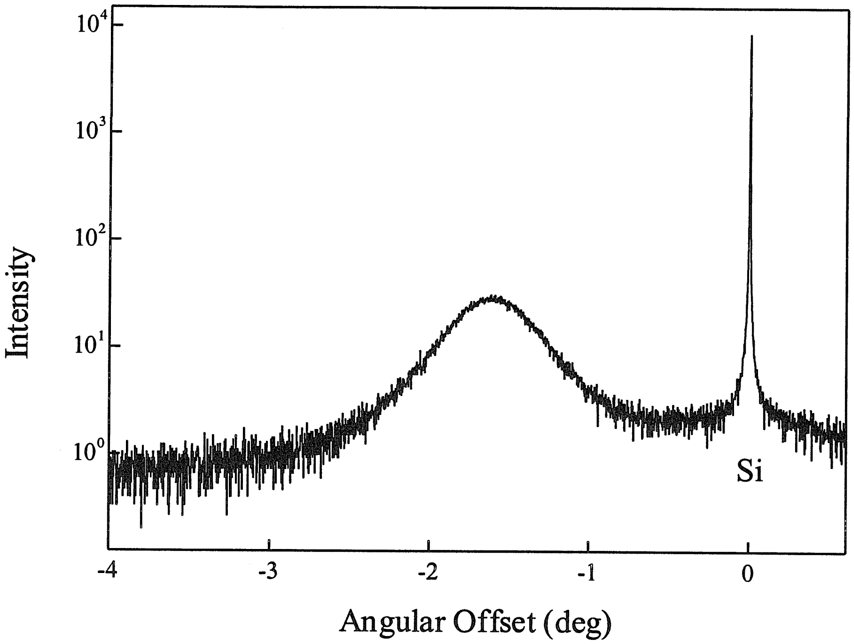

Figure 4.11: X-ray diffraction pattern for a type A sample annealed at 360 °C for 70 min.

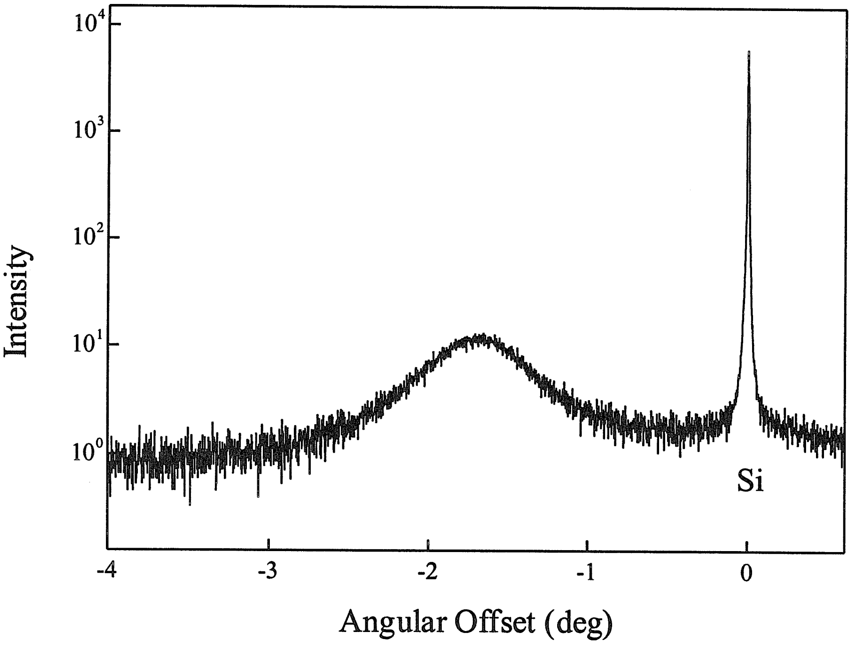

Figure 4.12: X-ray diffraction pattern for a type D sample annealed at 300 °C for 60 min.

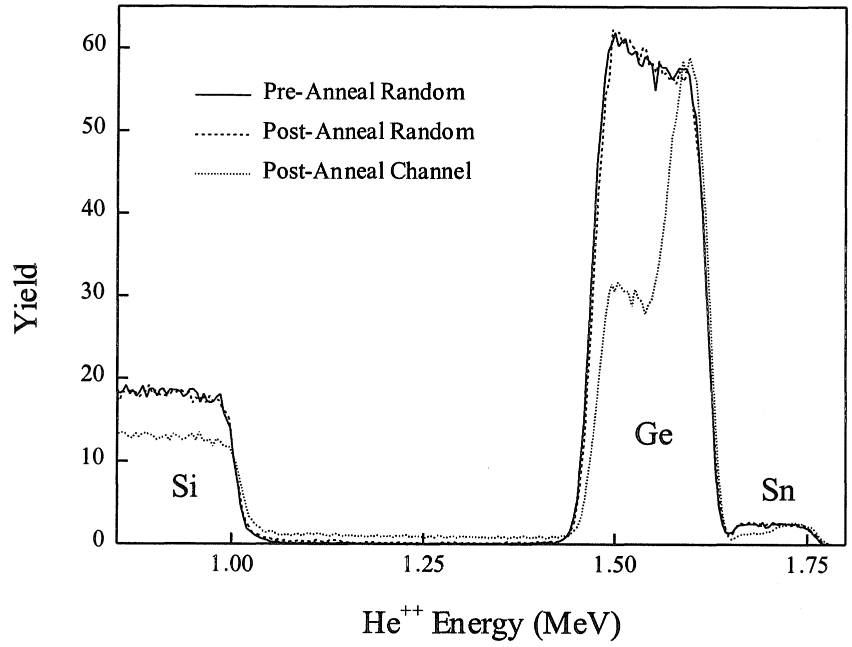

Figure 4.13: Rutherford backscattering spectra for a type A sample annealed at 300 °C for 14 hr.

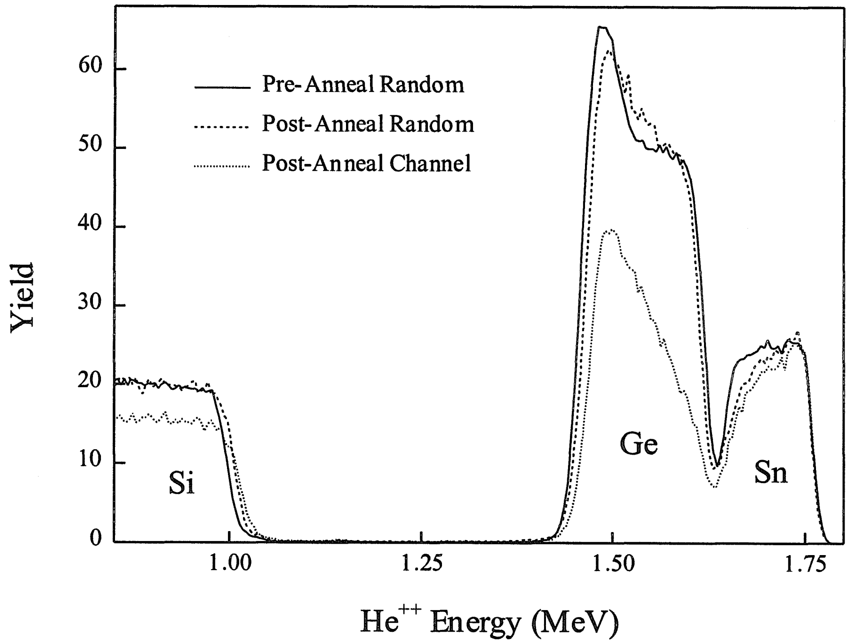

Figure 4.14: Rutherford backscattering spectra for a type C sample annealed at 325 °C for 40 min.

Anneal Time (sec)	c-$Sn_{0.02}Ge_{0.98}$ Thickness Change (nm)	Interface Velocity (nm sec^{-1})
25778	45	0.00175
5580	7	0.00125
7500	10	0.00133

Figure 4.15: Solid phase epitaxy velocities determined from Rutherford backscattering spectra for a type A sample annealed at 300 °C. These velocities were weighted by c-$Sn_{0.02}Ge_{0.98}$ thickness change and averaged to give a velocity of 0.0016 nm sec^{-1} ± 0.0002 nm sec^{-1}.

Anneal Time (sec)	c-$Sn_{0.02}Ge_{0.98}$ Thickness Change (nm)	Interface Velocity (nm sec^{-1})
2500	33	0.0132
2538	28	0.0110

Figure 4.16: Solid phase epitaxy velocities determined from Rutherford backscattering spectra for a type A sample annealed at 325 °C. These velocities were weighted by c-$Sn_{0.02}Ge_{0.98}$ thickness change and averaged to give a velocity of 0.012 nm sec^{-1} ± 0.001 nm sec^{-1}.

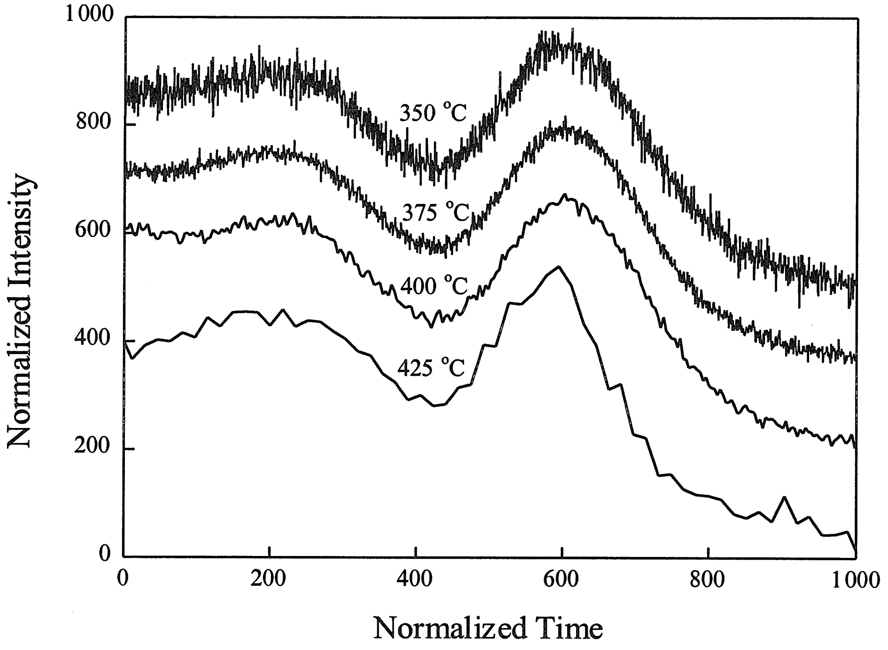

Figure 4.17: Time-resolved reflectivity spectra for type A samples annealed at 350 °C, 375 °C, 400 °C, and 425 °C.

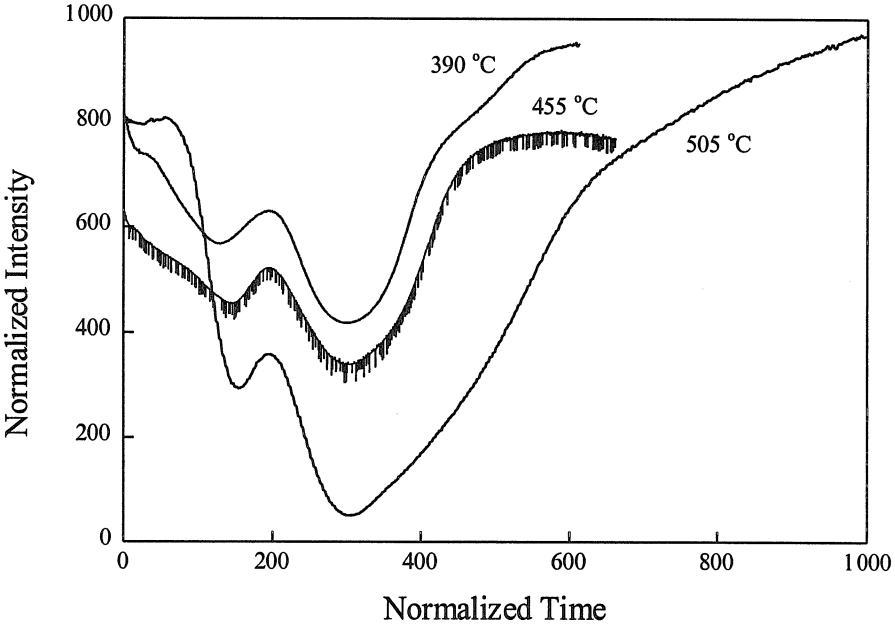

Figure 4.18: Time-resolved reflectivity spectra for type B samples annealed at 390 °C, 455 °C, and 505 °C.

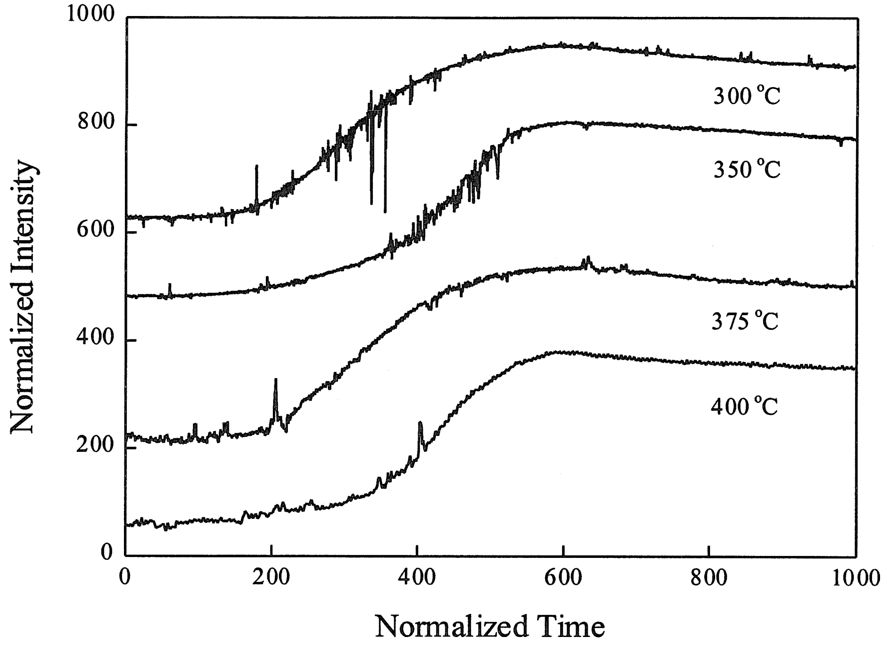

Figure 4.19: Time-resolved reflectivity spectra for type C samples annealed at 300 °C, 350 °C, 375 °C, and 400 °C.

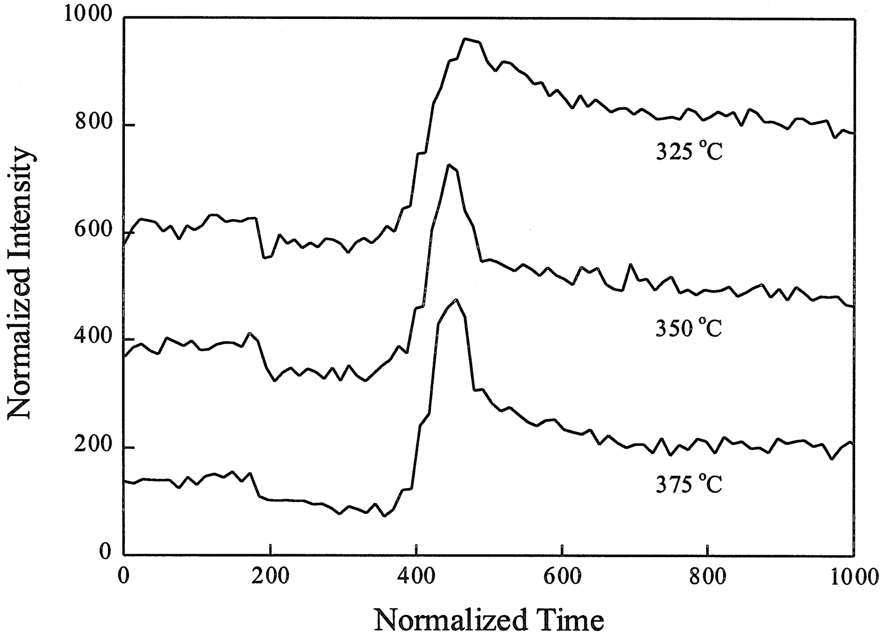

Figure 4.20: Time-resolved reflectivity spectra for type D samples annealed at 325 °C, 350 °C, and 375 °C.

Anneal Temperature (^oC)	Oscillation Period (sec)	Interface Velocity (nm sec^{-1})
350	2291.83	0.0388
375	483.99	0.184
400	101.63	0.875
425	22.94	3.88

Figure 4.21: Solid phase epitaxy velocities determined from time-resolved reflectivity spectra for type A samples annealed at 350 °C, 375 °C, 400 °C, and 425 °C.

Anneal Temperature (^oC)	Oscillation Period (sec)	Interface Velocity (nm sec^{-1})
390	180.75	0.492
455	119.56	0.744
505	22.09	4.02

Figure 4.22: Solid phase epitaxy velocities determined from time-resolved reflectivity spectra for type B samples annealed at 390 °C, 455 °C, and 505 °C.

Anneal Temperature (°C)	Oscillation Period (sec)	Interface Velocity (nm sec^{-1})
300	1072.25	0.0829
350	206.20	0.431
375	91.64	0.970
400	48.96	1.82

Figure 4.23: Solid phase epitaxy velocities determined from time-resolved reflectivity spectra for type C samples annealed at 300 °C, 350 °C, 375 °C, and 400 °C.

Anneal Temperature (°C)	Oscillation Period (sec)	Interface Velocity (nm sec^{-1})
325	15.47	5.75
350	8.19	10.9
375	7.57	11.7

Figure 4.24: Solid phase epitaxy velocities determined from time-resolved reflectivity spectra for type D samples annealed at 325 °C, 350 °C, and 375 °C.

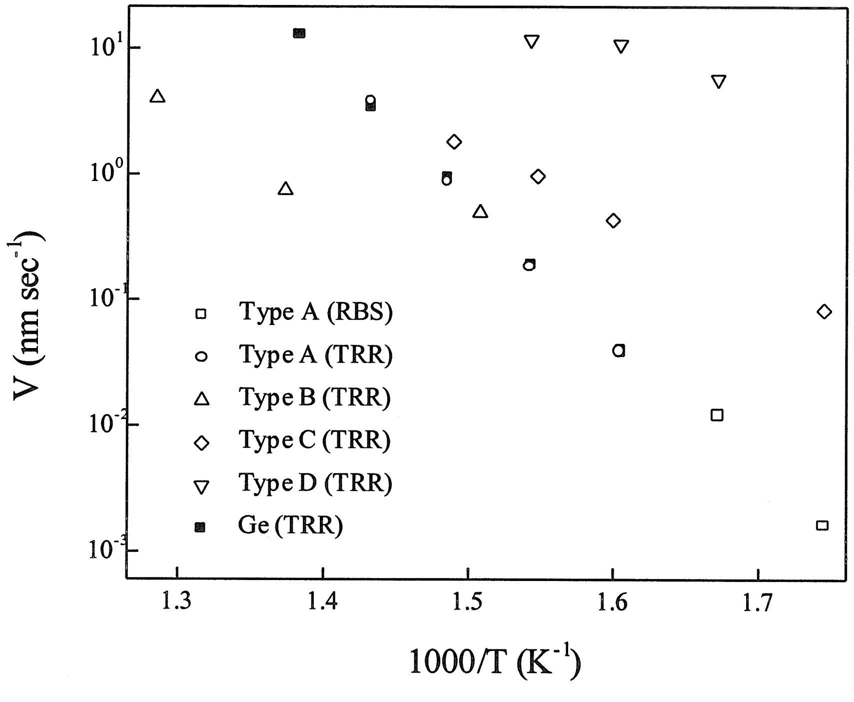

Figure 4.25: Solid phase epitaxy velocities for sample types A, B, C, and D and Ge [36].

Sample Type	Method	V_o (cm sec^{-1})	Q (eV)
A	Rutherford Backscattering	$1x10^{11}$	2.38
A	Time-Resolved Reflectivity	$8x10^{9} – 3x10^{10}$	2.30 ± 0.04
B	Time-Resolved Reflectivity	$6x10^{-5}$ – 10	0.8 ± 0.4
C	Time-Resolved Reflectivity	7 – 30	1.05 ± 0.04
D	Time-Resolved Reflectivity	$2x10^{-4}$ – 0.3	0.5 ± 0.2
Ge	Time-Resolved Reflectivity	$1x10^{9}$	2.26 ± 0.02

Figure 4.26: Solid phase epitaxy pre-exponential velocities and activation energies for sample types A, B, C, and D and Ge [36].

4.3 Pulsed Laser Deposition

Sn surface segregation is most likely a layer by layer process [41]. As a new surface layer of material is deposited, the Sn atoms located in the former surface layer segregate to the new surface layer. Sn atoms located beneath a complete layer or layers have greatly reduced segregation probability.

Figure 1.2 shows the estimated energy distribution for Si ablated at an energy density of approximately 3 J cm^{-2} as described in Chapter 1. The energy distributions for Sn and Ge ablated at an energy density of approximately 3 J cm^{-2} are assumed to be similar to the energy distribution shown in Figure 1.2. These energy distributions are expected to shift to higher energies as energy density is increased. This may act to increase or decrease Sn_xGe_{1-x} composition x.

If an atom is incident on an atom that forms the perimeter of a feature, the collision may result in displacement of the feature atom and replacement of the feature atom by the incident atom. This effect is referred to as feature atom displacement. An energy distribution for this effect was estimated by extrapolation from molecular dynamics simulation results for Si atom displacement yield from Si (001) surfaces irradiated by Ar^+ ions and is shown in Figure 2.3 [45]. A shift to higher energies is expected to translate into increased feature atom displacement. This is expected to increase Sn segregation and decrease Sn_xGe_{1-x} composition x.

An atom may undergo subsurface deposition. This effect is referred to as subplantation. An energy distribution for this effect was estimated from molecular dynamics simulation results for energetic Si growth on dihydride-terminated (1x1) Si (001) surfaces and is shown in Figure 3.2 for initial substrate temperatures of 0 K and

200 ^{o}C [46]. A shift to higher energies is expected to translate into increased subplantation and increased subplantation depth. This is expected to decrease Sn segregation and increase Sn_xGe_{1-x} composition x.

To evaluate the effect of energy distribution on alloy growth, Sn_xGe_{1-x} was grown by pulsed laser deposition, an energetic process.

4.3.1 Experiments

Each Si (001) substrate was cleaned and passivated as described in Chapter 1 and annealed at 400 °C to produce a monohydride-terminated (2x1) Si (001) surface.

The pulsed laser deposition system is described in detail in Chapter 1. The target was comprised of a polycrystalline Ge substrate and β-Sn wedges in a pie geometry. The target surface composition was approximately 0.55 Sn and 0.45 Ge. The energy density was varied by varying the position of the target relative to the position of the focusing lens and was estimated as described in Chapter 1. Crystalline Sn_xGe_{1-x} was grown at a deposition coverage of 0.001 nm pls^{-1}, a repetition rate of 10 pls sec^{-1}, and a time-averaged deposition rate of 0.01 nm sec^{-1} at a substrate temperature of 200 °C. Reflection high-energy electron diffraction was used at the onset of growth to confirm surface reconstruction and throughout growth to monitor crystallinity. Samples A and B were grown at energy densities of approximately 3 J cm^{-2} and 4 J cm^{-2}, respectively, and are described in Figure 4.27.

Samples A and B were characterized by 2 MeV He^{++} Rutherford backscattering spectrometry. Rump was used to analyze random orientation Sn and Ge backscattering profiles to determine microstructure and composition x [42].

Sample B was characterized by 15 keV scanning electron microscopy and electron microprobe analysis to determine microstructure and composition x.

Sample	Energy Density (J cm^{-2})	Thickness (nm)
A	3	36
B	4	18

Figure 4.27: Samples A and B.

4.3.2 Results

Figure 4.28 shows a scanning electron micrograph of sample B. Electron microprobe analysis indicated that the dark region is Sn_xGe_{1-x} with a composition x of 0.3 to 0.4 and that the light droplet-shaped regions are each a Sn region or a Ge region.

The exfoliational sputtering process described in Chapter 1 is expected to produce irregularly-shaped Sn and Ge regions. The hydrodynamic sputtering and condensation processes described in Chapter 1 are expected to produce droplet-shaped Sn and Ge regions. Sn segregation is expected to produce droplet-shaped Sn regions. The Sn and Ge regions shown in Figure 4.28 indicate that these processes, with the exception of the exfoliational sputtering process, may be active.

Figure 4.29 shows Rutherford backscattering spectra for samples A and B. The Sn and Ge backscattering profiles are each comprised of two components. The typical peak-shaped components most likely correspond to Sn_xGe_{1-x}. The atypical tail-shaped components most likely correspond to the Sn and Ge regions. For each backscattering profile, the latter component was extrapolated across the backscattering profile and subtracted from the backscattering profile. The resulting backscattering profiles were used to determine composition x. Samples A and B were estimated to have compositions x of 0.12 and 0.38, respectively.

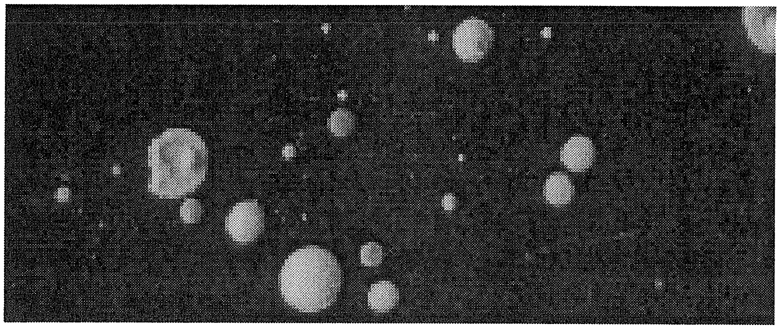

Figure 4.28: Scanning electron micrograph of sample B. The image area is approximately 90 μm by 36 μm.

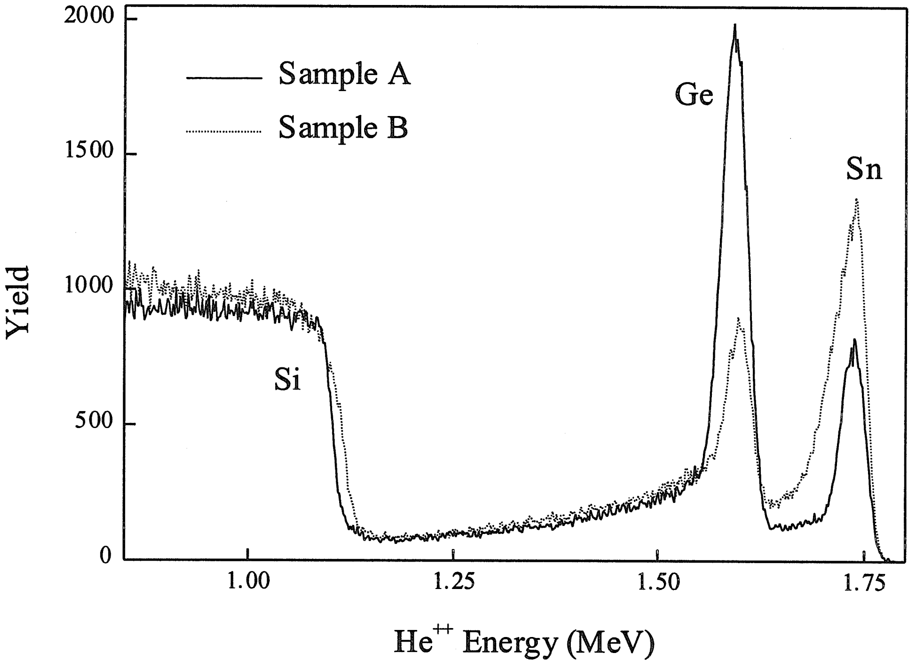

Figure 4.29: Rutherford backscattering spectra of samples A and B.

4.4 Conclusions

To evaluate the effect of energy distribution on alloy growth, Sn_xGe_{1-x} was grown by solid phase epitaxy, a thermal process, and by pulsed laser deposition, an energetic process.

Samples consisting of amorphous Sn_xGe_{1-x} grown on Ge grown on clean (2x1) Si (001) surfaces where composition x varied from 0.02 to 0.26 were annealed to initiate solid phase epitaxy. The crystalline Sn_xGe_{1-x} microstructures and compositions x were determined by transmission electron microscopy, x-ray diffraction, Rutherford backscattering spectrometry, and time-resolved reflectivity.

$Sn_{0.02}Ge_{0.98}$ samples were annealed at temperatures of 300 °C to 425 °C. Solid phase epitaxy occurred without Sn segregation, yielding Sn_xGe_{1-x} where composition x is approximately 0.02. The interface between Ge and $Sn_{0.02}Ge_{0.98}$ is characterized by crystallographic defects, indicating misfit strain relaxation. The interface between crystalline and amorphous $Sn_{0.02}Ge_{0.98}$ is characterized by pits resembling {111} facets located at the exit points of threading dislocations, indicating that interface velocity is lower near crystallographic defects.

$Sn_{0.10}Ge_{0.90}$ samples were annealed at temperatures of 300 °C to 505 °C. Solid phase epitaxy was accompanied by Sn segregation, yielding segregated Sn regions and Sn_xGe_{1-x} where composition x is approximately 0.05. Time-resolved reflectivity indicated a possible time delay between completion of solid phase epitaxy and onset of Sn segregation.

$Sn_{0.19}Ge_{0.81}$ samples were annealed at temperatures of 300 °C to 400 °C. $Sn_{0.26}Ge_{0.74}$ samples were annealed at temperatures of 300 °C to 375 °C. Solid phase epitaxy was accompanied by Sn segregation, yielding segregated Sn regions and Sn_xGe_{1-x} where composition x is approximately 0.05. Time-resolved reflectivity indicated simultaneous solid phase epitaxy and Sn segregation.

Crystalline Sn_xGe_{1-x} was grown on monohydride-terminated (2x1) Si (001) surfaces by pulsed laser deposition at energy densities of approximately 3 J cm^{-2} and 4 J cm^{-2}, a deposition coverage of 0.001 nm pls^{-1}, a repetition rate of 10 pls sec^{-1}, a time-averaged deposition rate of 0.01 nm sec^{-1}, and a substrate temperature of 200 ^{o}C.

Rutherford backscattering spectrometry indicated that samples grown at energy densities of approximately 3 J cm^{-2} and 4 J cm^{-2} have compositions x of approximately 0.12 and 0.38, respectively.

These results indicate that pulsed laser deposition is more feasible than solid phase epitaxy for production of Sn_xGe_{1-x} alloys in the desired composition range, most likely because of energetic effects such as subplantation.

References

[1] S. Oguz, W. Paul, T. T. Deutsch, B.-Y. Tsaur, and D. V. Murphy, Appl. Phys. Lett. 43, 848 (1983).

[2] I. T. H. Chang, B. Cantor, and A. G. Cullis, J. Non-Cryst. Solids 117-118, 263 (1990).

[3] S. M. Lee, J. Appl. Phys. 75, 1987 (1994).

[4] S. I. Shah, J. E. Greene, L. L. Abels, Q. Yao, and P. M. Raccah, J. Cryst. Growth 83, 3 (1987).

[5] A. Harwit, P. R. Pukite, J. Angilello, and S. S. Iyer, Thin Sol. Fi. 184, 395 (1990).

[6] J. Piao, R. Beresford, T. Licata, W. I. Wang, and H. Homma, J. Vac. Sci. Technol. B 8, 221 (1990).

[7] W. Wegscheider, K. Eberl, U. Menczigar, and G. Abstreiter, Appl. Phys. Lett. 57, 875 (1990).

[8] H.-J. Gossman, J. Appl. Phys. 68, 2791 (1990).

[9] E. A. Fitzgerald, P. E. Freeland, M. T. Asom, W. P. Lowe, R. A. Macharrie, Jr., B. E. Weir, A. R. Kortan, F. A. Thiel, Y.-H. Xie, A. M. Sergent, S. L. Cooper, G. A. Thomas, and L. C. Kimerling, J. Elec. Mat. 20, 489 (1991).

[10] K. Eberl, W. Wegscheider, and G. Abstreiter, J. Cryst. Growth 111, 882 (1991).

[11] P. Vogl, J. Olajos, W. Wegscheider, and G. Abstreiter, Surf. Sci. 267, 83 (1992).

[12] W. Wegscheider, J. Olajos, U. Menczigar, W. Dondl, and G. Abstreiter, J. Cryst. Growth 123, 75 (1992).

[13] O. Gurdal, M.-A. Hasan, M. R. Sardela, Jr., J. E. Greene, H. H. Radamson, J. E. Sundgren, and G. V. Hasson, Appl. Phys. Lett. 67, 956 (1995).

[14] G. He and H. A. Atwater, Nucl. Instrum. Methods Phys. Res. B 106, 126 (1995).

[15] G. He and H. A. Atwater, Appl. Phys. Lett. 68, 664 (1996).

[16] D. W. Jenkins and J. D. Dow, Phys. Rev. B 36, 7994 (1987).

[17] K. A. Mader, A. Baldereschi, and H. von Kanel, Solid State Comm. 69, 1123 (1989).

[18] T. Brudevoll, D. S. Citrin, N. E. Christensen, and M. Cardona, Phys. Rev. B 48, 17128 (1993).

[19] H. A. Atwater, G. He, and K. Saipetch, Mat. Res. Soc. Symp. Proc. 355, 123 (1995).

[20] N. A. Amrane, S. A. Abderrahmane, and H. Aourag, Infrared Phys. and Tech. 36, 843 (1995).

[21] B. Bouhafs, F. Benkabou, M. Ferhat, B. Khelifa, J. P. Dufour, and H. Aourag, Infrared Phys. and Tech. 36, 967 (1995).

[22] E. Kaxiras.

[23] G. He and H. A. Atwater, Phys. Rev. Lett. 79, 1937 (1997).

[24] C. D. Thurmond, F. A. Trumbore, and M. Kowalchik, J. Chem. Phys. 24, 799 (1956).

[25] T. Soma, H. Matsuo, and S. Kagaya, Phys. Status Solidi 105, 311 (1981).

[26] Binary Alloy Phase Diagrams, Ed. T. B. Massalski, Am. Soc. Metals, Materials Park, 1990.

[27] Tapp, E S Microware.

[28] W. Klemm and H. Stohr, Z. Anorg. Allg. Chem. 241, 305 (1939).

[29] R. C. Farrow, D. S. Robertson, G. M. Williams, A. G. Cullis, G. R. Jones, I. M. Young, and P. N. J. Dennis, J. Cryst. Growth 54, 507 (1981).

[30] J. L. Reno and L. L. Stephenson, Appl. Phys. Lett. 54, 2207 (1989).

[31] M. T. Asom, A. R. Kortan, L. C. Kimerling, and R. C. Farrow, Appl. Phys. Lett. 55, 1439 (1989).

[32] T. Ito, Jpn. J. Appl. Phys. 31, L920 (1992).

[33] G. A. Busch and R. Kern, Solid State Physics, Ed. F. Seitz and D. Turnbull, Academic Press, New York, 1960.

[34] M. E. Taylor, G. He, C. Saipetch, and H. A. Atwater, Mat. Res. Soc. Symp. Proc. 388, 97 (1995).

[35] M. E. Taylor, G. He, and H. A. Atwater, J. Appl. Phys. 80, 4384 (1996).

[36] G. L. Olson and J. A. Roth, Handbook of Crystal Growth, Ed. D. T. J. Hurle, Elsevier, Amsterdam, 1994.

[37] D. C. Paine, D. J. Howard, N. G. Stoffel, and J. A. Horton, J. Mater. Res. 5, 1023 (1990).

[38] C. Lee, T. E. Haynes, and K. S. Jones, Appl. Phys. Lett. 62, 501 (1993).

[39] Semiquant, Edax.

[40] B. Fultz and J. Howe, Transmission Electron Microscopy and Diffractometry of Materials.

[41] J. Y. Tsao, Materials Fundamentals of Molecular Beam Epitaxy, Academic Press, New York, 1993.

[42] Rump, L. R. Doolittle, M. O. Thompson, R. C. Cochran, and J. W. Mayer.

[43] Origin, Microcal Origin.

[44] Handbook of Optical Constants of Solids, Ed. E. D. Palik, Academic Press, Orlando, 1985.

[45] M. V. R. Murty and H. A. Atwater, Phys. Rev. B 45, 1507 (1992).

[46] M. V. R. Murty and H. A. Atwater, Surf. Sci. 374, 283 (1997).

Appendix A

Simulation Accuracy

A.1 Background

To ascertain the accuracy of the simulation, actual growth morphologies were compared to simulated growth morphologies for Si growth by molecular beam deposition and pulsed laser deposition. The simulation and the metrics used to evaluate growth morphology are described in detail in Chapter 2.

It should be noted that the simulation is a schematic representation of Si growth. The simulation was developed to qualitatively simulate the effects of temporal distribution and energy distribution on growth morphology rather than to quantitatively simulate Si growth. It should also be noted that a number of potentially important effects are not simulated. These effects include bulk displacement, radiation damage, hydrogen termination, surface reconstruction, anisotropic surface diffusion, anisotropic bonding, and surface diffusion involving step edge heights greater than two monolayers.

Since Si has a diamond cubic structure, one unit lattice cell corresponds to four monolayers. This relationship was used in conjunction with the lattice parameter of Si to convert monolayers to nanometers to facilitate comparison of simulation to experiment.

A.2 Experiments

Each Si (001) substrate was cleaned and passivated as described in Chapter 1 and annealed at 380 °C to produce a monohydride-terminated (2x1) Si (001) surface.

The molecular beam deposition chamber has a base pressure of $2\text{x}10^{-10}$ torr. Crystalline Si was grown at a deposition rate of 0.013 nm sec^{-1}. Because a submonolayer contamination layer typically makes the interface between the substrate and the film visible by transmission electron microscopy, no marker layer was grown prior to Si growth. Reflection high-energy electron diffraction was used at the onset of growth to confirm surface reconstruction and throughout growth to monitor crystallinity.

The pulsed laser deposition chamber is described in detail in Chapter 1. Polycrystalline Si and Ge substrates were used as targets. An energy density of approximately 3 J cm^{-2} was used. Crystalline Si was grown at a deposition coverage of 0.0005 nm pls^{-1}, a repetition rate of 25 pls sec^{-1}, and a time-averaged deposition rate of 0.0125 nm sec^{-1}. To make the interface between the substrate and the film visible by transmission electron microscopy, a submonolayer Ge layer was grown prior to Si growth. Reflection high-energy electron diffraction was used at the onset of growth to confirm surface reconstruction and throughout growth to monitor crystallinity.

Samples A and C were grown by molecular beam deposition at substrate temperatures of 280 °C and 380 °C, respectively. Samples B and D were grown by pulsed laser deposition at substrate temperatures of 280 °C and 380 °C, respectively. Samples A and D underwent transitions from crystalline growth to amorphous growth. Transitions of this type are described in Chapter 3. The surfaces of interest are the surfaces of the crystalline layers. The samples are described in Figure A.1.

The samples were characterized by 200 keV cross-sectional high-resolution transmission electron microscopy. The micrographs were converted to digital images using a scanner. Adobe Photoshop was used to generate surface profiles S(x) from the digital images [1]. Origin was used to determine root-mean square roughnesses R and Fourier height correlation functions M(k) and to linearly fit the Fourier height correlation functions M(k) [2]. In each linear fit, k values smaller than 0.03 nm^{-1} were discarded because of possible Fourier transform edge effects and k values larger than 2.5 nm^{-1} were discarded because of possible discrete atom effects. These k values correspond to features larger than 33 nm and smaller than 0.4 nm, respectively.

A.3 Simulations

In each simulation, material was deposited on an initially flat surface. The molecular beam deposition simulations used the thermal energy distribution and the continuous temporal distribution at a deposition rate of 0.013 nm sec^{-1}. The pulsed laser deposition simulations used the energetic energy distribution and the pulsed temporal distribution at a deposition coverage of 0.0005 nm pls^{-1}, a repetition rate of 25 pls sec^{-1}, and a time-averaged deposition rate of 0.0125 nm sec^{-1}.

In each simulation, a 40 nm by 4 nm cell size was used. The 40 nm axis was selected to correspond to a typical cross-sectional high-resolution transmission electron microscopy sample thickness. The 4 nm axis was selected to minimize computation time.

Simulations A and C are molecular beam deposition simulations at substrate temperatures of 280 °C and 380 °C, respectively. Simulations B and D are pulsed laser deposition simulations at substrate temperatures of 280 °C and 380 °C, respectively. The simulations are described in Figure A.1.

For each simulation, Origin was used to generate a surface image [2]. Each pair of integer coordinates in the x-y plane of the image has an associated height value equal to the height of the surface atom located at the corresponding position in the x-y plane of the film. To aid interpretation, non-integer pairs of coordinates have associated height values obtained by linear interpolation of height values associated with surrounding pairs of integer coordinates. The height values are represented using a gray scale in which white represents a maximum value and black represents a minimum value.

For each simulation, Origin was used to determine two root-mean square roughnesses representing the root-mean square roughnesses that would be observed if the simulation were to be characterized by cross-sectional high-resolution transmission electron microscopy at two cross-sectional thicknesses [2]. The maximum root-mean square roughness R_{max} is equal to the mean of the root-mean square roughnesses of the surface profiles S(x) generated from the 40 nm rows. The minimum root-mean square roughness R_{min} is equal to the root-mean square roughness of the surface profile S(x) generated from the maximum values of the 40 nm rows. R_{max} would be observed if the cross-sectional thickness were a single atomic layer. R_{min} would be observed if the cross-sectional thickness were 40 nm.

For each simulation a surface profile S(x) was generated from a randomly selected 40 nm row. Origin was used to determine Fourier height correlation functions M(k) and to linearly fit the Fourier height correlation functions M(k) [2]. In each linear fit, k values smaller than 0.03 nm^{-1} were discarded because of possible Fourier transform edge effects and k values larger than 2.5 nm^{-1} were discarded because of possible discrete atom effects. These k values correspond to features larger than 33 nm and smaller than 0.4 nm, respectively.

Sample & Simulation	Deposition Process Type	Substrate Temperature (^oC)	Sample Thickness (nm)	Simulation Thickness (nm)
A	Molecular Beam	280	0.94	0.92
B	Pulsed Laser	280	1.00	0.95
C	Molecular Beam	380	6.06	6.19
D	Pulsed Laser	380	7.83	7.84

Figure A.1: Samples A, B, C, and D and simulations A, B, C, and D.

A.4 Results

Figures A.2 through A.5 show cross-sectional <110> high-resolution transmission electron micrographs of samples A, B, C, and D, respectively. Figures A.6 through A.9 show partial surface images of simulations A, B, C, and D, respectively. Figures A.10 through A.13 show surface profiles S(x) for samples A and C, samples B and D, simulations A and C, and simulations B and D, respectively. The surface profiles S(x) shown in Figures A.12 and A.13 were generated from randomly selected 40 nm rows.

Figures A.14 and A.15 show root-mean square roughnesses R for samples A, B, C, and D and root-mean square roughnesses R_{min} and R_{max} for simulations A, B, C, and D. For each sample and simulation, R is between R_{min} and R_{max}. For samples and simulations A and B, R is similar to R_{max}. For samples and simulations C and D, R is similar to the mean of R_{min} and R_{max}. Comparison of R to R_{max} and to the mean of R_{min} and R_{max} indicates that the simulation correctly estimates greater roughness in simulations A and C than in simulations B and D, respectively.

Figures A.16 through A.19 show Fourier height correlation functions M(k) for sample A and simulation A, sample B and simulation B, sample C and simulation C, and sample D and simulation D, respectively. Comparison of sample M(k) to simulation M(k) indicates that the simulation correctly predicts transitions from relatively flat slopes indicating feature size distributions dominated by roughening to relatively negative slopes indicating feature size distributions dominated by smoothening as k is increased.

Figures A.20 through A.23 show Fourier height correlation functions M(k) for samples A and B, simulations A and B, samples C and D, and simulations C and D, respectively. Comparison of sample M(k) to simulation M(k) indicates that the simulation correctly estimates greater roughness in simulations A and C than in simulations B and D, respectively.

Figure A.24 shows Fourier height correlation function M(k) linear fit exponents for samples A, B, C, and D and simulations A, B, C, and D. The exponents for simulations A and B are more positive than the exponents for samples A and B, respectively, indicating that the simulation estimates a feature size distribution influenced too heavily by roughening and too lightly by smoothening. The exponents for simulations C and D are within error of the exponents for samples C and D, respectively, indicating that the simulation estimates a feature size distribution influenced by a correct balance of roughening and smoothening.

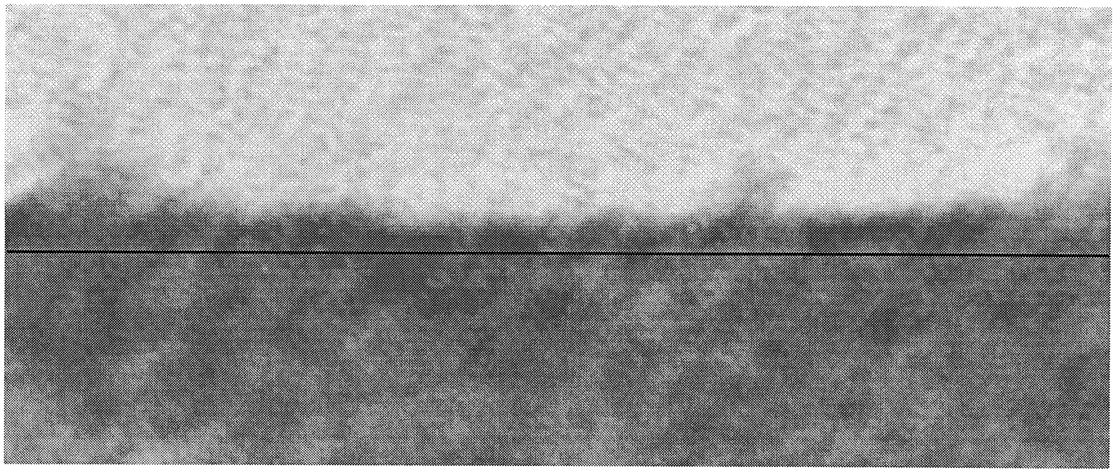

Figure A.2: Cross-sectional <110> high-resolution transmission electron micrograph of sample A. The image area is approximately 22 nm by 9 nm. The line demarcates the boundary between the substrate and the film.

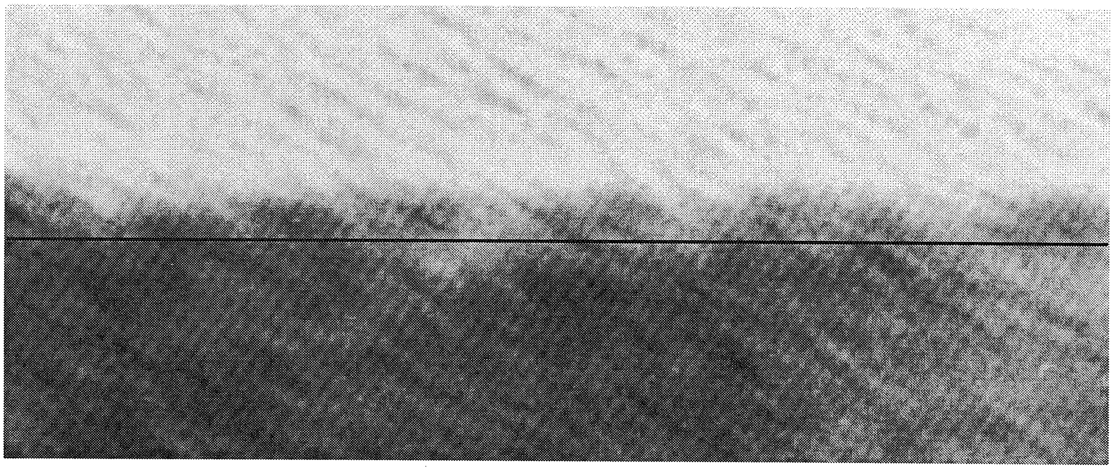

Figure A.3: Cross-sectional <110> high-resolution transmission electron micrograph of sample B. The image area is approximately 22 nm by 9 nm. The line demarcates the boundary between the substrate and the film.

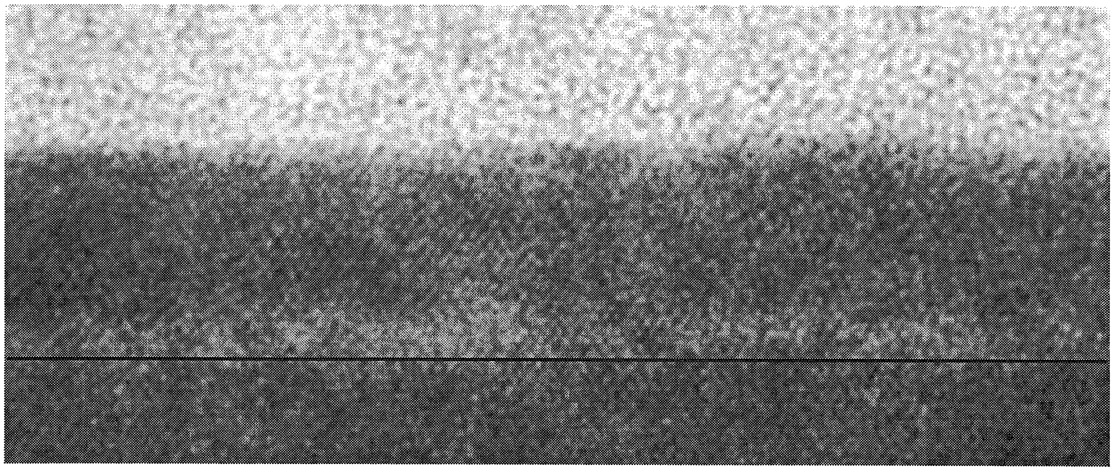

Figure A.4: Cross-sectional <110> high-resolution transmission electron micrograph of sample C. The image area is approximately 32 nm by 13 nm. The line demarcates the boundary between the substrate and the film.

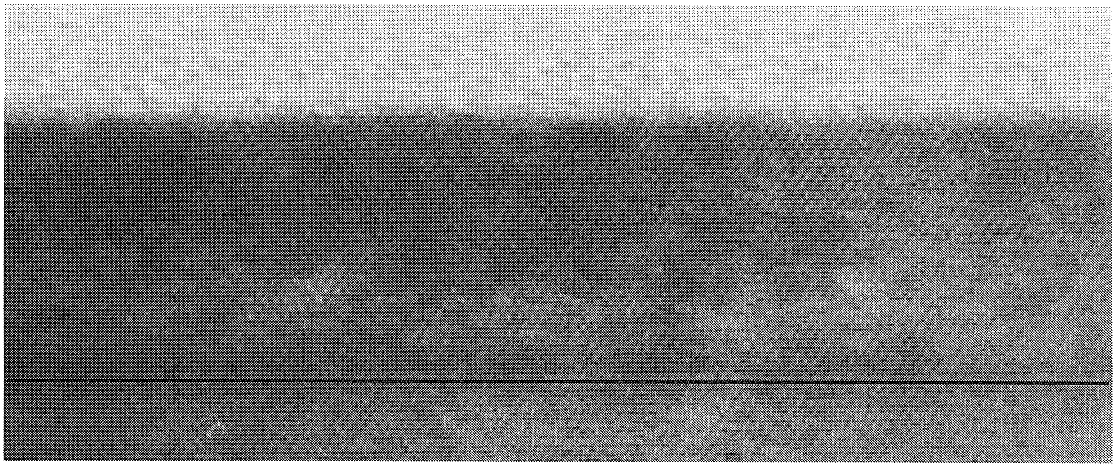

Figure A.5: Cross-sectional <110> high-resolution transmission electron micrograph of sample D. The image area is approximately 32 nm by 13 nm. The line demarcates the boundary between the substrate and the film.

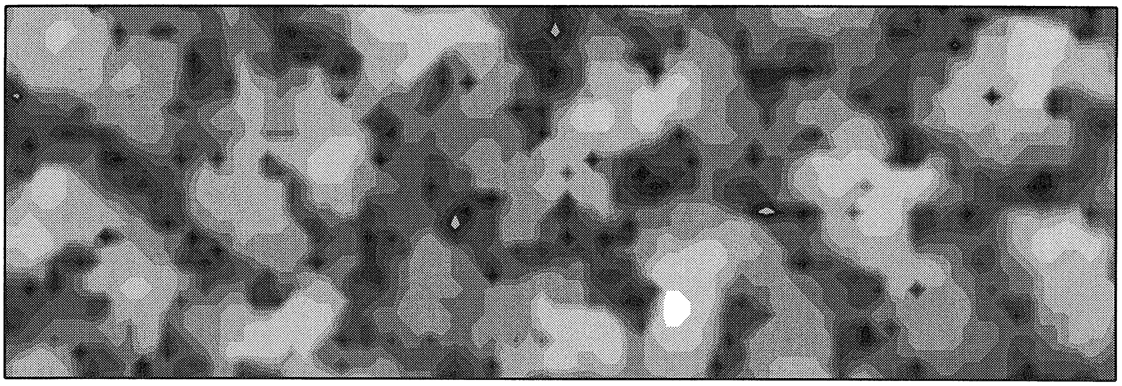

Figure A.6: Partial surface image of simulation A. The image area is approximately 12 nm by 4 nm. Black and white represent thicknesses of 0 nm and 1.5 nm, respectively.

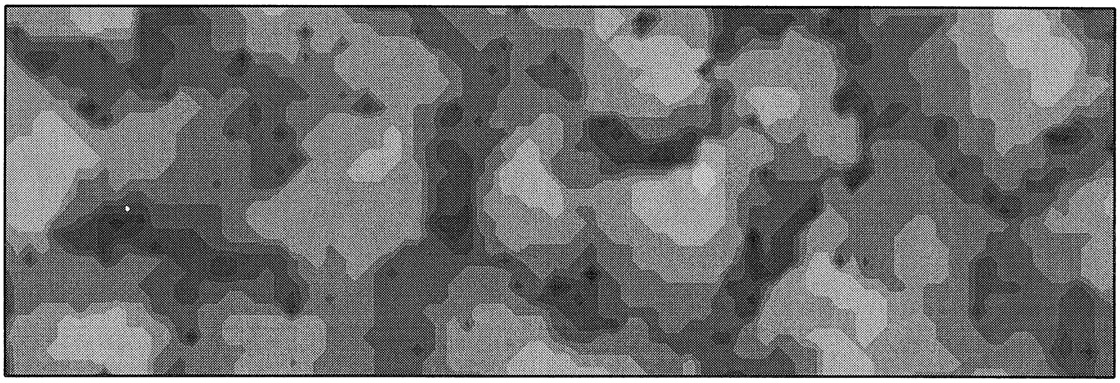

Figure A.7: Partial surface image of simulation B. The image area is approximately 12 nm by 4 nm. Black and white represent thicknesses of 0 nm and 1.5 nm, respectively.

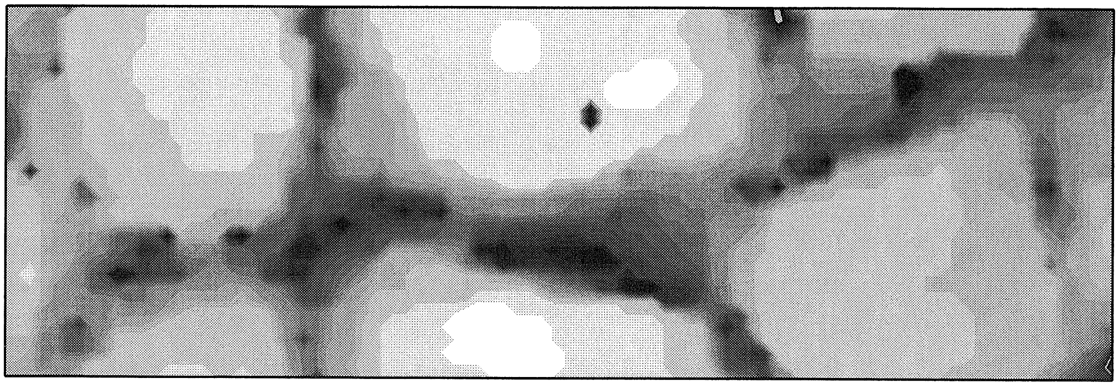

Figure A.8: Partial surface image of simulation C. The image area is approximately 12 nm by 4 nm. Black and white represent thicknesses of 4.0 nm and 6.8 nm, respectively.

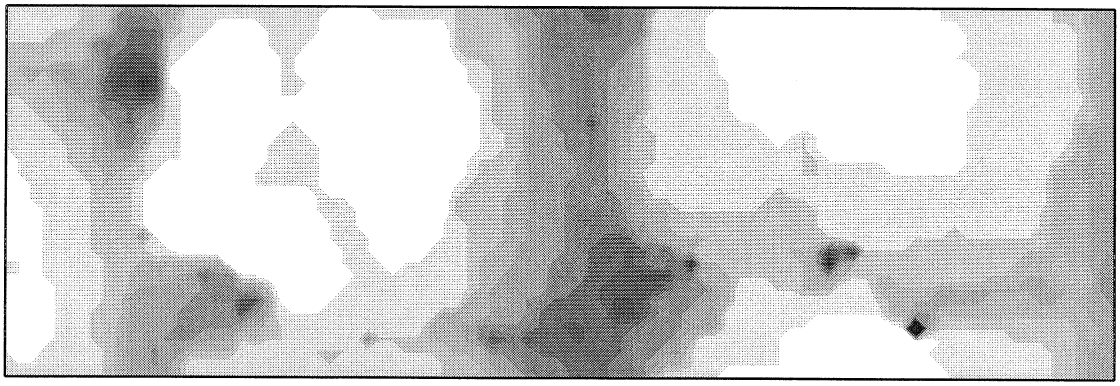

Figure A.9: Partial surface image of simulation D. The image area is approximately 12 nm by 4 nm. Black and white represent thicknesses of 5.4 nm and 8.2 nm, respectively.

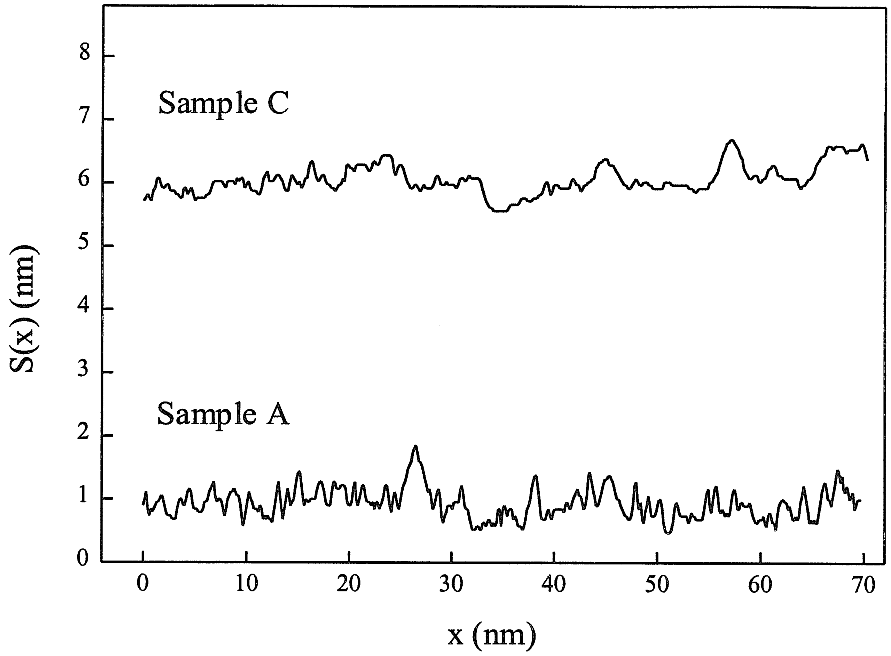

Figure A.10: Surface profiles of samples A and C.

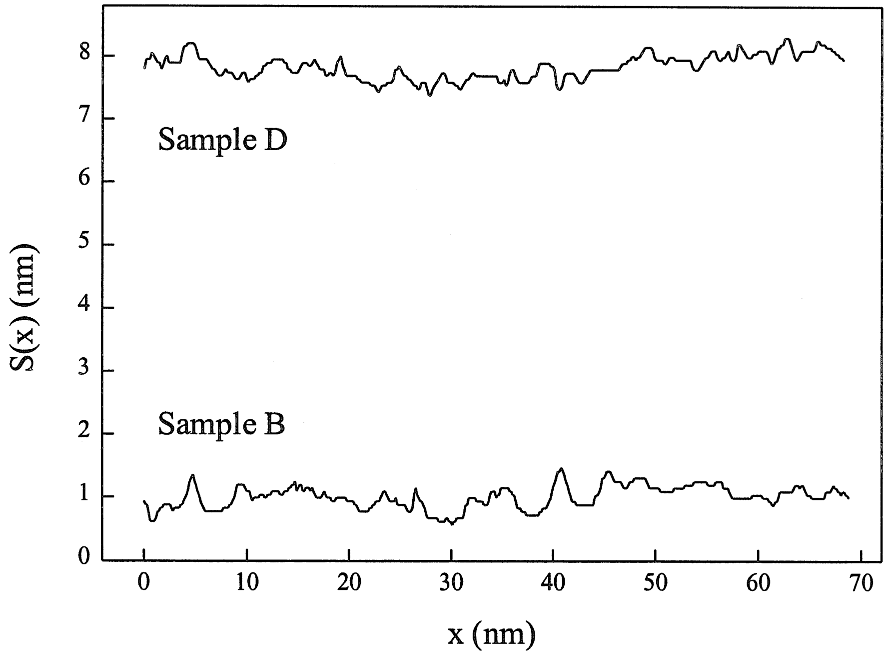

Figure A.11: Surface profiles of samples B and D.

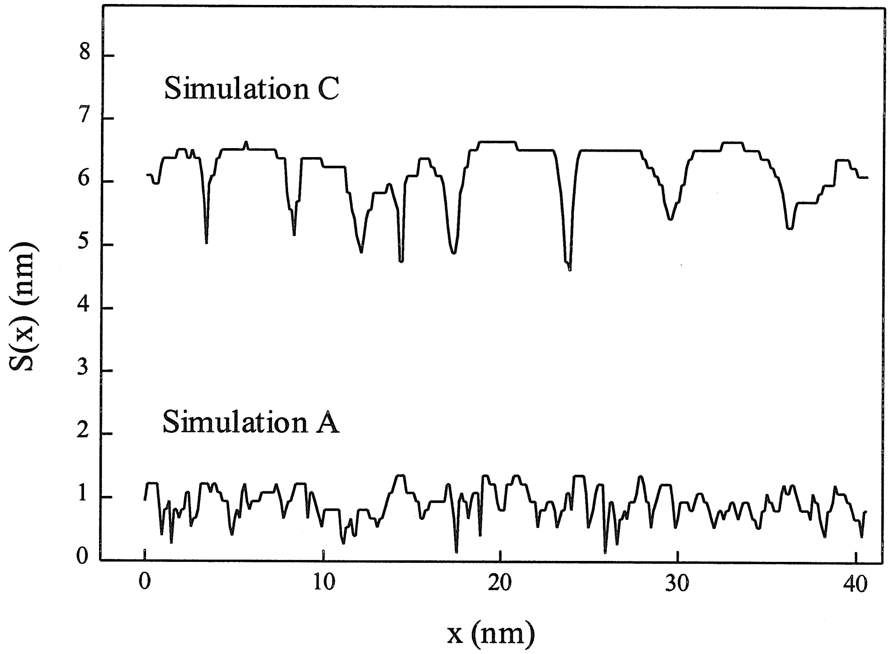

Figure A.12: Surface profiles of simulations A and C.

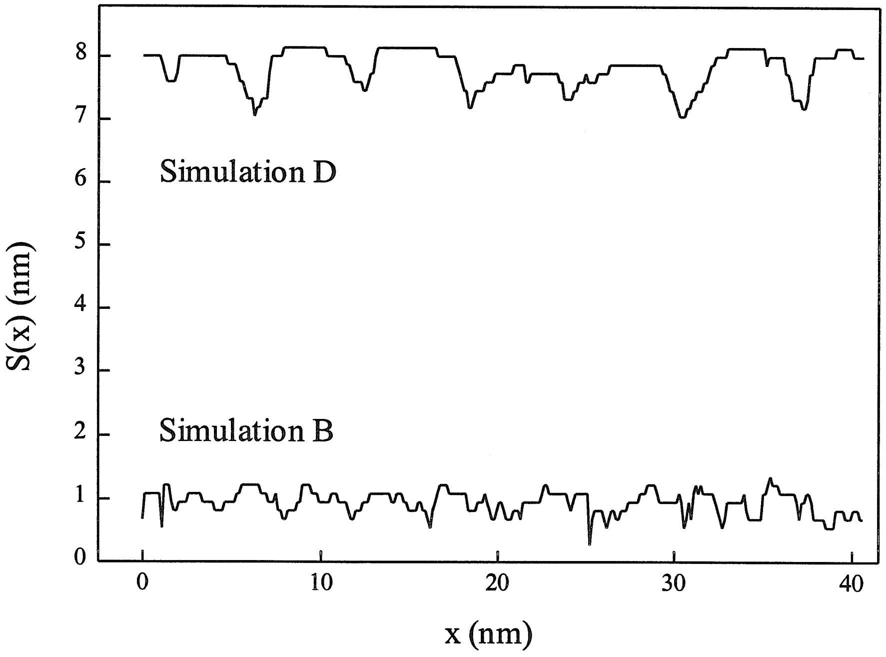

Figure A.13: Surface profiles of simulations B and D.

Sample & Simulation	Sample R (nm)	Simulation R_{min} (nm)	Simulation R_{max} (nm)
A	0.23	0.065	0.276 ± 0.002
B	0.18	0.055	0.183 ± 0.001
C	0.24	0.056	0.502 ± 0.010
D	0.20	0.075	0.310 ± 0.007

Figure A.14: Root-mean square roughnesses for samples A, B, C, and D and minimum and maximum root-mean square roughnesses for simulations A, B, C, and D.

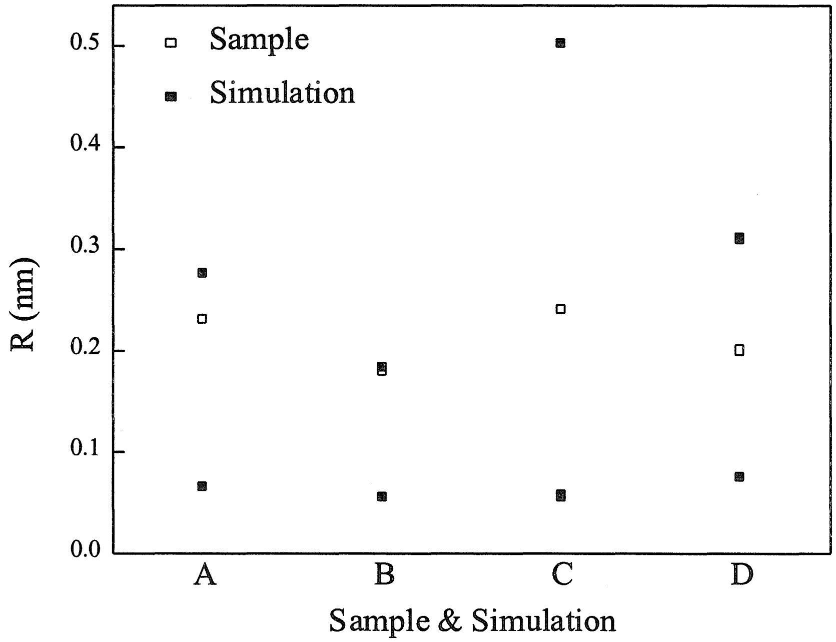

Figure A.15: Root-mean square roughnesses for samples A, B, C, and D and minimum and maximum root-mean square roughnesses for simulations A, B, C, and D.

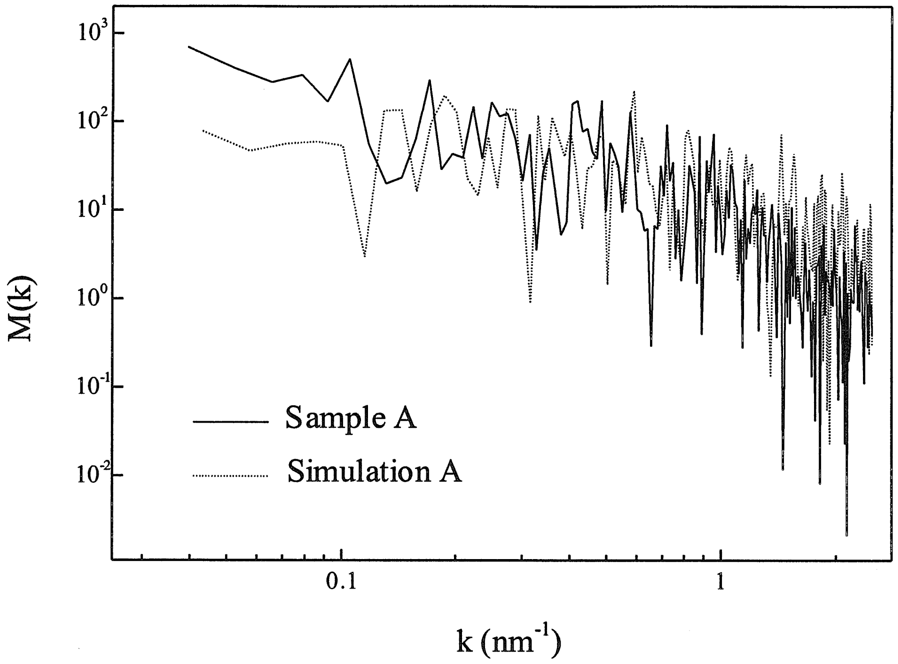

Figure A.16: Fourier height correlation functions for sample A and simulation A.

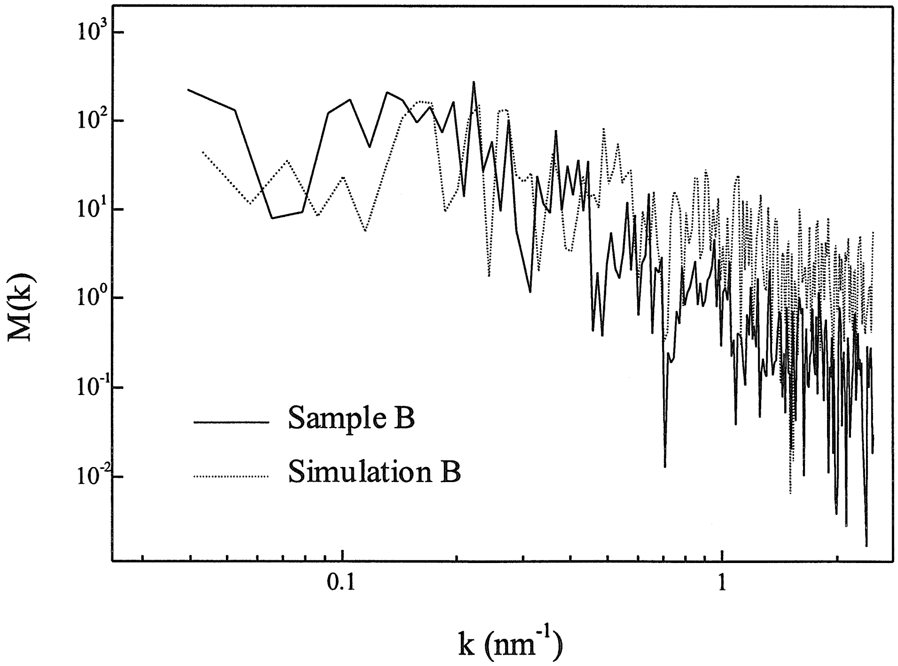

Figure A.17: Fourier height correlation functions for sample B and simulation B.

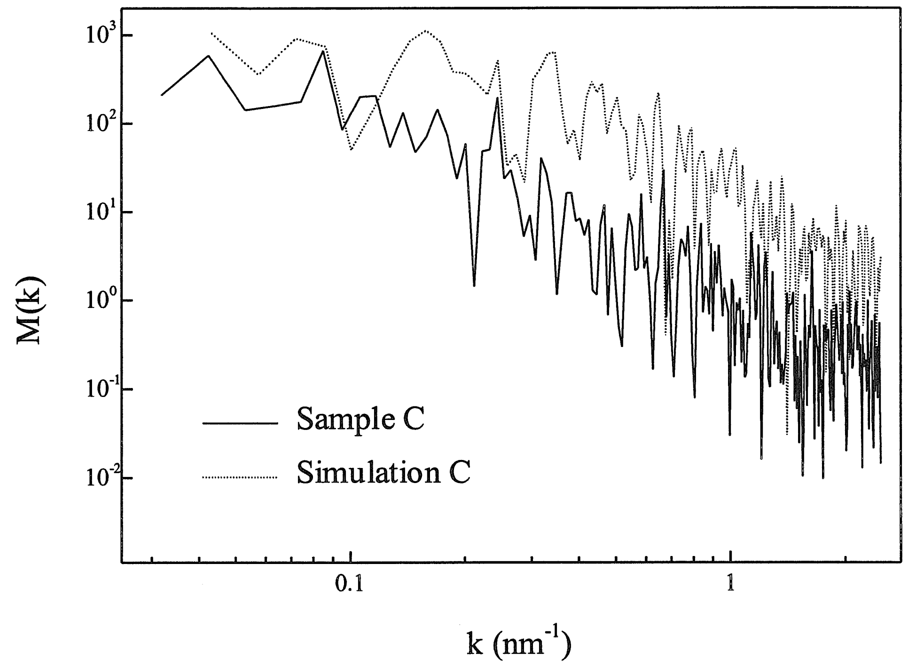

Figure A.18: Fourier height correlation functions for sample C and simulation C.

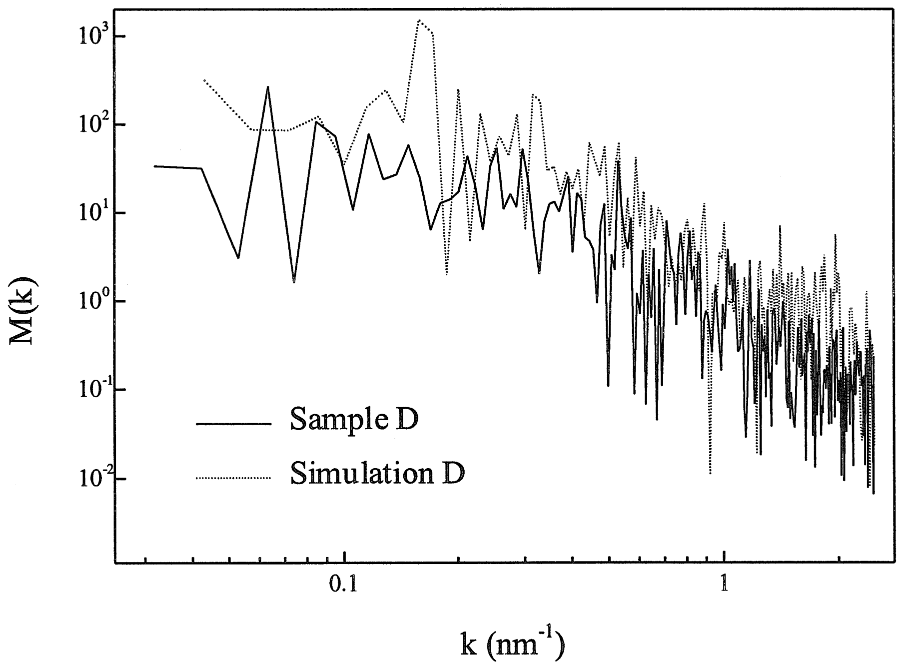

Figure A.19: Fourier height correlation functions for sample D and simulation D.

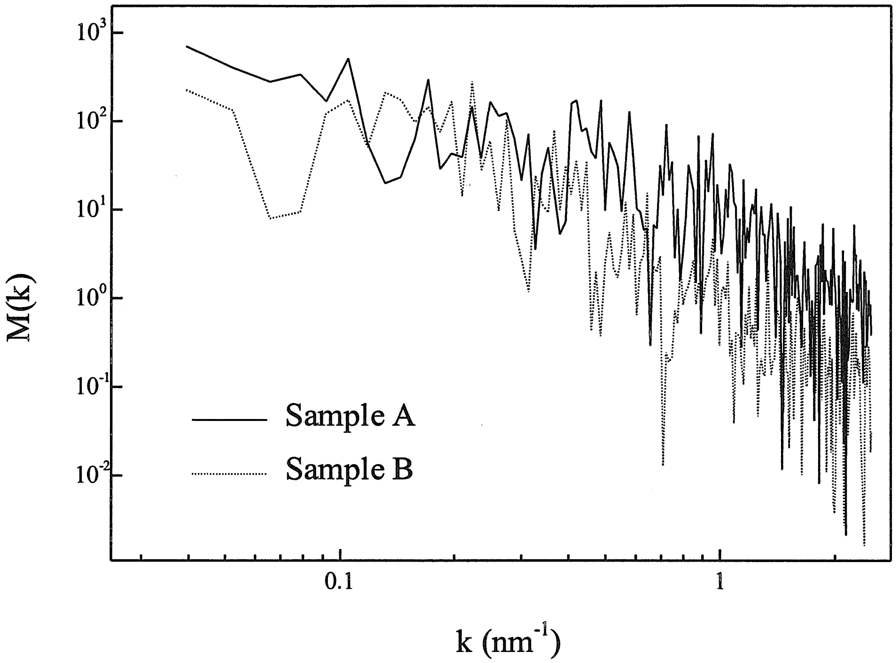

Figure A.20: Fourier height correlation functions for samples A and B.

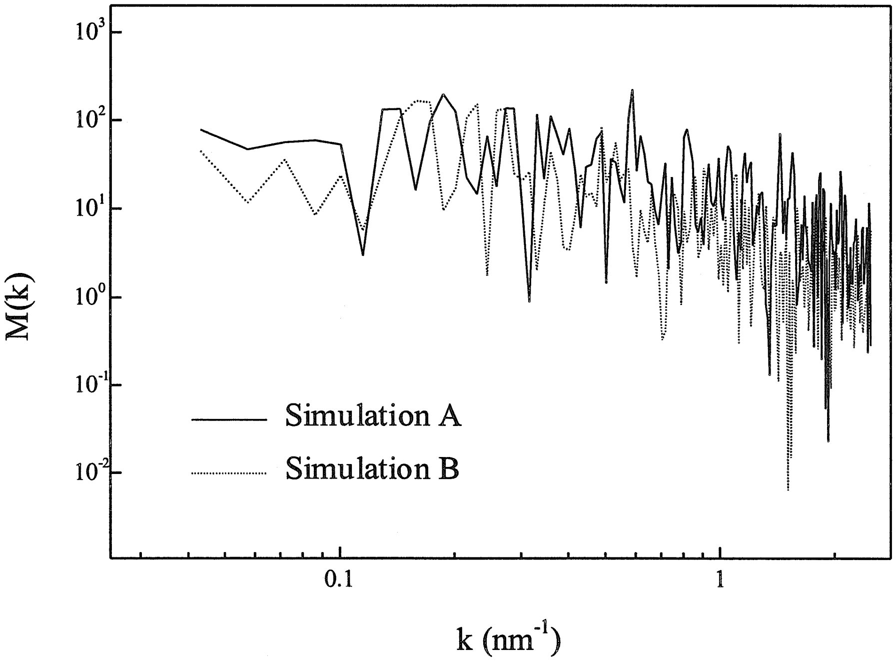

Figure A.21: Fourier height correlation functions for simulations A and B.

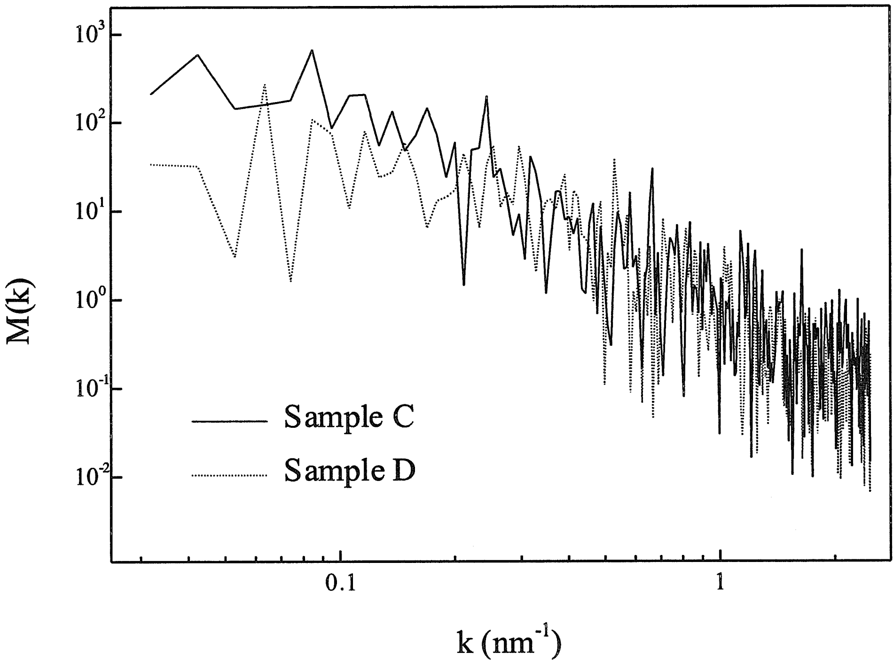

Figure A.22: Fourier height correlation functions for samples C and D.

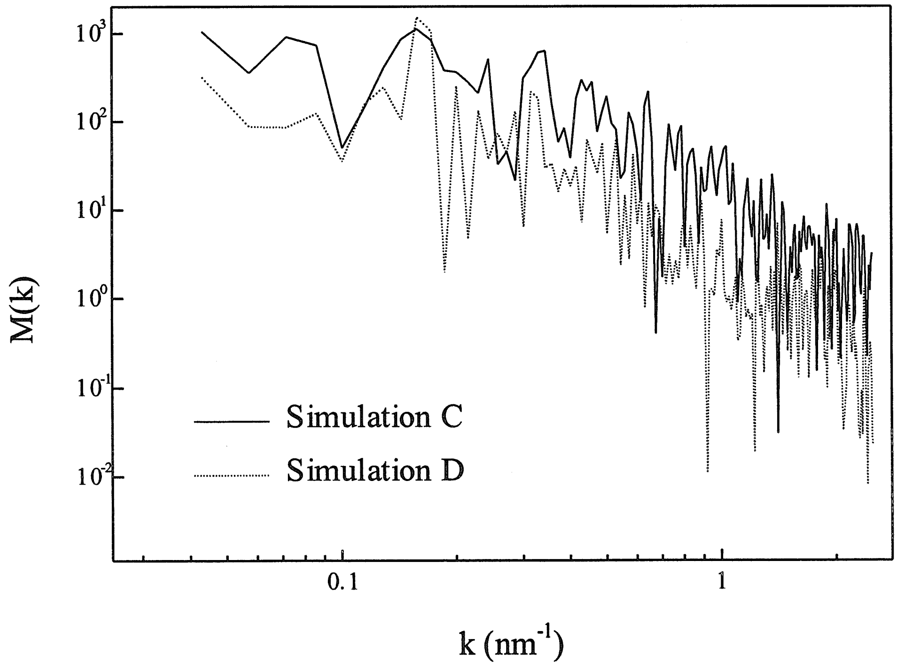

Figure A.23: Fourier height correlation functions for simulations C and D.

Sample & Simulation	k (nm^{-1})	x (nm)	Sample Linear Fit Exponent	Simulation Linear Fit Exponent
A	0.03 – 0.42	2.4 – 33.3	-1.0 ± 0.3	-0.2 ± 0.3
A	0.42 – 2.50	0.4 – 2.4	-2.7 ± 0.2	-1.6 ± 0.2
B	0.03 – 0.22	4.5 – 33.3	-0.3 ± 0.5	1.1 ± 0.5
B	0.22 – 2.50	0.4 – 4.5	-2.5 ± 0.2	-1.5 ± 0.2
C	0.03 – 0.16	6.3 – 33.3	-1.1 ± 0.3	-0.2 ± 0.6
C	0.16 – 2.50	0.4 – 6.3	-2.2 ± 0.1	-2.4 ± 0.1
D	0.03 – 0.32	3.1 – 33.3	-0.7 ± 0.3	-0.8 ± 0.5
D	0.32 – 2.50	0.4 – 3.1	-2.4 ± 0.2	-2.7 ± 0.2

Figure A.24: Fourier height correlation function linear fit exponents for samples A, B, C, and D and simulations A, B, C, and D.

A.5 Conclusions

Crystalline Si was grown on monohydride-terminated (2x1) Si (001) surfaces by molecular beam deposition at a deposition rate of 0.013 nm sec^{-1} and by pulsed laser deposition at an energy density of approximately 3 J cm^{-2}, a deposition coverage of 0.0005 nm pls^{-1}, a repetition rate of 25 pls sec^{-1}, and a time-averaged deposition rate of 0.013 nm sec^{-1} at substrate temperatures of 280 °C and 380 °C. These growth morphologies were compared to simulated growth morphologies.

Root-mean square roughness analysis indicated that the simulation estimates roughness consistent with experiment when cross-sectional high-resolution transmission electron microscopy sample thickness is considered.

Fourier height correlation analysis indicated that the simulation correctly predicts transitions from feature size distributions dominated by roughening to feature size distributions dominated by smoothening. Fourier height correlation analysis also indicated that the simulation estimates a feature size distribution influenced too heavily by roughening and too lightly by smoothening in the 280 °C simulations and influenced by a correct balance of roughening and smoothening in the 380 °C simulations.

Root-mean square roughness analysis and Fourier height correlation analysis indicated that the simulation correctly estimates greater roughness in the molecular beam deposition simulations than in the pulsed laser deposition simulations.

These results are encouraging but not definitive. The samples were grown on monohydride-terminated (2x1) Si (001) surfaces rather than on clean (2x1) Si (001) surfaces because the pulsed laser deposition system is limited to a maximum safe substrate temperature of approximately 420 °C. Thin samples were grown because computer memory restrictions limited the simulation thickness. The samples were characterized by cross-sectional high-resolution transmission electron microscopy rather than by atomic force microscopy or by scanning tunneling microscopy because *in situ* atomic force microscopy and *in situ* scanning tunneling microscopy were not available and because *ex situ* atomic force microscopy provided no meaningful results, possibly because of small sample thickness and sample oxidation. Hydrogen termination most likely affects growth morphology. Cross-sectional high-resolution transmission electron microscopy sample thickness most likely affects evaluation of growth morphology. To definitively ascertain the accuracy of the simulation, more precise experiments should be undertaken. Samples could be grown on clean (2x1) Si (001) surfaces. Thin samples with small roughness could be characterized by *in situ* atomic force microscopy or by *in situ* scanning tunneling microscopy and compared to the simulation. Thicker samples with greater roughness could be characterized by *in situ* or *ex situ* atomic force microscopy and compared to a one-dimensional analog of the simulation.

References

[1] Adobe Photoshop, Adobe Systems.

[2] Origin, Microcal Origin.

Appendix B

Simulation Code

```
#include <stdio.h>
#include <stdlib.h>
#include <time.h>
#include <math.h>
#ifndef RAND_MAX
#define RAND_MAX 2147483647
#endif

#define SWAP(a,b) tempr=(a);(a)=(b);(b)=tempr

int Nat;                    /* Substrate dimensions. */
int Fat;                    /* Fourier dimensions. */
int Natom;                  /* Number of atoms. */
int Nsub;                   /* Number of substrate atoms. */
int Nact;                   /* Number of active atoms. */
int Nper;                   /* Atoms deposited per pulse. */
int Ndep;                   /* Number of deposited atoms. */
int pulse;                  /* Growth type. */
int N[12];                  /* Numbers of candidate jumps of each jump type: [type] */
int *atrack;                /* Active atom list: [position] */
int *ctrack;                /* Atom positions in active atom list: [atom] */
int ***surf;                /* Surface atom info: [x][y][height,atom] */
int **dep;                  /* Atom positions: [atom][x,y,z] */
int **situ;                 /* Atom jump type tracker: [atom][dir] */
int **neighx;               /* Neighboring x positions: [x][dir] */
int **neighy;               /* Neighboring y positions: [y][dir] */
float *ftrans;              /* Fourier transform input: [site] */
float **fsurf;              /* Fourier transform output: [x][y] */
double brprob;              /* Breaking probability. */
double thermal;             /* Thermal energy in eV. */
double kin;                 /* Energetic energy in eV. */
double barrier[12];         /* Activation barriers for jump types in eV: [type] */
double *energy;             /* Atom energies in eV: [atom] */
double **kinet;             /* Energetic energy info: [atom][energy,brprob] */
double **rate;              /* Atom jump rates: [atom][dir] */

double ran0 ()              /* Numerical Recipes random uniform deviate routine. */
{
    static double y,maxran,v[98];
    double dum;
    static int iff=0;
    int j;
    if (iff==0)
    {
        iff=1;
        maxran=RAND_MAX+1.0;
        srand((unsigned)time(NULL));
        for (j=1;j<=97;j++)
            dum=rand();
        for (j=1;j<=97;j++)
            v[j]=rand();
        y=rand();
    }
    j=1+(int)(97.0*y/maxran);
    y=v[j];
    v[j]=rand();
```

```
    return y/maxran;
}

double expdev ()                    /* Numerical Recipes random exponential deviate routine. */
{
    double dum,ran0();
    do
        dum=ran0();
    while (dum==0.0);
    return -log(dum);
}

void fourn ()                       /* Numerical Recipes multidimensional FFT routine. */
{
    int i,j,k;
    int ndim,idim,isign;
    unsigned long i1,i2,i3,i2rev,i3rev,ip1,ip2,ip3,ifp1,ifp2;
    unsigned long ibit,k1,k2,n,nprev,nrem,ntot;
    unsigned long nn[3];
    float tempi,tempr;
    float avcov;
    double theta,wi,wpi,wpr,wr,wtemp;
    isign=1;
    ndim=2;
    nn[0]=0;
    nn[1]=Nat;
    nn[2]=Nat;
    avcov=(float)(0.0);
    for (i=0;i<Nat;i++)
    {
        for (j=0;j<Nat;j++)
            avcov=avcov+(float)(surf[i][j][0]);
    }
    avcov=avcov/((float)(Nsub));
    ftrans[0]=(float)(0.0);
    k=1;
    for (i=0;i<Nat;i++)
    {
        for (j=0;j<Nat;j++)
        {
            ftrans[k]=((float)(surf[i][j][0]))-avcov;
            k=k+1;
            ftrans[k]=(float)(0.0);
            k=k+1;
        }
    }
    for (ntot=1,idim=1;idim<=ndim;idim++)
        ntot *= nn[idim];
    nprev=1;
    for (idim=ndim;idim>=1;idim--)
    {
        n=nn[idim];
        nrem=ntot/(n*nprev);
        ip1=nprev << 1;
        ip2=ip1*n;
        ip3=ip2*nrem;
```

```
    i2rev=1;
    for (i2=1;i2<=ip2;i2+=ip1)
    {
        if (i2<i2rev)
        {
            for (i1=i2;i1<=i2+ip1-2;i1+=2)
            {
                for (i3=i1;i3<=ip3;i3+=ip2)
                {
                    i3rev=i2rev+i3-i2;
                    SWAP(ftrans[i3],ftrans[i3rev]);
                    SWAP(ftrans[i3+1],ftrans[i3rev+1]);
                }
            }
        }
        ibit=ip2 >> 1;
        while (ibit>=ip1 && i2rev>ibit)
        {
            i2rev -= ibit;
            ibit >>= 1;
        }
        i2rev += ibit;
    }
    ifp1=ip1;
    while (ifp1<ip2)
    {
        ifp2=ifp1 << 1;
        theta=isign*6.28318530717959/(ifp2/ip1);
        wtemp=sin(0.5*theta);
        wpr = -2.0*wtemp*wtemp;
        wpi=sin(theta);
        wr=1.0;
        wi=0.0;
        for (i3=1;i3<=ifp1;i3+=ip1)
        {
            for (i1=i3;i1<=i3+ip1-2;i1+=2)
            {
                for (i2=i1;i2<=ip3;i2+=ifp2)
                {
                    k1=i2;
                    k2=k1+ifp1;
                    tempr=(float)wr*ftrans[k2]-(float)wi*ftrans[k2+1];
                    tempi=(float)wr*ftrans[k2+1]+(float)wi*ftrans[k2];
                    ftrans[k2]=ftrans[k1]-tempr;
                    ftrans[k2+1]=ftrans[k1+1]-tempi;
                    ftrans[k1] += tempr;
                    ftrans[k1+1] += tempi;
                }
            }
            wr=(wtemp=wr)*wpr-wi*wpi+wr;
            wi=wi*wpr+wtemp*wpi+wi;
        }
        ifp1=ifp2;
    }
    nprev *= n;
}
```

```
    k=1;
    for (i=0;i<Fat;i++)
    {
        for (j=0;j<Fat;j++)
        {
            fsurf[i][j]=(float)((ftrans[k]*ftrans[k])+(ftrans[k+1]*ftrans[k+1]));
            k=k+2;
        }
    }
}

void define_neighbor ()                /* Neighbor positions. */
{
    int i;
    for (i=1;i<Nat;i++)
        neighx[i][0]=i-1;
    neighx[0][0]=Nat-1;
    for (i=0;i<(Nat-1);i++)
        neighx[i][1]=i+1;
    neighx[Nat-1][1]=0;
    for (i=1;i<Nat;i++)
        neighy[i][0]=i-1;
    neighy[0][0]=Nat-1;
    for (i=0;i<(Nat-1);i++)
        neighy[i][1]=i+1;
    neighy[Nat-1][1]=0;
}

void define_barrier ()                 /* Activation barriers in eV. */
{
    double jump;                       /* Jump barrier. */
    double bond;                       /* Bond barrier. */
    double vert1;                      /* Step edge barrier for single step height. */
    double vert2;                      /* Step edge barrier for double step height. */
    vert1=0.15;
    vert2=0.40;
    jump=0.55;
    bond=0.30;
    barrier[0]=jump;
    barrier[1]=jump+vert1;
    barrier[2]=jump+vert2;
    barrier[3]=bond+jump;
    barrier[4]=bond+jump+vert1;
    barrier[5]=bond+jump+vert2;
    barrier[6]=2.0*bond+jump;
     barrier[7]=2.0*bond+jump+vert1;
    barrier[8]=2.0*bond+jump+vert2;
    barrier[9]=3.0*bond+jump;
    barrier[10]=3.0*bond+jump+vert1;
    barrier[11]=3.0*bond+jump+vert2;
}

void define_kinetic ()                 /* Si PLD energy distribution. */
{
    int i,j,k;
    int atom;                          /* Atom position in deposition list. */
```

```
int cat;                          /* Energy category. */
double rnum;                      /* Random number. */
double kinetic[126][4];           /* Energetic energy info: [index][energy,eprob,brprob] */
kinetic[0][0]=135.0;
for (i=1;i<126;i++)
    kinetic[i][0]=kinetic[i-1][0]-(double)(1.0);
kinetic[125][1]=0.00342;
kinetic[124][1]=0.00841;
kinetic[123][1]=0.01146;
kinetic[122][1]=0.01330;
kinetic[121][1]=0.01437;
kinetic[120][1]=0.01758;
kinetic[119][1]=0.02079;
kinetic[118][1]=0.02280;
kinetic[117][1]=0.02412;
kinetic[116][1]=0.02492;
kinetic[115][1]=0.02536;
kinetic[114][1]=0.02553;
kinetic[113][1]=0.02500;
kinetic[112][1]=0.02447;
kinetic[111][1]=0.02293;
kinetic[110][1]=0.02154;
kinetic[109][1]=0.02028;
kinetic[108][1]=0.01914;
kinetic[107][1]=0.01811;
kinetic[106][1]=0.01716;
kinetic[105][1]=0.01630;
kinetic[104][1]=0.01550;
kinetic[103][1]=0.01477;
kinetic[102][1]=0.01409;
kinetic[101][1]=0.01347;
kinetic[100][1]=0.01289;
kinetic[99][1]=0.01235;
kinetic[98][1]=0.01184;
kinetic[97][1]=0.01160;
kinetic[96][1]=0.01136;
kinetic[95][1]=0.01142;
kinetic[94][1]=0.01146;
kinetic[93][1]=0.01148;
kinetic[92][1]=0.01147;
kinetic[91][1]=0.01145;
kinetic[90][1]=0.01141;
kinetic[89][1]=0.01136;
kinetic[88][1]=0.01129;
kinetic[87][1]=0.01122;
kinetic[86][1]=0.01114;
kinetic[85][1]=0.01106;
kinetic[84][1]=0.01097;
kinetic[83][1]=0.01087;
kinetic[82][1]=0.01077;
kinetic[81][1]=0.01067;
kinetic[80][1]=0.01056;
kinetic[79][1]=0.01046;
kinetic[78][1]=0.01035;
kinetic[77][1]=0.01024;
kinetic[76][1]=0.01008;
```

```
kinetic[75][1]=0.00993;
kinetic[74][1]=0.00968;
kinetic[73][1]=0.00945;
kinetic[72][1]=0.00922;
kinetic[71][1]=0.00900;
kinetic[70][1]=0.00880;
kinetic[69][1]=0.00859;
kinetic[68][1]=0.00840;
kinetic[67][1]=0.00822;
kinetic[66][1]=0.00804;
kinetic[65][1]=0.00786;
kinetic[64][1]=0.00770;
kinetic[63][1]=0.00754;
kinetic[62][1]=0.00738;
kinetic[61][1]=0.00714;
kinetic[60][1]=0.00690;
kinetic[59][1]=0.00660;
kinetic[58][1]=0.00630;
kinetic[57][1]=0.00602;
kinetic[56][1]=0.00576;
kinetic[55][1]=0.00550;
kinetic[54][1]=0.00526;
kinetic[53][1]=0.00502;
kinetic[52][1]=0.00480;
kinetic[51][1]=0.00459;
kinetic[50][1]=0.00439;
kinetic[49][1]=0.00419;
kinetic[48][1]=0.00401;
kinetic[47][1]=0.00383;
kinetic[46][1]=0.00366;
kinetic[45][1]=0.00349;
kinetic[44][1]=0.00334;
kinetic[43][1]=0.00319;
kinetic[42][1]=0.00304;
kinetic[41][1]=0.00290;
kinetic[40][1]=0.00277;
kinetic[39][1]=0.00264;
kinetic[38][1]=0.00252;
kinetic[37][1]=0.00240;
kinetic[36][1]=0.00229;
kinetic[35][1]=0.00218;
kinetic[34][1]=0.00207;
kinetic[33][1]=0.00197;
kinetic[32][1]=0.00188;
kinetic[31][1]=0.00178;
kinetic[30][1]=0.00169;
kinetic[29][1]=0.00161;
kinetic[28][1]=0.00152;
kinetic[27][1]=0.00144;
kinetic[26][1]=0.00136;
kinetic[25][1]=0.00129;
kinetic[24][1]=0.00122;
kinetic[23][1]=0.00115;
kinetic[22][1]=0.00108;
kinetic[21][1]=0.00102;
kinetic[20][1]=0.000954354;
```

```
kinetic[19][1]=0.000894174;
kinetic[18][1]=0.000836308;
kinetic[17][1]=0.000780322;
kinetic[16][1]=0.000726362;
kinetic[15][1]=0.000674283;
kinetic[14][1]=0.000623795;
kinetic[13][1]=0.000575188;
kinetic[12][1]=0.000528171;
kinetic[11][1]=0.000482891;
kinetic[10][1]=0.000439058;
kinetic[9][1]=0.000396671;
kinetic[8][1]=0.000355586;
kinetic[7][1]=0.000316093;
kinetic[6][1]=0.000277757;
kinetic[5][1]=0.000240722;
kinetic[4][1]=0.000204990;
kinetic[3][1]=0.000170271;
kinetic[2][1]=0.000136853;
kinetic[1][1]=0.000104448;
kinetic[0][1]=0.000076020;
kinetic[125][3]=0.08195;
kinetic[124][3]=0.09988;
kinetic[123][3]=0.11781;
kinetic[122][3]=0.13574;
kinetic[121][3]=0.15367;
kinetic[120][3]=0.17160;
kinetic[119][3]=0.18953;
kinetic[118][3]=0.20746;
kinetic[117][3]=0.22539;
kinetic[116][3]=0.24332;
kinetic[115][3]=0.26125;
kinetic[114][3]=0.27918;
kinetic[113][3]=0.29711;
kinetic[112][3]=0.31504;
kinetic[111][3]=0.33297;
kinetic[110][3]=0.35090;
kinetic[109][3]=0.36883;
kinetic[108][3]=0.38676;
kinetic[107][3]=0.40469;
kinetic[106][3]=0.42262;
kinetic[105][3]=0.44055;
kinetic[104][3]=0.45848;
kinetic[103][3]=0.47641;
kinetic[102][3]=0.49434;
kinetic[101][3]=0.51227;
kinetic[100][3]=0.53020;
kinetic[99][3]=0.54813;
kinetic[98][3]=0.56606;
kinetic[97][3]=0.58399;
kinetic[96][3]=0.60192;
kinetic[95][3]=0.61985;
kinetic[94][3]=0.63778;
kinetic[93][3]=0.65571;
kinetic[92][3]=0.67364;
kinetic[91][3]=0.69157;
kinetic[90][3]=0.70950;
```

```
kinetic[89][3]=0.72743;
kinetic[88][3]=0.74536;
kinetic[87][3]=0.76329;
kinetic[86][3]=0.78122;
kinetic[85][3]=0.79915;
kinetic[84][3]=0.81708;
kinetic[83][3]=0.83501;
kinetic[82][3]=0.85294;
kinetic[81][3]=0.87087;
kinetic[80][3]=0.88880;
kinetic[79][3]=0.90673;
kinetic[78][3]=0.92466;
kinetic[77][3]=0.94259;
kinetic[76][3]=0.96052;
kinetic[75][3]=0.97845;
kinetic[74][3]=0.99638;
for (i=0;i<74;i++)
    kinetic[i][3]=1.00000;
kinetic[0][2]=kinetic[0][1];
for (i=1;i<126;i++)
    kinetic[i][2]=kinetic[i-1][2]+kinetic[i][1];
atom=0;
if (pulse==1)
{
    k=0;
    j=(int)(kinetic[0][2]*(double)(Nper));
    if (j>k)
    {
        for (k=0;k<j;k++)
        {
            kinet[atom][0]=kinetic[0][0];
            kinet[atom][1]=kinetic[0][3];
            atom=atom+1;
        }
    }
    for (i=1;i<126;i++)
    {
        j=(int)(kinetic[i][2]*(double)(Nper))-atom;
        for (k=0;k<j;k++)
        {
            kinet[atom][0]=kinetic[i][0];
            kinet[atom][1]=kinetic[i][3];
            atom=atom+1;
        }
    }
}
else
{
    while (atom<Ndep)
    {
        do
            rnum=ran0();
        while (rnum==0.0);
        if ((0.0<rnum)&&(rnum<=kinetic[0][2]))
            cat=0;
        for (i=1;i<126;i++)
```

```
                {
                    if ((kinetic[i-1][2]<rnum)&&(rnum<=kinetic[i][2]))
                        cat=i;
                }
                kinet[atom][0]=kinetic[cat][0];
                kinet[atom][1]=kinetic[cat][3];
                atom=atom+1;
            }
        }
}

void classify_atom (atom)               /* Jump types and rates classification. */
int atom;
{
    int i,j;
    int nx,ny;                          /* Atom x and y positions. */
    int nxneigh,nyneigh;                /* Neighbor atom x and y positions. */
    int coor;                           /* Atom coordination. */
    int situtype;                       /* Jump type. */
    int freq;                           /* Jump attempt frequency in each direction. */
    int delz0;                          /* Atom depth. */
    int delz[4];                        /* Depth differences between atom and neighbor: [dir] */
    freq=150;
    nx=dep[atom][0];
    ny=dep[atom][1];
    for (i=0;i<4;i++)
    {
        situtype=situ[atom][i];
        if ((situtype>=0)&&(situtype<12))
            N[situtype]=N[situtype]-1;
    }
    nyneigh=neighy[ny][0];
    delz[0]=dep[atom][2]-surf[nx][nyneigh][0];
    nyneigh=neighy[ny][1];
    delz[2]=dep[atom][2]-surf[nx][nyneigh][0];
    nxneigh=neighx[nx][0];
    delz[1]=dep[atom][2]-surf[nxneigh][ny][0];
    nxneigh=neighx[nx][1];
    delz[3]=dep[atom][2]-surf[nxneigh][ny][0];
    coor=0;
    for (i=0;i<4;i++)
    {
        if (delz[i]<=0)
            coor=coor+1;
        delz[i]=delz[i]-1;
        delz[i]=(int)(sqrt(delz[i]*delz[i]));
    }
    delz0=dep[atom][2]-surf[nx][ny][0];
    if ((delz0<0)||(coor==4)||((delz[0]>2)&&(delz[1]>2)&&(delz[2]>2)&&(delz[3]>2)))
    {
        if (ctrack[atom]>=0)
        {
            Nact=Nact-1;
            for (i=ctrack[atom];i<Nact;i++)
            {
                atrack[i]=atrack[i+1];
```

```
            j=atrack[i];
            ctrack[j]=ctrack[j]-1;
         }
        ctrack[atom]=-1;
        for (i=0;i<4;i++)
        {
            situ[atom][i]=12;
            rate[atom][i]=0.0;
        }
    }
}
else
{
    if (ctrack[atom]<0)
    {
        atrack[Nact]=atom;
        ctrack[atom]=Nact;
        Nact=Nact+1;
    }
    for (i=0;i<4;i++)
    {
        if (delz[i]>2)
        {
            situ[atom][i]=12;
            rate[atom][i]=0.0;
        }
        else
        {
            if (coor==0)
            {
                if (delz[i]==0)
                {
                    N[0]=N[0]+1;
                    situ[atom][i]=0;
                }
                else if (delz[i]==1)
                {
                    N[1]=N[1]+1;
                    situ[atom][i]=1;
                }
                else
                {
                    N[2]=N[2]+1;
                    situ[atom][i]=2;
                }
            }
            else if (coor==1)
            {
                if (delz[i]==0)
                {
                    N[3]=N[3]+1;
                    situ[atom][i]=3;
                }
                else if (delz[i]==1)
                {
                    N[4]=N[4]+1;
```

```
                        situ[atom][i]=4;
                    }
                    else
                    {
                        N[5]=N[5]+1;
                        situ[atom][i]=5;
                    }
                }
                else if (coor==2)
                {
                    if (delz[i]==0)
                    {
                        N[6]=N[6]+1;
                        situ[atom][i]=6;
                    }
                    else if (delz[i]==1)
                    {
                        N[7]=N[7]+1;
                        situ[atom][i]=7;
                    }
                    else
                    {
                        N[8]=N[8]+1;
                        situ[atom][i]=8;
                    }
                }
                else if (coor==3)
                {
                    if (delz[i]==0)
                    {
                        N[9]=N[9]+1;
                        situ[atom][i]=9;
                    }
                    else if (delz[i]==1)
                    {
                        N[10]=N[10]+1;
                        situ[atom][i]=10;
                    }
                    else
                    {
                        N[11]=N[11]+1;
                        situ[atom][i]=11;
                    }
                }
                situtype=situ[atom][i];
                rate[atom][i]=freq*exp(((-1)*barrier[situtype])/energy[atom]);
            }
        }
    }
}


void define_surface ()                    /* Substrate. */
{
    int i,j;
    Natom=0;
```

```
    for (j=0;j<Nat;j++)
    {
        for (i=0;i<Nat;i++)
        {
            surf[i][j][0]=0;
            surf[i][j][1]=Natom;
            dep[Natom][0]=i;
            dep[Natom][1]=j;
            dep[Natom][2]=0;
            Natom=Natom+1;
        }
    }
    for (i=0;i<Nsub;i++)
        energy[i]=thermal;
}

void move_atom (atom,dir)            /* Atom jump. */
int atom,dir;
{
    int i;
    int nx,ny;                       /* Atom x and y positions before jump. */
    int nxnew,nynew;                 /* Atom x and y positions after jump. */
    int nx0,nx1;                     /* Neighbor atom x positions before jump. */
    int ny0,ny1;                     /* Neighbor atom y positions before jump. */
    int nxnew0,nxnew1;               /* Neighbor atom x positions after jump. */
    int nynew0,nynew1;               /* Neighbor atom y positions after jump. */
    int neighbor[8];                 /* Neighbor atoms before and after jump: [dir] */
    nx=dep[atom][0];
    ny=dep[atom][1];
    nx0=neighx[nx][0];
    nx1=neighx[nx][1];
    ny0=neighy[ny][0];
    ny1=neighy[ny][1];
     if (dir==0)
    {
        nxnew=nx;
        nynew=ny0;
    }
    else if (dir==2)
    {
        nxnew=nx;
        nynew=ny1;
    }
    else if (dir==1)
    {
        nynew=ny;
        nxnew=nx0;
    }
    else if (dir==3)
    {
        nynew=ny;
        nxnew=nx1;
    }
    nxnew0=neighx[nxnew][0];
    nxnew1=neighx[nxnew][1];
    nynew0=neighy[nynew][0];
```

```
    nynew1=neighy[nynew][1];
    dep[atom][0]=nxnew;
    dep[atom][1]=nynew;
    dep[atom][2]=surf[nxnew][nynew][0]+1;
    surf[nx][ny][0]=surf[nx][ny][0]-1;
    surf[nxnew][nynew][0]=surf[nxnew][nynew][0]+1;
    surf[nx][ny][1]=-1;
    i=Natom-1;
    do
    {
        if ((dep[i][0]==nx)&&(dep[i][1]==ny)&&(dep[i][2]==surf[nx][ny][0]))
            surf[nx][ny][1]=i;
        else
            i=i-1;
    }
    while (surf[nx][ny][1]==-1);
    neighbor[0]=surf[nx][ny0][1];
    neighbor[1]=surf[nx0][ny][1];
    neighbor[2]=surf[nx][ny1][1];
    neighbor[3]=surf[nx1][ny][1];
    neighbor[4]=surf[nxnew][nynew0][1];
    neighbor[5]=surf[nxnew0][nynew][1];
    neighbor[6]=surf[nxnew][nynew1][1];
    neighbor[7]=surf[nxnew1][nynew][1];
    surf[nxnew][nynew][1]=atom;
    for (i=0;i<8;i++)
        classify_atom (neighbor[i]);
    classify_atom (atom);
}

void thermal_jump ()                /* Select generic jump and jump. */
{
    int i,j,k;
    int rnum1;                      /* Random number. */
    int situtype;                   /* Jump type. */
    int atom;                       /* Atom. */
    int dir;                        /* Direction. */
    double rnum2;                   /* Random number. */
    double rtot;                    /* Total rate. */
    double rsitutype[12];           /* Rates for jump types: [type] */
    rtot=0.0;
    for (i=0;i<12;i++)
        rsitutype[i]=0.0;
    for (i=0;i<Nact;i++)
    {
        atom=atrack[i];
        for (j=0;j<4;j++)
        {
            k=situ[atom][j];
            rsitutype[k]=rsitutype[k]+rate[atom][j];
            rtot=rtot+rate[atom][j];
        }
    }
    if (rtot>0.0)
    {
        rsitutype[0]=rsitutype[0]/rtot;
```

```
        for (i=1;i<12;i++)
            rsitutype[i]=rsitutype[i-1]+rsitutype[i]/rtot;
        do
            rnum2=ran0();
        while (rnum2==0.0);
        if ((0.0<rnum2)&&(rnum2<=rsitutype[0]))
            situtype=0;
        for (i=1;i<12;i++)
        {
            if ((rsitutype[i-1]<rnum2)&&(rnum2<=rsitutype[i]))
                situtype=i;
        }
        do
            rnum2=ran0();
        while (rnum2==1.0);
        rnum1=(int)(N[situtype]*rnum2);
        i=0;
        j=0;
        k=0;
        while (k<=rnum1)
        {
            atom=atrack[i];
            if (situ[atom][j]==situtype)
                k=k+1;
            if (k<=rnum1)
            {
                j=j+1;
                if (j==4)
                {
                    i=i+1;
                    j=0;
                }
            }
            else
                dir=j;
        }
        move_atom (atom,dir);
    }
}

void spec_jump (atom)                    /* Select specific jump and jump. */
int atom;
{
    int i,j;
    int rnum1;                           /* Random number. */
    int situtype;                        /* Jump type. */
    int dir;                             /* Direction. */
    double rnum2;                        /* Random number. */
    double rtot;                         /* Total rate. */
    double rsitutype[12];                /* Rates for jump types: [type] */
    rtot=0.0;
    for (i=0;i<12;i++)
        rsitutype[i]=0.0;
    for (i=0;i<4;i++)
    {
        j=situ[atom][i];
```

```
            if ((j>=0)&&(j<12))
            {
                rsitutype[j]=rsitutype[j]+rate[atom][i];
                rtot=rtot+rate[atom][i];
            }
        }
        if (rtot>0.0)
        {
            rsitutype[0]=rsitutype[0]/rtot;
            for (i=1;i<12;i++)
                rsitutype[i]=rsitutype[i-1]+rsitutype[i]/rtot;
            do
                rnum2=ran0();
            while (rnum2==0.0);
            if ((0.0<rnum2)&&(rnum2<=rsitutype[0]))
                situtype=0;
            for  (i=1;i<12;i++)
            {
                if ((rsitutype[i-1]<rnum2)&&(rnum2<=rsitutype[i]))
                    situtype=i;
            }
            j=0;
            for (i=0;i<4;i++)
            {
                if (situ[atom][i]==situtype)
                    j=j+1;
            }
            do
                rnum2=ran0();
            while (rnum2==1.0);
            rnum1=(int)(j*rnum2);
            i=0;
            j=0;
            while (j<=rnum1)
            {
                if (situ[atom][i]==situtype)
                    j=j+1;
                if (j<=rnum1)
                    i=i+1;
                else
                    dir=i;
            }
            move_atom (atom,dir);
        }
    }

    void deposit_atom ()                /* Deposition. */
    {
        int i;
        int nx,ny;                      /* Atom x and y positions. */
        int nx0,nx1;                    /* Neighbor atom x positions. */
        int ny0,ny1;                    /* Neighbor atom y positions. */
        int neighbor[5];                /* Neighbor atoms: [dir] */
        int under;                      /* Atom hit by deposited atom. */
        double rnum;                    /* Random number. */
        do
```

```
            rnum=ran0();
        while (rnum==1.0);
        nx=(int)(Nat*rnum);
        do
            rnum=ran0();
        while (rnum==1.0);
        ny=(int)(Nat*rnum);
        dep[Natom][0]=nx;
        dep[Natom][1]=ny;
        if ((pulse==1)||(pulse==2))
        {
            under=surf[nx][ny][1];
            if (ctrack[under]>-1)
            {
                if (brprob==1.0)
                    spec_jump (under);
                else
                {
                    rnum=ran0();
                    if (rnum<=brprob)
                        spec_jump (under);
                }
            }
        }
        dep[Natom][2]=surf[nx][ny][0]+1;
        printf ("\n%d",(Natom+1-Nsub));
        surf[nx][ny][0]=surf[nx][ny][0]+1;
        nx0=neighx[nx][0];
        nx1=neighx[nx][1];
        ny0=neighy[ny][0];
        ny1=neighy[ny][1];
        neighbor[0]=surf[nx][ny0][1];
        neighbor[1]=surf[nx0][ny][1];
        neighbor[2]=surf[nx][ny1][1];
        neighbor[3]=surf[nx1][ny][1];
        neighbor[4]=surf[nx][ny][1];
        surf[nx][ny][1]=Natom;
        for (i=0;i<5;i++)
            classify_atom (neighbor[i]);
        classify_atom (Natom);
        Natom=Natom+1;
}

int main ()
{
        int i,j,k,m,p;
        int Npulse;                 /* Number of pulses. */
        int Ntot;                   /* Number of atoms. */
        int Nrec[4];                /* File output points: [atoms] */
        double Nrep;                /* Repetition rate in pulses per second. */
        double Nml;                 /* Thickness in monolayers. */
        double Nmicro;              /* Deposition time in microseconds. */
        double rdep;                /* Deposition rate per microsecond. */
        double rtot;                /* Jump rate per microsecond. */
        double tdep;                /* Time between depositions in microseconds. */
        double tpdep;               /* Time between depositions with exp deviation. */
```

```
double tthm;                        /* Thermalization time in microseconds. */
double tpul;                        /* Time between pulses in microseconds. */
double timer;                       /* Time tracker. */
double Nmlr[4];                     /* File output points: [thick] */
char out_name1[25];                 /* Real output file name. */
char out_name2[25];                 /* Complete Fourier output file name. */
char out_name3[25];                 /* Averaged Fourier output file name. */
FILE *out1;
FILE *out2;
FILE *out3;
printf ("\nReal output file? ");
scanf ("%24s",out_name1);
 printf ("\nComplete Fourier output file? ");
scanf ("%24s",out_name2);
printf ("\nAveraged Fourier output file? ");
 scanf ("%24s",out_name3);
printf ("\nSubstrate dimensions (atoms)? ");
scanf ("%d",&Nat);
printf ("\nSubstrate temperature (C)? ");
scanf ("%lg",&thermal);
printf ("\nST (0), PK (1), SK (2), PT (3) growth? ");
scanf ("%d",&pulse);
Nsub=Nat*Nat;
if ((pulse==0)||(pulse==2))
{
    printf ("\nDeposition thickness (mL)? ");
    scanf ("%lg",&Nml);
    printf ("\nDeposition rate (mL/second)? ");
    scanf ("%lg",&rdep);
    printf ("\nFirst record thickness (mL)? ");
    scanf ("%lg",&Nmlr[0]);
    printf ("\nSecond record thickness (mL)? ");
    scanf ("%lg",&Nmlr[1]);
    printf ("\nThird record thickness (mL)? ");
    scanf ("%lg",&Nmlr[2]);
    printf ("\nFourth record thickness (mL)? ");
    scanf ("%lg",&Nmlr[3]);
    tdep=1000000.0/(rdep*Nsub);
    Ndep=(int)(Nml*Nsub);
    for (i=0;i<4;i++)
        Nrec[i]=(int)(Nmlr[i]*Nsub);
}
else
{
    Nmicro=5.0;
    printf ("\nDeposition rate (mL/pulse)? ");
    scanf ("%lg",&Nml);
    printf ("\nNumber of pulses? ");
    scanf ("%d",&Npulse);
    printf ("\nLaser repetition rate (Hz)? ");
    scanf ("%lg",&Nrep);
    printf ("\nFirst record pulse number? ");
    scanf ("%d",&Nrec[0]);
    printf ("\nSecond record pulse number? ");
    scanf ("%d",&Nrec[1]);
    printf ("\nThird record pulse number? ");
```

```
        scanf ("%d",&Nrec[2]);
        printf ("\nFourth record pulse number? ");
        scanf ("%d",&Nrec[3]);
        Nper=(int)(Nml*Nsub);
        Ndep=Nper*Npulse;
        tdep=((double)(Nmicro))/((double)(Nper));
        tpul=(1000000.0/Nrep)-(double)(Nmicro);
}
out1=fopen(out_name1,"w");
 out2=fopen(out_name2,"w");
out3=fopen(out_name3,"w");
srand((unsigned)time(NULL));
Ntot=Ndep+Nsub;
Fat=(Nat/2)+1;
thermal=(thermal+273.15)*0.000086183;
tthm=0.000005;
surf=(int***)malloc(sizeof(int**)*Nat);
neighx=(int**)malloc(sizeof(int*)*Nat);
neighy=(int**)malloc(sizeof(int*)*Nat);
dep=(int**)malloc(sizeof(int*)*Ntot);
situ=(int**)malloc(sizeof(int*)*Ntot);
ctrack=(int*)malloc(sizeof(int)*Ntot);
 atrack=(int*)malloc(sizeof(int)*(Nsub+1));
fsurf=(float**)malloc(sizeof(float*)*Fat);
rate=(double**)malloc(sizeof(double*)*Ntot);
energy=(double*)malloc(sizeof(double)*Ntot);
ftrans=(float*)malloc(sizeof(float)*(2*Nsub+1));
for (i=0;i<Fat;i++)
        fsurf[i]=(float*)malloc(sizeof(float)*Fat);
for (i=0;i<Nat;i++)
{
        surf[i]=(int**)malloc(sizeof(int*)*Nat);
        neighx[i]=(int*)malloc(sizeof(int)*2);
        neighy[i]=(int*)malloc(sizeof(int)*2);
}
for (i=0;i<Nat;i++)
{
        for (j=0;j<Nat;j++)
                surf[i][j]=(int*)malloc(sizeof(int)*2);
}
for (i=0;i<Ntot;i++)
{
        dep[i]=(int*)malloc(sizeof(int)*3);
        situ[i]=(int*)malloc(sizeof(int)*4);
        rate[i]=(double*)malloc(sizeof(double)*4);
}
if ((pulse==0)||(pulse==3))
        kin=0.3;
else
{
        if (pulse==1)
        {
                kinet=(double**)malloc(sizeof(double*)*Nper);
                for (i=0;i<Nper;i++)
                        kinet[i]=(double*)malloc(sizeof(double)*2);
        }
```

```
    else
    {
        kinet=(double**)malloc(sizeof(double*)*Ndep);
        for (i=0;i<Ndep;i++)
            kinet[i]=(double*)malloc(sizeof(double)*2);
    }
    define_kinetic ();
}
define_neighbor ();
define_barrier ();
for (i=0;i<12;i++)
    N[i]=0;
for (i=0;i<Ntot;i++)
{
    ctrack[i]=-1;
    for (j=0;j<4;j++)
    {
        situ[i][j]=12;
        rate[i][j]=0.0;
    }
}
Nact=0;
define_surface ();
if ((pulse==0)||(pulse==2))
{
    for (j=0;j<Ndep;j++)
    {
        if (pulse==0)
            energy[Natom]=kin;
        else
        {
            energy[Natom]=kinet[Natom-Nsub][0];
            brprob=kinet[Natom-Nsub][1];
        }
        deposit_atom ();
        timer=0.0;
        while (timer<=tthm)
        {
            rtot=0.0;
            for (k=0;k<4;k++)
                rtot=rtot+rate[Natom-1][k];
            timer=timer+(1.0/rtot);
            if (timer<=tthm)
                spec_jump (Natom-1);
        }
        energy[Natom-1]=thermal;
        classify_atom (Natom-1);
        tpdep=tdep*expdev();
        timer=0.0;
        while (timer<tpdep)
        {
            rtot=0.0;
            for (k=0;k<Nact;k++)
            {
                p=atrack[k];
                for (m=0;m<4;m++)
```

```
                    rtot=rtot+rate[p][m];
                }
                timer=timer+(1.0/rtot);
                if (timer<=tpdep)
                    thermal_jump ();
            }
            p=j+1;
            if ((p==Nrec[0])||(p==Nrec[1])||(p==Nrec[2])||(p==Nrec[3]))
            {
                for (k=0;k<Nat;k++)
                {
                    for (m=0;m<Nat;m++)
                    {
                        fprintf (out1,"%d %d %d",k,m,surf[k][m][0]);
                        fprintf (out1,"\n");
                    }
                }
                fourn ();
                for (k=0;k<Fat;k++)
                {
                    for (m=0;m<Fat;m++)
                    {
                        fprintf (out2,"%d %d %f",k,m,fsurf[k][m]);
                        fprintf (out2,"\n");
                    }
                }
                for (k=0;k<Fat;k++)
                {
                    fprintf (out3,"%d %f %f",k,fsurf[0][k],fsurf[k][0]);
                    fprintf (out3,"\n");
                }
            }
        }
}
else
{
    for (i=0;i<Npulse;i++)
    {
        for (j=0;j<Nper;j++)
        {
            if (pulse==3)
                energy[Natom]=kin;
            else
            {
                energy[Natom]=kinet[j][0];
                brprob=kinet[j][1];
            }
            deposit_atom ();
            timer=0.0;
            while (timer<=tthm)
            {
                rtot=0.0;
                for (k=0;k<4;k++)
                    rtot=rtot+rate[Natom-1][k];
                timer=timer+(1.0/rtot);
                if (timer<=tthm)
```

```
            spec_jump (Natom-1);
    }
    energy[Natom-1]=thermal;
    classify_atom (Natom-1);
    tpdep=tdep*expdev();
    timer=0.0;
    while (timer<tpdep)
    {
        rtot=0.0;
        for (k=0;k<Nact;k++)
        {
            p=atrack[k];
            for (m=0;m<4;m++)
                rtot=rtot+rate[p][m];
        }
        timer=timer+(1.0/rtot);
        if (timer<=tpdep)
            thermal_jump ();
    }
}
timer=0.0;
while (timer<tpul)
{
    rtot=0.0;
    for (k=0;k<Nact;k++)
    {
        p=atrack[k];
        for (m=0;m<4;m++)
            rtot=rtot+rate[p][m];
    }
    timer=timer+(1.0/rtot);
    thermal_jump ();
}
j=i+1;
if ((j==Nrec[0])||(j==Nrec[1])||(j==Nrec[2])||(j==Nrec[3]))
{
    for (k=0;k<Nat;k++)
    {
        for (m=0;m<Nat;m++)
        {
            fprintf (out1,"%d %d %d",k,m,surf[k][m][0]);
            fprintf (out1,"\n");
        }
    }
    fourn ();
    for (k=0;k<Fat;k++)
    {
        for (m=0;m<Fat;m++)
        {
            fprintf (out2,"%d %d %f",k,m,fsurf[k][m]);
            fprintf (out2,"\n");
        }
    }
    for (k=0;k<Fat;k++)
    {
        fprintf (out3,"%d %f %f",k,fsurf[0][k],fsurf[k][0]);
```

```
                    fprintf (out3,"\n");
                }
            }
        }
    }
    fclose(out1);
    fclose(out2);
    fclose(out3);
    return 1;
}
```